Thermomechanical Properties of Graphene and The Graphene's Impact on Motion of Light Atoms By Means of Molecular Dynamics

Alireza Lajevardipour

Submitted to the
Institute of Graduate Studies and Research
in partial fulfillment of the requirements for the degree of

Doctor of Philosophy
in
Physics

Eastern Mediterranean University
June, 2012
Gazimağusa, North Cyprus

Approval of the Institute of Graduate Studies and Research

Prof. Dr. Elvan Yilmaz
Director

I certify that this thesis satisfies the requirements as a thesis for the degree of Doctor of Philosophy in Physics.

Prof. Dr. Mustafa Halilsoy
Chair, Physics

We certify that we have read this thesis and that in our opinion, it is fully adequate, in scope and quality, as a thesis of the degree of Doctor of Philosophy in Physics.

Prof. Dr. Mustafa Halilsoy
Supervisor

Examining Committee

1. Prof. Dr. Mustafa Halilsoy _____
2. Prof. Dr. Omar Mustafa _____
3. Prof. Dr. Ozay Gurtug _____
4. Assoc.Prof. Dr. Izzet Sakalli _____
4. Assoc.Prof. Dr. Tugrul Hakioglu _____

ABSTRACT

In this thesis, our study on graphene is reported, an introductory background on simulation techniques and graphene properties is given. Molecular dynamics framework is used to study graphene at atomic level.

Namely, stochastic motion of noble gases in a periodic two-dimensional potential produced by a graphene sheet is studied. We calculated the depth of the potential well of the interaction between noble gases and the graphene sheet. Langevin equation is solved numerically to explain the effects of the binding energy, coefficient of friction and the equilibrium distance on the motion of noble gases on the graphene sheet.

Next, using the valence force field model of Perebeinos and Tersoff (2009 Phys. Rev. B 79 241409(R)), different energy modes of suspended graphene subjected to tensile or compressive strain are studied. Carrying out Monte Carlo simulations we observed that:

i) only for small strains ($|\varepsilon| \lessapprox 0.02$) the total energy is symmetrical in the strain, while it behaves completely different beyond this threshold.

ii) the important energy contributions in stretching experiments are stretching, angle bending, out-of-plane term and the term provides repulsion against $\pi - \pi$ misalignment.

iii) in compressing experiments the two latter terms increase rapidly and beyond the buckling transition stretching and bending energies are found to be constant.

iv) from stretching-compressing simulations we calculated the Young modulus at room temperature as 350 ± 3.15 N/m. It is found to be in good agreement with experimental results (340 ± 50 N/m) and with ab-initio results 322-353 N/m.

v) molar heat capacity is estimated to be $24.64\,\mathrm{J\,mol^{-1}\,K^{-1}}$ which is comparable with the Dulong-Petit value, i.e. $24.94\,\mathrm{J\,mol^{-1}\,K^{-1}}$ and is almost independent of the strain.

vi) non-linear scaling properties were obtained from height-height correlations at finite temperature.

viii) the used valence force field model results in a temperature independent bending modulus for graphene.

Keywords: graphene sheet, stochastic motion, Noble gases, Langevin dynamics, valence force field, thermomechanical properties, suspended graphene, tensile and compressive strain.

ÖZ

Grafen üzerine yaptığımız bu tez çalışması similasyon (taklit yöntemi) için bir ön literatür ve grafen teknikleri içermektedir. Burada moleküler yöntemler grafenin atomik incelenmesinde kullanılmıştır.

İlk önce grafen levhanın 2 - boyutlu potansiyelindeki asal (soy) bir gazın stokastik (tahmini) hareketi incelenmiştir. Bu çerçevede asal gaz ile grafen levha arasındaki potansiyelin derinliği hesap edilmiştir. Etkileşimin bağlanma enerjisi, sürtünme katsayısı ve denge konumlarının tespiti için sayısal (numerik) Langevin denklemi kullanılmıştır.

Daha sonra Perebeinos ve Tersoff'un [Phys.Rev. B79, 241409 (R) (2009)] değerlik (valans) kuvvet alan yöntemi kullanarak asılı grafenin gerilme ve sıkışma altındaki farklı enerji kipleri incelenmiştir. Monte Carlo yöntemi kullanarak aşağıdaki sonuçlar elde edilmiştir:

i) Toplam enerji küçük gerilme ($|\varepsilon| \lessapprox 0.02$) altında simetrik bir yapı sergilemekte, bunun ötesinde ise farklı görülmektedir.

ii) Enerjiye katkı sağlayan unsurlar, gerilme, açı - bükülmesi, düzlem sapması ve düzensiz dizilimli $\pi - \pi$ itişinden kaynaklanmaktadır.

iii) Sıkıştırma deneylerinde önceki iki etki hızla artmakta, bunun sonunda dolanıma geçiş gerilimi ve bükülme enerjileri sabit kalmaktadır.

iv) Gerilme - sıkıştırma similasyonlarında, oda sıcaklığında Young modülü 350 ± 3.15 N/m olarak tesbit edilmiş bu ise deneysel (340 ± 50 N/m) ve asli aralık olan 322-353 N/m değerlerine uyum sağlamaktadır.

v) Molar ısı kapasitesi $24.64\,\mathrm{J\,mol^{-1}\,K^{-1}}$ olarak bulunmuş, ki bu Dulong - Petit değeri olan $24.94\,\mathrm{J\,mol^{-1}\,K^{-1}}$ e uygun olarak neredeyse gerilimden bağımsız davranmaktadır.

vi) Kısıtlı sıcaklıkta Lineer olmayan ayar özellikleri yükseklik - yükseklik bağlantısından elde edilmiştir. vii) Değerlik kuvvet alan modeli sıcaklıktan bağımsız bir bükülme mödülü sergilemektedir.

Anahtar Kelimeler: Grafen levha, stokastik hareket, asal (soy) gazlar, Langevin dinamiği, değerlik (valans) kuvvet alan modeli, termomekanik özellikler, gerilen ve sıkıştırılan asılı grafen.

ACKNOWLEDGEMENTS

I would like to thank my family for their endless support. Also I like to appreciate my friend Mehdi Neek-Amal for his scientific efforts in years collaborating together. The chairman in department of physics, prof. Mustafa Halilsoy, was very obliging to me. I will never forget his awesome lecture on advanced analytical mechanics.Also he protected me to continue my PhD after my supervisor were dismissed from university. It is important to respect all staff and faculty members in department of physics for their friendly social interaction in duration of my PhD at EMU. Prof Ozay Gurtug for his nice courses and his helping attitude. Çilem Aydintan for her friendly help more than a normal secretary. Resat Akoglu as a helping lab technician. And all my friends in faculty of Arts and Sciences.

TABLE OF CONTENTS

LIST OF FIGURES

LIST OF TABLES

LIST OF ABBREVIATIONS

2D two dimensions

2DPP two dimensional periodic potential

acGNRs armchair graphene nanoribbons

CVD chemical vapor deposition

CNTs carbon nanotubes

CNT carbon nanotube

GNRs graphene nanoribbons

LJ Lennard-Jones

MD Molecular dynamics

MC Monte Carlo

MWCNTs multi-walled carbon nanotubes

SWCNT single walled carbon nanotube

SWCNTs single walled carbon nanotubes

PBC periodic boundary conditions

zzGNRs zigzag graphene nanoribbons

Chapter 1

INTRODUCTION

In recent decades, carbon has attracted interest as a nano-material, due to the diversity of its stable forms and their novel properties. In particular, the graphene (discovered in 2004) has been subjected to many studies of its peculiar properties to use in new devices at nanometer scale.

Graphene has opened huge possibilities in electronic device fabrication and has shown much promise in replacing silicon-based electronics. It has made it possible to understand properties at low-dimension. Including, the observation of integer quantum Hall effect (even at room temperature), breakdown of adiabatic Born-Oppenheimer approximation, realization of Klein paradox, possibilities of high T_c superconductivity, metal-free magnetism, ballistic electronic propagation, charge-carrier doping, chemical activities and high surface area (making graphene as the material of the 21st century). The diverse structural and electronic features as well as exciting applications have attracted theoretical and experimental scientists to explore such low dimensional material [1].

Moreover, nanotechnology has been a major focus in science and technology where most research in this area deals with chemical, physical and biological issues or a combination of them. Nanotechnology is a multidisciplinary subject ranging from physics, chemistry, biology and material science to mechanical and electrical engineering.

The underlying theme of nanotechnology is to handle matter in nano-scale where physical properties are size dependent. Therefore, 'nanotechnology' might be referred to as the study of those small-scale objects which can be assembled to create a novel device. Examples of nanotechnology in modern use are the present nanostructures such as carbon nanotubes, buckyballs and graphene sheets that

provide a possible new basis for the creation of many nano-devices due to their conspicuous properties like their high strength, high flexibility and low weight.

Experience shows that deep understanding of material properties can result in great improvement to products and promote the development of novel ones. Therefore, it is essential to recognize that materials are inherently of a hierarchical multiscale character. Properties should not be considered as monolithic quantities only at macroscopic levels, as historically taught. Rather, important material properties can arise at a myriad of length scales ranging from atomic to microscopic to mesoscopic to macroscopic. Study of nanoscience necessarily draws from foundations in electronic structure and atomistic-scale phenomena, which are the basic building blocks of materials. Scientists and engineers are increasingly drawn together by this unifying theme to develop multiscale methods to bridge the gaps between lowerscale and macroscopic theory [2].

Taking advantage of modern supercomputers and modeling techniques to predict properties of new nanomaterials such as mechanical, electrical, optical and thermal properties is very crucial. Such computational studies can accelerate developments in materials, manufacturing, electronics, medicine and healthcare, energy, the environment and world security.

To date, many work has been undertaken on computational modeling at nanoscale which can significantly reduce the time taken in the trial-and-error processes leading to applications (and in turn, decreases the research cost). Rather than employing large-scale laboratory facilities, computational modeling can utilize elementary mechanical principles and classical mathematical modeling procedures to investigate the mechanics of nanoscale systems. Computational simulation is also recognized now as an essential element between theory and experimentation. These concepts comprise the foundations of a new multidisciplinary study at the interface of science and engineering, which is referred to in the current literature as multiscale, multi-physics modeling and simulation [2, 3]. Translating a scientific problem into computer application requires the participation of all members of the science and technology community. Then it cause discussions

between different scientific fields, utilization of high-performance computing, and experiment-simulation cooperation [4].

In this work, we study the graphene interaction with gases and the graphene sheet under strain. Molecular dynamics simulation is utilized to examine the effect of graphene on the motion of some gas atoms and to investigate thermo-mechanical properties of graphene sheet under strain.

This work is divided into five chapters. The scientific simulation methods, involving the related potentials and numerical algorithm are presented in Chapter 2. Physical properties of graphene and its brief history are given in Chapter 3. In Chapter 4, our study on stochastic motion of noble gases on a graphene sheet is reported. Finally, Chapter 5 comprises our last work about thermomechanical properties of graphene with the means of valence force field model.

Chapter 2

SCIENTIFIC SIMULATION

2.1 Techniques

Mechanical property of a material depends on its atomistic structure and the way it is configured. A comprehensive investigation of the evolution of atomistic configuration with time is crucial to understand the mechanisms of material deformation. In nano-scale where direct experimental observation is difficult to conduct. Therefore, numerical simulation techniques are used as very powerful tools ubiquitously [2, 5, 6, 7, 8, 9, 10].

Molecular dynamics (MD), for example, enables us to study the atomic dynamic behavior at the atomic scale. The kinetic energy of the system can be ignored when the temperature is at zero Kelvin. Atomistic analysis can be conducted statistically by Monte Carlo (MC) methods, in which random process will be investigated for deformation and failure.

Since the 1980s, MD methods have become widely accepted and improved because of rapid computer developments and innovations in computational algorithms. These developments show that MD has gradually become an effective atomistic simulation method [5, 6, 7, 8, 9].

The idea of numerical simulation is to simulate an atomic system from atomic interactions. These interactions can be determined for a certain atomic configuration with interatomic potentials. Where the potentials can be obtained from experience, experimental data or quantum mechanics. Based on the principle of total potential energy, that energy can be minimized to explore the stable structure of the system (static lattice calculation), the force on each atom can be calculated to generate atom motion (MD), the energy required for a certain pro-

cess can be associated with probabilities to statistically study the process (MC method), the minimum energy path evolved from a given initial configuration to the final configurations. Other properties of the system can also be calculated from the total energy or analyzed through a simulated process. Since MD is a commonly used method in multiscale analysis and has wide applications, it can be used as an example to explain the simulation process.

After a configuration of atoms is constructed, the potentials are used to determine the force on each atom. Then the atoms are allowed to move for a short time Δt with the initial velocities and calculated accelerations, following Newton's second law of particle motion. Then the forces are calculated again with the new atom positions and the step is repeated. There is a numerical process with integration for a time step Δt and cycling to update configurations for time steps (h).

h is the number of loading steps to complete the designed simulation time t (i.e., $t = h\Delta t$) and is usually about $10^4 - 10^7$. To follow fast atomic vibrations (of the order of $(1 - 10)THz$ depend on area of simulation) the step-by-step integration process requires very small time steps, typically of $\Delta t = 10^{-15}s$. This numerical analysis is not only used for the analysis under given loading but can also be used first for obtaining the equilibrium status and checking whether the used potential functions are correct. The latter can be done, for instance, to check whether the obtained lattice constant is consistent with the observed one. Last step is for data processing which uses different softwares such as VMD, Jmol, gnuplot, etc. to visualize the acquired configuration and to obtain other useful information.

The MD simulation is not complicated. It is simply a cycling process that finds interatomic forces, update the positions of atoms, and repeats to determine the interatomic forces at the new positions. However, the obtained results can be quite different for different users. The following three factors are essential to get high accuracy for the simulation:

- A realistic initial condition for both position and velocity vectors of the simulation system is absolutely important. Obtaining the equilibrium status of the system before any loading or excitation is essential for getting reliable results. This is a prerequisite condition to carry on non-equilibrium simulation such as system deformation under external loading. To reach that equilibrium status, the system needs to undertake a relaxation process under a certain thermodynamic ensemble such as the so-called "NPT" or "NVE" ensemble (their explanations will mention later in this chapter).

- A rational design of the simulation model and its boundary condition.

- An accurate potential function to calculate the correct interatomic force.

2.2 Potentials

In classical molecular dynamics, the atomic structure (composition of electrons and nucleus) is not considered and is replaced by a single mass point as illustrated in Figure 2.1. However, the interatomic potential and forces have their origin at the subatomic level and therefore the atomic structure must be considered.

Suppose, N is the total number of the atoms in the simulation system. The position of atom i (1, 2, . . . N) can be defined by the vector $\mathbf{r}_i$ or by its components x_i, y_i, and z_i of that atom along the three axes x, y, and z. Figure 2.1 shows the vector $\mathbf{r}_{ij}$ which connects atom i with atom j. The first subscript represents the starting atom and the second indicates the ending atom. In numerical simulation, the length of the vector $\mathbf{r}_{ij}$, namely the scalar r_{ij} is frequently used to describe the distance and relative position between atoms i and j.

the force $\mathbf{F}_i$ at atom i applied by other atoms in the simulation system can be obtained through the derivatives of potential energy U of the system with respect to its position vector $\mathbf{r}_i$:

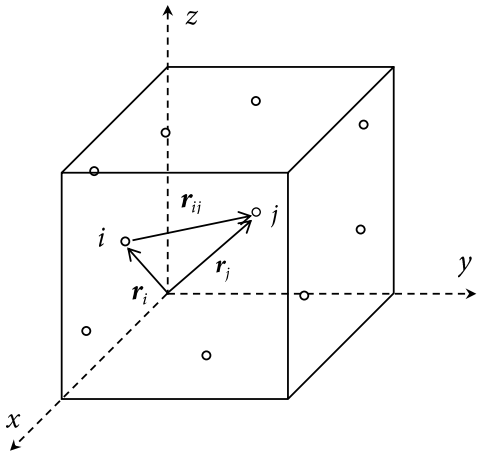

Figure 2.1: The definition of connecting vector ($\mathbf{r}_{ij}$) between i and j atoms.

$$\mathbf{F}_i = -\frac{\partial U\left(\mathbf{r}_1, \ldots, \mathbf{r}_N\right)}{\partial \mathbf{r}_i} \tag{2.1}$$

Pair potentials are the simplest interatomic interactions, and are dependent on the distance r_{ij} between two atoms. The total pair potential of a generic atom i with other near atoms in the simulation system can be expressed as

$$U_i = \sum_{j>i}^{N_i} V_{ij}\left(r_{ij}\right) = \frac{1}{2} \sum_{j=1(j\neq i)}^{N_i} V_{ij}\left(r_{ij}\right) \tag{2.2}$$

where the factor $1/2$ is introduced to avoid double counting. In fact, the pair potential V_{ij} is equally shared by both atom i and j, so atom i should only account for a half.

The following is an example of the differential relationship between energy and force via the pair potential energy between atom i and j

$$U_i = \frac{1}{2} \sum_{j\neq i}^{N_i} V_{ij}\left(|\mathbf{r}_{ij}|\right) = \frac{1}{2} \sum_{j\neq i}^{N_i} V_{ij}\left(|\mathbf{r}_j - \mathbf{r}_i|\right) \tag{2.3}$$

As seen in equation 2.1, if the potential energy U_is is known, the interaction forces between atoms can be determined. Through integrations of Newton's second law and evolution of dynamical variables such as position vector, the velocity

and acceleration of each atom in the system with time can be determined. Therefore, the models for determination of the potential function U and its related force field of the atomic system is the key for numerical simulation.

In equation 2.2, the summation symbol over a typical atom j $(1, ..., N_i)$ covers all atoms within its neighborhood sphere defined with atom i as the center and r_{cut} as the radius. The latter is also called cutoff radius indicating that if $r_{ij} > r_{cut}$ the interatomic potential is too small and can be neglected. The total potential energy U^T of the atomic system can be expressed as the sum of pair potentials of all atoms

$$U^T = \frac{1}{2} \sum_{i=1}^{N} \sum_{j \neq i}^{N_i} V_{ij} \left(r_{ij} \right) \tag{2.4}$$

2.2.1 Lennard-Jones (LJ) Potential

There are a variety of physical models that describe the interatomic interaction. One of the most famous functions for describing pairwise interactions is LJ potential 2.5.

$$V_{LJ} \left(r_{ij} \right) = 4\varepsilon \left[\left(\frac{\sigma}{r_{ij}} \right)^{12} - \left(\frac{\sigma}{r_{ij}} \right)^{6} \right], \tag{2.5}$$

where r_{ij} is the distance between atoms i and j, and the term $1/r_{ij}^{12}$ simulates the repulsive force between two atoms whereas the $1/r_{ij}^{6}$ term describes the attractive force between atoms simulating the van der Waals force. The $1/r_{ij}^{12}$ term comes from the Pauli exclusion principle. It states that when the electron clouds of two atoms begin to overlap, the energy of the system increases rapidly, because two electrons cannot have the same quantum state. On the other hand, Van der Waals force is weaker than repulsive force; therefore the corresponding exponent is 6, much smaller than that of the repulsion term.

The two parameters, σ and ε, in LJ potential (equation 2.5) denotes the collision diameter and the bond energy at the equilibrium position, respectively. The collision diameter (σ) is the distance at which the potential $V(r)$ is zero. At

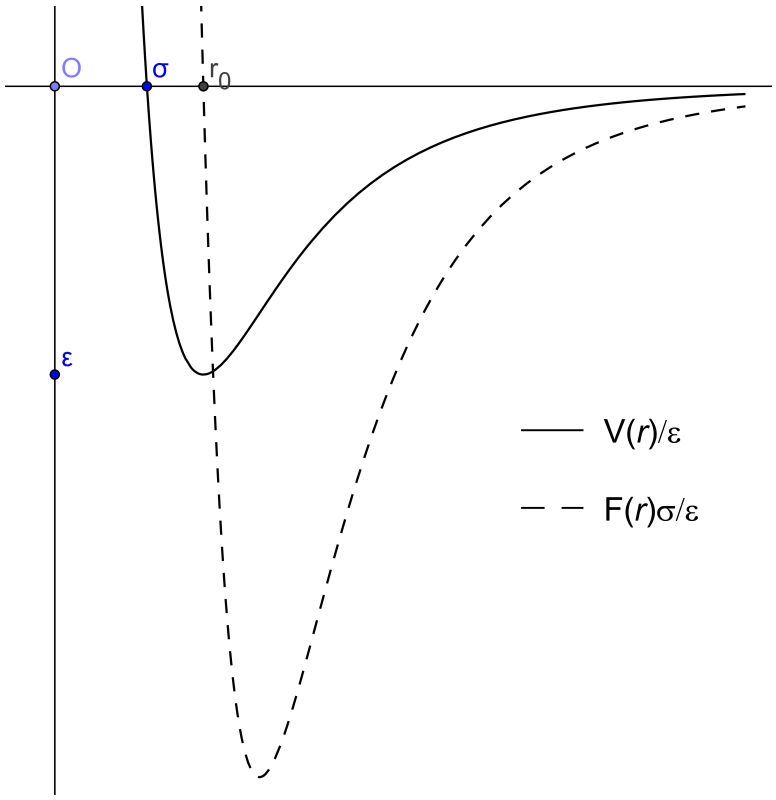

Figure 2.2: The LJ potential and its derivative force with the dimensionless distance.

the equilibrium position ($r = r_0$), $F(r) = 0$ then r_0 is called bond length. ε is negative and is the minimum energy for an atomic pair. It represents the work needed to move coupled atoms from the equilibrium position r_0 to infinity. This is the reason why ε is called bond or dissociation energy.

In Figure 2.2, the solid line represents dimensionless potential energy ($V(r)/\varepsilon$) where the dotted line shows the dimensionless force ($F(r)\sigma/\varepsilon$); both with respect to the dimensionless distance r/σ.

The unit of potential energy $V(r)$ depends on ε and normally is in eV. The equilibrium interatomic distance r_0 is related to the collision diameter σ.

$$r_0 = 2^{1/6}\sigma \tag{2.6}$$

The interactive force between two atoms can be obtained from the derivative of equation 2.5 with respect to r_{ij} as shown in equation 2.7.

$$F_{ij}\left(r_{ij}\right) = -\frac{\partial V_{LJ}\left(r_{ij}\right)}{\partial r_{ij}} = 24\frac{\varepsilon}{\sigma}\left[\left(\frac{\sigma}{r_{ij}}\right)^{13} - \left(\frac{\sigma}{r_{ij}}\right)^{7}\right] \tag{2.7}$$

In the almost one century since LJ potential was proposed, a vast amount of data for parameters σ and ε has been introduced. But it is worth noting that these values are obtained under specific conditions and their credibility depends on the introduced conditions.

The LJ potential has two parameters, σ and ε. But the two parameters available for mono-atoms. To obtain the values of σ and ε for LJ potential between unlike chemical elements, the following averages (equations 2.8 and 2.9) are given by Lorentz-Berthelot mixing rules for parameters $\sigma_{1,2}$ and $\varepsilon_{1,2}$ [5] as

$$\sigma_{1,2} = \frac{1}{2}\left(\sigma_1 + \sigma_2\right), \tag{2.8}$$

$$\varepsilon_{1,2} = \sqrt{\varepsilon_1 \varepsilon_2}. \tag{2.9}$$

2.2.2 Force Field

Calculating the electronic energy for a given nuclear configuration to obtain a potential energy for a system is a major problem due to complexity of quantum states. The force field method is one approach to bypass this problem. A force field is constructed by writing the electronic energy as a parametric function of the nuclear coordinates, and fitting the parameters to experimental data or finding parameter from quantum computational method like ab-intio.

The main element in force field methods are atoms where electrons are not considered as individual particles. This means that instead of solving the Schrödinger equation, bonding information must be provided explicitly. The dynamics of the atoms is handled by classical mechanics whereas quantum mechanical aspects of the nuclear motion are neglected.

Hereby, molecules are treated as a "ball-spring" model, where atoms have different sizes and "elasticity" and bonds have different lengths and "rigidity".

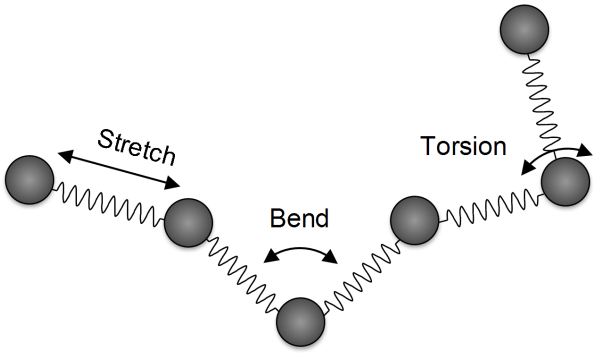

Figure 2.3: The illustration of the fundamental energy terms in a typical force field.

There are many different force fields, but we used valence force field to simulate graphene under strain. The force field energy is written as a sum of energy components:

$$E_{ff} = E_{st} + E_{be} + E_{out} + E_{tors} + E_{cross} + E_{nb} + \cdots \tag{2.10}$$

Where each component describes one degrees of freedom or the energy required for distorting a molecule in a specific way. There are two types of energy in force field, bond terms and non-bond terms. The first five terms on the right-hand side of equation 2.10 are related to bond interactions between any two connected atoms (Figure 2.3); where E_{st} represents the energy for stretching a bond between two atoms, E_{be} is the energy required for bending an angle between two bonds, E_{out} describes the out-of-plane energy, E_{tros} is the torsional energy for twisting about a bond, and E_{cross} represents coupling between the bonding terms. E_{nb} is related to the non-bonded atom-atom interactions and includes the van der Waals energy and electrostatic energy. If there are other mechanisms affecting energy then these may be included in E_{ff} by adding appropriate terms into the above expression.

Consider the idea of masses connected by springs for atoms in a simulation system; by applying Hooke's Law we can evaluate the energy required to stretch and bend bonds from their equilibrium state. In the first approximation or in

simple harmonic case, E_{st} and E_{be} are expressed as equations

$$E_{st} = \frac{K_s}{2} \sum_{i=1}^{N} \sum_{j \neq i}^{N_i} (r_{ij} - r_0)^2 \tag{2.11}$$

$$, E_{be} = K_{be} \sum_{i=1}^{N} \sum_{j<k}^{N_i} (\theta_{ijk} - \theta_0)^2, \tag{2.12}$$

where N is the total number of bonds and N_i is the total number atoms within a neighborhood sphere defined with atom i as the center and r_{cut} as the cutoff radius. K_s and K_{be} are the force constants for stretching and bending, respectively. r_{ij} is the bond length between atom i and j, θ_{ijk} is the angle between the atoms i, j and k. Finally r_0 and θ_0 are equilibrium bond lengths and bond angles. Also in [11], bond bending energy term is introduced as a cosine harmonic

$$E_{be} = K_{be} \sum_{i=1}^{N} \sum_{j<k}^{N_i} (\cos(\theta_{ijk}) - \cos(\theta_0))^2. \tag{2.13}$$

If the central C_0 atom in the configuration shown in Figure 2.4 is sp^2-hybridized, there is a significant energy penalty associated with making the center pyramidal, since the four atoms prefer to be localized in a plane. If the four atoms are exactly in a plane, the sum of the three angles with C_0 as the central atom should be exactly 360°. However, a quite large pulling center out-of-plane may be achieved without seriously distorting any of these three angles. Taking the bond distances to 1.5Å, and moving the central atom 0.2Å out of the plane, only reduces the angle sum to 354.8° (i.e. almost a 1.7° decrease per angle). The corresponding out-of-plane angle, α, is 7.7° for this case. E_{out} is written as a harmonic term in the angle α (and zero for equilibrium state)

$$E_{out} = K_{out} \alpha^2. \tag{2.14}$$

The E_{cross} term includes any needed terms to cover coupling between other bond terms. For chain molecules, an accurate description of their vibro-rotational

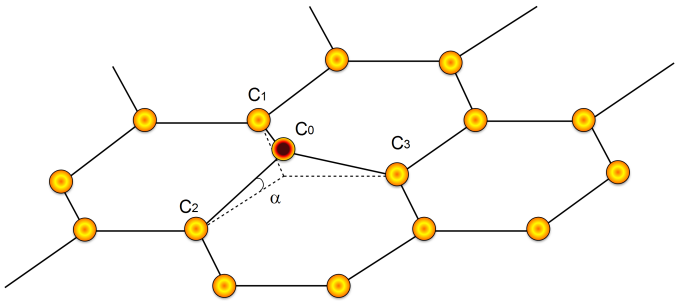

Figure 2.4: The schematic definition of out-of-plane angle.

frequencies often requires the introduction of cross coupling terms. Consider, for example a molecule such as H_2O. It has an equilibrium angle of 104.5° and an O-H distance of 0.958Å. If the angle is compressed to 90°, say, and the optimal bond length is determined by electronic structure calculations, the equilibrium distance becomes 0.968Å (i.e. slightly longer). Similarly, if the angle is widened, the lowest energy bond length becomes shorter than 0.958Å. This may qualitatively be understood by noting that the hydrogen atoms come closer together if the angle is reduced.

This leads to an increased repulsion between the hydrogen atoms, which can be partly alleviated by making the bonds longer. If we just use the first five terms in the force field energy, this coupling between bond distance and angle will be missed. The coupling can be taken into account by including a term that depends on both bond length and angle. E_{cross} may in general include a whole series of terms that couple two (or more) of the bonded terms.

2.3 Numerical Algorithm; Velocity Verlet

From a mathematical point of view, the differential equation of motion is an initial value problem with boundary condition where it can be handled by numerous time steps. Each step will have finite time difference Δt instead of infinitesimal time dt used in the differential equation. The Taylor series expansions for a position function can be used to derive explicit finite difference equations:

$$\mathbf{r}_i(t+\Delta t) = \mathbf{r}_i(t) + \frac{\Delta t}{1!}\frac{d\mathbf{r}_i(t)}{dt} + \frac{\Delta t^2}{2!}\frac{d^2\mathbf{r}_i(t)}{dt^2} + \cdots + \frac{\Delta t^{(n-1)}}{(n-1)!}\frac{d^{(n-1)}\mathbf{r}_i(t)}{dt^{(n-1)}} + R_n(\Delta t^n). \tag{2.15}$$

This expansion indicates that the value and derivatives, at time t and increment Δt, are used to express the position function at time $t+\Delta t$. The error is the remaining part $\mathbf{R}_n$ of order of $(\Delta t)^n$. The symbol n denotes the first n terms where the highest derivative order is $(n-1)$. $\mathbf{R}_n$ will be dropped from equation 2.15 for numerical algorithm calculation. This means that error is expected by replacing dt with Δt. It, however, can be very small if Δt is small and n is large. In other word, the error order depends on the numerical algorithm and in principle, the accuracy can be adequate.

The Velocity Verlet algorithm starts from the position $\mathbf{r}_i(t)$ and velocity $\mathbf{V}_i(t)$ at the current step. From equation 2.15 by $n=3$ and with some substitution of physical relations, one can obtain

$$\mathbf{r}_i(t+\Delta t) = \mathbf{r}_i(t) + \mathbf{V}_i(t)\Delta t + \frac{1}{2}\left(\frac{\mathbf{F}_i(t)}{m_i}\right)\Delta t^2 \tag{2.16}$$

where $\mathbf{F}_i(t)$ is the force at the current time. The time step Δt is very small and acceleration is linear in this range. Then one can get the average acceleration from the $\mathbf{F}_i(t)$ and $\mathbf{F}_i(t+\Delta t)$. This acceleration can be used to determine the velocity at the next time step $(t+\Delta t)$ as

$$\mathbf{V}_i(t+\Delta t) = \mathbf{V}_i(t) + \frac{1}{2m_i}\left[\mathbf{F}_i(t) + \mathbf{F}_i(t+\Delta t)\right]\Delta t. \tag{2.17}$$

The dropped remaining terms are in $\mathbf{R}_3(\Delta t^3)$, thus the error is third order. The integration process of Velocity Verlet algorithm in time rang of (t_0, t_f) is

$$\mathbf{r}_i(t_0) \mapsto \mathbf{r}_i(t_0 + \Delta t) \mapsto \mathbf{r}_i(t_0 + 2\Delta t) \mapsto \cdots \mapsto \mathbf{r}_i(t_0 + h\Delta t), \tag{2.18}$$

where $t_f = t_0 + h\Delta t$. Velocity Verlet algorithm is commonly used in numerical simulations because the position $\mathbf{r}_i(t)$ and the velocity $\mathbf{V}_i(t)$ can be obtained at the same time. In our study on graphene interaction with noble gases, we have used this numerical algorithm to develop a Fortran code in which a subroutine is used to calculate the force of $\mathbf{F}_i(t + \Delta t)$.

It is seen from equations 2.16 and 2.17 that solving the differential equation of motion by means of Velocity Verlet algorithm requires both initial position vectors and initial velocity vectors. Therefore, initial position and velocity must be assigned to the system.

2.4 Periodic Boundary Conditions

The boundary conditions in atomistic modeling are very important. Because of small size of atomistic models, usually at the nanoscale, a large percentage of atoms are located at the boundary. These boundary atoms have completely different surrounding conditions and forces from the other atoms in material. Also, boundary atoms may vaporize to vacuum if there is no other medium surrounding the model, which may cause instability of the simulation system. This problem can be handled by using periodic boundary conditions to eliminate boundary effects.

Figure 2.5 shows a schematic of periodic boundary conditions (PBC) in a 2D problem. The central basic cubic box is replicated throughout space to form an infinite body. Take atom 1 in the center box for example; when it moves to box C, its image in box G enters the center box from the other side. And all the images

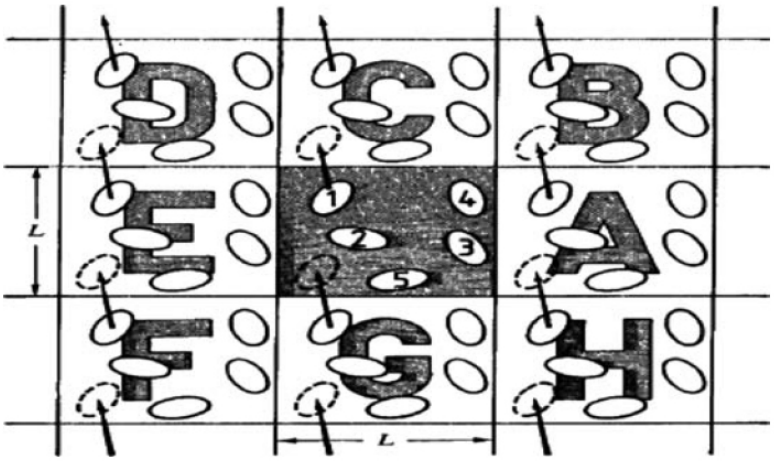

Figure 2.5: A two-dimensional periodic system [5].

of atom 1 move in the same way. By this means, the boundaries are eliminated.

PBC enables us to study the properties of materials through the simulation of a small number of atoms. Usually if the treatment is appropriate, PBC with the short-ranged interactions is a good approximation for the equilibrium properties apart from phase transitions.

2.5 Statistical Ensembles

Depending on the needs of simulation tasks, the atomistic system can be taken as different thermodynamic ensembles so a certain thermodynamic state can be controlled for the system during the simulation process. There are three main ensembles; NPT, NVE and NVT.

The NPT ensemble is an isobaric-isothermal ensemble, with the atom number N, the system pressure P, and the temperature T of the system remain constant throughout the simulation. To keep temperature constant, the simulation system should be connected to a thermostat (or thermal bath) to provide or absorb heat to maintain the desired constant temperature T_{set}, respectively. This can be done using Nose-Hoover thermostat. To control the system pressure, a barostat is used. Specifically, pressure is controlled using a piston, mimicking the volume pressure relationship. The volume changes with time and, in turn, changes the

instantaneous pressure so that the average pressure will converge approximately to the required value.

The NVE thermodynamic ensemble is also called microcanonical ensemble NVE. Where, the atom number N, the system volume V, and the total energy E of the system remain constant throughout the simulation.

The NVT ensemble is called canonical ensemble NVT. where, the atom number N, the system volume V, and the temperature T of the system remain constant throughout the simulation.

Moreover, Nose-Hoover thermostat is a way proposed for adjusting the system temperature, where a friction force term is added and the acceleration becomes

$$\frac{d^2\mathbf{r}_i(t)}{dt^2} = \frac{\mathbf{F}_i(t)}{m_i} - \gamma(t)\,\mathbf{V_i}(t). \tag{2.19}$$

The force expressed by the last term is a frictional force which is proportional to the atom velocity. If the system temperature is higher than the setting temperature, the corresponding kinetic energy and velocity are also higher than the setting ones. Thus more frictional force will be produced to reduce the acceleration and, in turn, to reduce the velocity and the system temperature. Here, $\gamma(t)$ is the frictional coefficient which is controlled based on the temperature difference between the system and the thermal bath as follows:

$$\frac{d\gamma(t)}{dt} = \frac{N_f k_B}{Q}\left(T(t) - T_{bath}\right) \tag{2.20}$$

where:

$$Q = N_f k_B T_{bath} \tau_T^2 \tag{2.21}$$

is the effective "mass" of the thermostat, τ_T is the thermostat relaxation time constant (normally in the range 0.5 to 2 ps), N_f is the number of degrees of freedom in the system and k_B is the Boltzmann constant.

2.6 Langevin Dynamics

Langevin dynamics is an approach for mathematical modeling of molecular systems. It is characterized by the use of simplified models where stochastic differential equations are used to omit some degrees of freedom with controlled temperature by a thermostat. For a system of N particles with masses M and coordinates $\mathbf{x} = \mathbf{x}(t)$ that constitute a time-dependent random variable, the displacement of a particle is governed by

$$d\mathbf{V} = -M^{-1}\nabla U(\mathbf{x})dt - \gamma\mathbf{V}dt + \sqrt{2\gamma k_B T}M^{-1/2}d\mathbf{W} \tag{2.22}$$

where $U(\mathbf{x})$ is the interaction potential, and $-\nabla U(\mathbf{x})$ is the force calculated from the potential, $\gamma\mathbf{V}$ is friction force due to the viscosity of the fluid, and the last term is related to random force due to impacts of fluid particles. The random numbers are delta-correlated with zero mean as

$$\langle dW(t)\rangle = 0, \tag{2.23}$$

$$\langle dW_i(t)dW_j(t')\rangle = \delta_{ij}\,\delta\left(t - t'\right). \tag{2.24}$$

Here, δ is the Dirac delta and $\langle ...\rangle_\xi$ is an average on distribution of the realizations of the random variable $dW(t)$.

The equation 2.22 is the Langevin equation of motion for a Brownian particle. When damping factor (γ) grows, particle spans the inertia all the way to the diffusive (Brownian) regime. From fluctuation dissipation theorem, we have an important result that relates the magnitude of friction (dissipation) with the strength of the random noise or fluctuating force (g) as

$$g = 2\gamma\, k_B T M^{-1}. \tag{2.25}$$

The balance between γ and g (friction and fluctuation) in last two terms of

equation 2.22 plays an important role. It can keep the system alive, otherwise excessive friction can drive any system to a completely dead state. This balance is necessary to have a thermal equilibrium state at long times.

2.6.1 Brownian Dynamics

Brownian dynamics is a simplified version of Langevin dynamics and corresponds to the limit where there is no distinct direction for applied forces on particle and average acceleration is zero. The viscosity term dominates the inertial one then we can ignore the acceleration term. This process is called "overdamped" Langevin dynamics, or Langevin dynamics without inertia as

$$0 = -\nabla U(\mathbf{x}) - \gamma \mathbf{V}(t) + \mathbf{f}_{random}(t). \tag{2.26}$$

Where $\mathbf{V}(\mathbf{x}) = -\frac{1}{\gamma}\nabla U(\mathbf{x})$ is the deterministic velocity, and $\eta(t) = \frac{1}{\gamma}\mathbf{f}_{random}(t)$ is the stochastic velocity. The latter has zero mean and its deferent components at different times are independent so its mean and covariance is

$$\begin{aligned} \langle \eta(t) \rangle &= 0, \\ \langle \eta_a(t)\, \eta_b(t') \rangle &= 2D\, \delta_{a,b}\, \delta(t - t'). \end{aligned} \tag{2.27}$$

Where the parameter D is related to diffusion of particles in the fluid. The covariance relation comes of this usual assumption that the probability distribution for the noise in velocity is Gaussian with the variance, σ^2, of $2D$.

2.6.2 Ornstein-Uhlenbeck Process

In this process Brownian particle is not subjected to any external potential then we can rewrite equation 2.22 as

$$d\mathbf{V} = -\frac{1}{\tau}\mathbf{V}dt + \sqrt{\frac{2k_BT}{M\tau}}d\mathbf{W} \tag{2.28}$$

where $\tau = 1/\gamma$, is relaxation time. With some mathematical concern about continuity and fast fluctuating function, we can obtain explicit formal solution for equation 2.28 as

$$\mathbf{V}(t) = \mathbf{V}_0 e^{-t/\tau} + \sqrt{\frac{2k_B T}{M\tau}} \int_0^t e^{-(t-t')/\tau} d\mathbf{W}(t'). \tag{2.29}$$

With some mathematical manipulations and using equations 2.23 and 2.24, we can acquire an important quantity that is the mean square displacement of particle from starting point as

$$\left\langle (\mathbf{x}(t) - \mathbf{x}_0)^2 \right\rangle_\xi = \tau^2 \left(1 - e^{-t/\tau}\right)^2 \left[{\mathbf{V}_0}^2 - \frac{k_B T}{M} \right] + \frac{2k_B T\tau}{M} \left[t - \tau \left(1 - e^{-t/\tau}\right) \right]. \tag{2.30}$$

In equilibrium the first term will be vanished that means $\left\langle {\mathbf{V}_0}^2 \right\rangle_{eq} = k_B T/M$, from equitation theorem. Then we can find this important result by approximation as

$$\left\langle \left\langle (\mathbf{x}(t) - \mathbf{x}_0)^2 \right\rangle_\xi \right\rangle_{eq} = \begin{cases} \frac{k_B T}{M} t^2 & t \to 0 \\ \frac{2k_B T\tau}{M} t & t \to \infty \end{cases}. \tag{2.31}$$

The result for short time ($t \to 0$) is the free particle form $x(t) - x_0 = V_0 t$, however the result for long times can be understood in compression with the diffusion result $\left\langle \left\langle (x(t) - x_0)^2 \right\rangle \right\rangle = 2Dt$ which gives Einstein result $D = \frac{k_B T}{\gamma}$. In general form, if we define the mean square displacement of particle as $\langle r^2 \rangle \propto Dt^\alpha$ then $\alpha = 1$ is diffusion, $\alpha > 1$ is supper diffusion and $\alpha < 1$ is subdiffusion.

2.6.3 Einstein Relation

Einstein predicted equation 2.32 that indicates Brownian motion of a particle in a fluid at a thermodynamic temperature T is characterized by a diffusion coefficient.

$$D = k_B T/\gamma \tag{2.32}$$

where k_B is Boltzmann's constant and γ is the linear drag coefficient on the particle (in the low-Reynolds regime applicable for small particles). Also, $1/\gamma$ is called mobility that is the ratio of the particle's drift velocity to an applied force. Equation 2.32 is Einstein relation connecting the fluctuation of noise to the dissipation in the medium.

2.7 Metropolis Monte Carlo Method

MC method uses a statistical method instead of the deterministic method used in MD. This method can be used for both statics and dynamics problems of atomistic systems.

What we need to do in the Monte Carlo method is to carry on routine sampling experiments which involve the generation of random numbers followed by a limited number of arithmetic and logic operations. The procedure of the so-called Metropolis algorithm is simple:

1. Draw random numbers and calculate the system energy $H(A)$ for configuration A.

2. Evolve the system to B state by random numbers then calculate the new system energy $H(B)$ for configuration B.

3. Accept or reject the new configuration according to an energy criterion.

4. Repeat last two steps until a certain number of trials is reached.

As for the energy criterion, it is easy to see that if energy $H(B)$ is less than $H(A)$, configuration B may be closer to the configuration with minimum potential energy, thus configuration B should be accepted, and then goto the next step. In the case where $H(B)$ is larger than $H(A)$ but not too much,there is a possibility that the $H(B)$ contribution will still be acceptable. To further accept or reject this configuration, draw random number p within $0 \leq p \leq 1$ and if the inequality showed in equation 2.33 is valid then it is accepted otherwise, it is rejected.

$$p < \ e^{-\frac{H(B)-H(A)}{k_B T}} \tag{2.33}$$

How to move from a previous to a new state is arbitrary, which makes this method widely applicable. However, one should have additional knowledge of the system behavior so it can be used easily for the generation of new stats. This is quite different from MD where the trajectories or the deformation pattern of each atom can be determined by establishing and solving the governing equations. Here, only the knowledge to guide the motion of the system is needed. In the original Metropolis method, one atom is chosen randomly to moved for generating a new configuration.

Chapter 3

GRAPHENE

3.1 Carbon

Carbon is a vital chemical element with fascinating properties. Where its graphite form is soft enough to be used in pencils, its diamond form is among the hardest materials. Carbon has been used from ancient times, in charcoal form for bronze production or as soot for writing. Carbon based nanomaterials refer to solid carbon materials with structural units on a nanometer scale in at least one direction. These materials have a large surface to volume ratio reflected in their unique and remarkable properties. The morphology of carbon nanomaterials ranges from fullerenes to carbon nanotubes, from graphene to nanocones or nanodiamonds.

Atomic number of Carbon is 6, therefore carbon atom has six electrons witch configuration of its electronic ground state is $1s^2 2s^2 2p^2$. The two electrons contained in the $1s$ orbital are strongly bound electrons and are called core electrons. The other four electrons which occupy the $2s^2 2p^2$ orbitals, are weakly bound electrons, and are called valence electrons. Two electrons are found in the $1s$ orbital close to the nucleus. These two electrons, which spin in opposite directions, have the lowest possible energy. Two electrons fill the $2s$ orbital and have opposite spin. The last two electrons partially fill the $2p$ orbital and have parallel spin. The $2s$ and the $2p$ electrons have different energy levels. The $2p$ electrons located in the outer orbital are the only electrons available for bonding to other atoms. These electrons are the valence electrons. In some carbon allotropes, four valence electrons participate in bonding the carbon atoms [12].

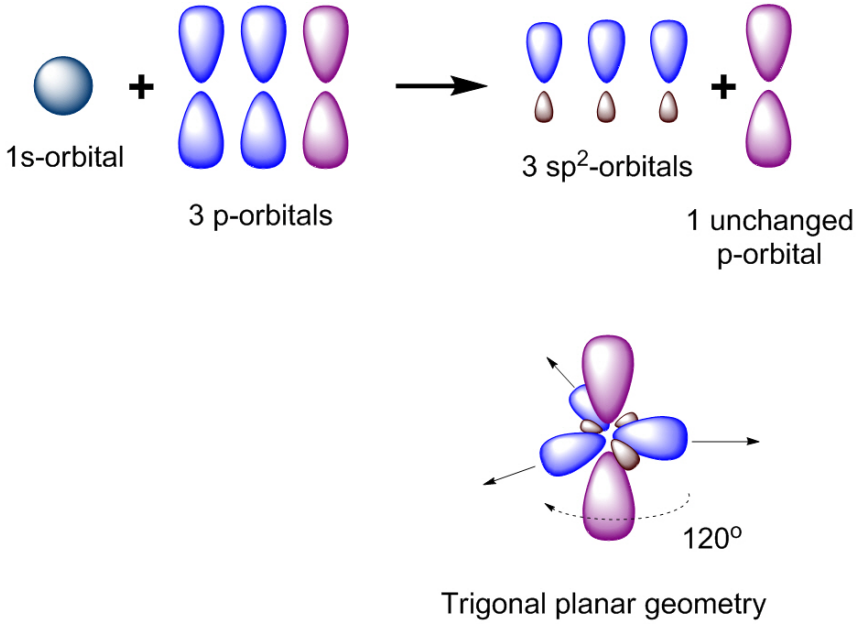

Figure 3.1: The sp^2 hybridization of carbon.

3.1.1 sp^2 Hybridization

The electron configuration of the carbon atom has to be changed from two to four valence electrons in order to allow carbon atoms to combine themselves. This modification implies mixing the orbitals and forming new hybrid atomic orbitals (Figure 3.1). The process is called hybridization. For carbon, one $2s$ electron is excited into the $2p$ orbital. The remaining $2s$ orbital is spherically symmetrical while the formed three $2p$ orbitals are oriented along the three axes perpendicular to each other. The way of combining these different orbitals gives different carbon hybridization types.

When carbon is in its excited state, sp^2 hybridization occurs. In this case, two $2p$ orbitals and one $2s$ orbital participate in the hybridization process and form three equivalent orbitals called sp^2 hybrid orbitals. These identical orbitals are in the same plane and their orientation is at 120° angle. Graphene structure comes from sp^2 hybridized carbon. The planar orientation of the sp^2 orbitals is available to form σ bonds with three other sp^2 hybridized carbon atoms. The unchanged $2p$ orbital of carbon is perpendicular to the plane containing the three hybridized orbitals and is available to form π bonds (Figure 3.2).

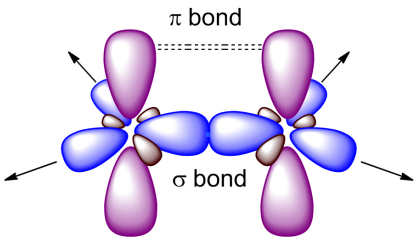

Figure 3.2: The illustration of σ and π bonds.

3.2 Carbon Allotropes

Allotropes are defined as structural modifications of an element. In other word, allotropes are different forms of chemical elements. Carbon has three main allotropes: carbyne, graphite and diamond. These three forms come from the three types of carbon hybridization; sp, sp^2, and sp^3 respectively. Carbon nanostructures, called Fullerenes, are a recently discovered forms of pure carbon and take the form of a hollow sphere, ellipsoid, or tube. Depend on the surface curvature of fullerene, hybridization falls between graphite (sp^2) and diamond (sp^3) [13]. Amorphous carbon is a carbon material with a variety of very short-range crystalline orders related to the graphite and diamond lattices. These disordered structures are formed because carbon is able to exist in three hybridizations.

3.2.1 Graphite

Graphite, the sp^2 hybridized form of carbon, its Greek root means to draw and to write. Graphite has a layered hexagonal planar structure. The hexagonal layers are held parallel with each other by Van der Waals forces. In each layer, the hexagonal lattice is formed by carbon atoms with separation of 0.142 nm, and the distance between planes is 0.335 nm [14]. The chemical bonds within the layers are covalent with sp^2 hybridization. Two forms of graphite are known, hexagonal and rhombohedral. Although these have graphene layers which stack differently, they have similar physical properties. The thermodynamically stable form of graphite is hexagonal graphite with an ABAB stacking sequence of

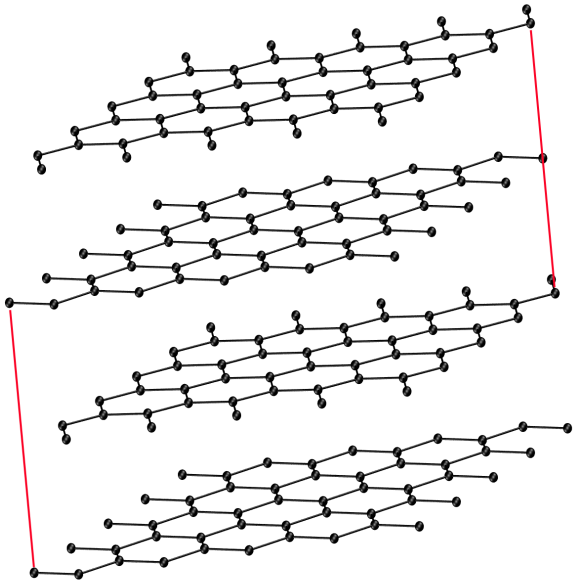

Figure 3.3: Graphite structure.

the graphene layers (Figure 3.3). The unit cell dimensions are $a = 0.2456\ nm$ and $c = 0.6708\ nm$ [15]. Hexagonal graphite is thermodynamically stable below approximately 2600 K and 6 GPa [16]. The rhombohedral graphite is thermodynamically unstable with an ABCABC stacking sequence of the layers. The unit cell constants are $a = 0.2566\ nm$ and $c = 1.0062\ nm$ [17]. This form has not been isolated in pure form. It is always mixed with the hexagonal form in variable amounts which can be increased up to 40% of rhombohedral content. Heating to above 1600 K progressively transforms rhombohedral graphite to hexagonal graphite, which shows that the hexagonal phase is thermodynamically more stable [18].

3.2.2 Nanostructures

Nanomaterial refers to material which has at least one nanoscale dimension. Although most micro-scale materials have similar properties to their bulk materials, the properties of nanoscale materials are substantially different from their corresponding bulk. The large surface to volume ratio and the nanometer size of the materials determine the characteristics which do not exist in the corresponding bulk materials, i.e. high surface energy, spatial confinement, reduced

imperfections. As a result, the material properties differ significantly on the nanometer scale. For example, the lattice constants are reduced, the photoluminescence process occurs [19, 20]. Carbon based nanomaterials cover various types of nanostructured carbons. The most representative ones are nanodiamonds, buckyballs, nanotubes and graphene.

By the late twentieth century, carbon science was widely considered to be a mature discipline and unlikely to attract scientists' major attention anymore. However, this situation changed in 1985 by the synthesis of buckyball, C_{60}, which led to the synthesis of carbon nanotubes and which drew attention to carbon science again [21].

3.2.2.1 Buckyball

Buckyballs or spherical fullerenes are a class of molecules composed entirely of carbon. They are zero-dimensional molecules since all dimensions are limited to nanoscale. Among the isolated stabile fullerenes are C_{60}, C_{70}, C_{76}, C_{80}, C_{84} and the series extends to gigantic fullerenes with more than 100 carbon atoms [22]. However, the most stable and also most famous buckyball is C_{60}. The Figure 3.4 shows the stricture of C_{60}. Some other fullerenes and gigantic fullerenes are presented in Figure 3.5 and Figure 3.6.

C_{60}s have average diameter of 0.68nm. The arrangement of their 60 carbon atoms resembles a football ball. Fullerenes are chemically stable, but they are less dynamically stable than graphite. The sp^2-hybridized carbon atoms must be bent to form closed spheres in comparison to planar graphite in which the atoms are at their minimum energy level. Fullerenes have been studied as a main material in various applications. Some examples are solar cells, photodetectors, field effect transistors, and additives in polymers.

3.2.2.2 Nanotube

carbon nanotubes (CNTs) are cylindrical fullerenes and similar to spherical fullerenes, the sp^2-hybridized carbon atoms must be bent to form cylindrical

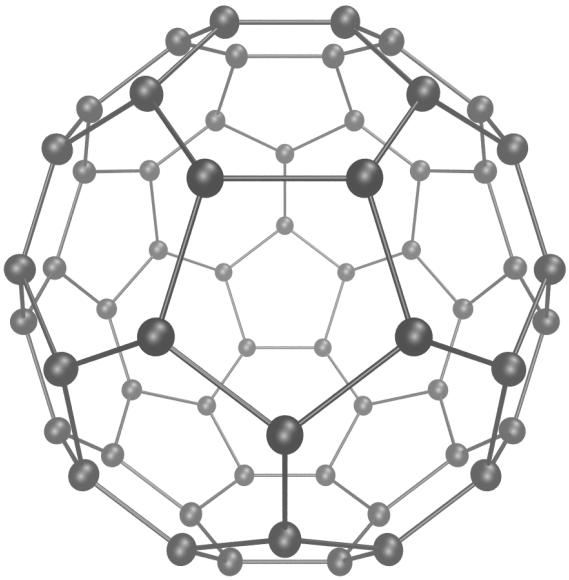

Figure 3.4: C_{60} stricture.

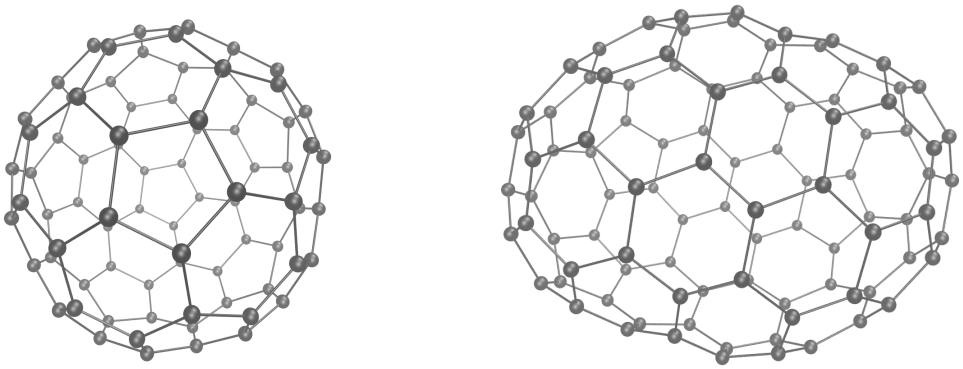

Figure 3.5: The stricture of C_{80} and C_{100} are shown in left and right sections respectively.

structures.

CNTs have a close relation to graphite as their structure can be conceptualized as a rolled-up monolayer of graphite. If only one layer forms the tube wall, the tube type is single walled carbon nanotube (SWCNT). CNTs with multiple rolled layers of graphite are called multi-walled carbon nanotubes (MWCNTs). MWCNTs have more than one wall or concentric tubes and the inter-tube spacing is 0.34nm, which corresponds to the interlayer distance of 0.35nm in graphite [23]. While the diameter of CNTs is in the range of several hundred nanometers down to 0.3nm [24], the length can be up to several centimeters [25]. Since only one

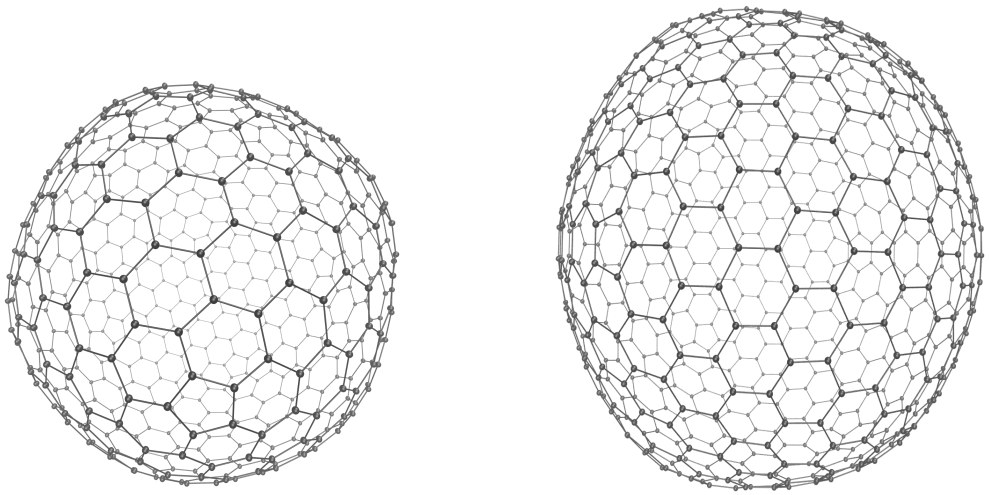

Figure 3.6: The left image represents C_{540} where the right one shows C_{720}

direction is not limited to nanoscale, CNTs are 1D nanomaterials. Following the concept of forming a carbon nanotube (CNT) by wrapping a one atom-thick layer of graphite into a cylinder, the structure of a SWCNT can be represented by a chiral vector C_h. The chiral vector C_h is defined by two integers $(n,\ m)$ as well as two base vectors a_1 and a_2 [26, 27]. The description of a specific SWCNT is given by $(n,\ m)$ indices when the graphite layer is bent in such a way that both ends of the vector lie on top of each other. When indices are taken in consideration as criteria, single walled carbon nanotubes (SWCNTs) are categorized as follows: armchair tubes $(n,\ n)$ when $m = n$, zig-zag tubes $(n,\ 0)$ for $m = 0$,and chiral tubes for any other $(n,\ m)$. The pair of integer indices $(n,\ m)$ determine the diameter and the chiral angle of the tube. The chirality of SWCNTs is related to their electrical properties. A tube is metallic when $(m - n)/3$ is an integer. All other SWCNTs are semiconducting. This means that m and n determine the diameter, the chirality, and the physical properties of SWCNTs [28] (Figures 3.7 and 3.8). Generally, for $(n,\ m)$ carbon nanotubes, the corresponding diameter, denoted here by d, can be acquired from equation 3.1.

$$d = \frac{\sqrt{3}\, a_0}{\pi}\sqrt{n^2 + nm + m^2} \tag{3.1}$$

where $a_0 = 1.42$Å is carbon-carbon bond length.

Using atomic force spectroscopy, CNTs are shown high values of tensile strength and Youngs modulus. Pressing on the tip of a nanotube causes bending without damaging the tip. When the force is removed, the nanotube returns to its original state. This property makes CNTs very useful as probe tips for high-resolution scanning probe microscope [29, 30]. CNT arrays have a lower thermal resistance which might serve as the interface material for thermal management in high power microelectronic devices [31]. Recently, CNTs have been used to support platinum in proton exchange membrane fuel cell electrodes [32, 33]. In lithium ion batteries, CNTs are used as electrodes because they exhibit high reversible capacity [34]. There are several other areas of technology where carbon nanotubes are already being used. These include composite materials, flat-panel displays, and sensing devices [35, 36, 37, 38].

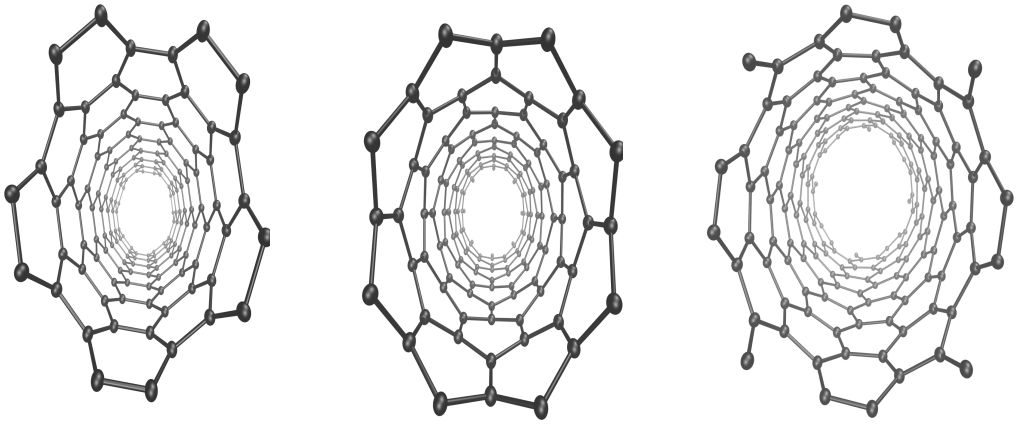

Figure 3.7: From left, the figure shows armchair, zigzag and chiral nanotubes respectively.

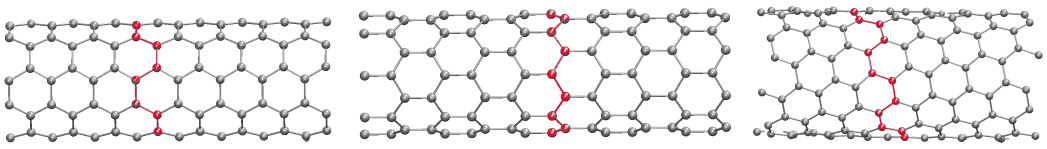

Figure 3.8: Side view of tree types of nanotubes; Armchair, Zigzag and Chiral from left to right

3.3 History of Graphene

Graphene has been studied theoretically for many years [39]. It was believed to be unstable, and presumed not to exist in the free state [40].

In the past it was predicted that strictly 2D crystals were thermodynamically unstable and could not exist because a divergent contribution of thermal fluctuations in low-dimensional crystals should lead to such large displacements of atoms that they become comparable to interatomic distances and dislocations should appear in 2D crystals [41] at any finite temperature. However, strong interatomic bonds can ensure that thermal fluctuations cannot lead to the generation of dislocations [41] and 2D crystals are intrinsically stabilized by gentle crumpling in the third dimension [42] which is reported from x-ray diffraction experiments [43]. The fact that 2D atomic crystals do exist and are stable under ambient conditions is amazing by itself.

Free standing graphene layers are difficult to be obtained, as they have the tendency to roll and form scrolls with respect to its lower energy state [44]. The first try to synthesize graphene was done by P.Boehm in 1962. In his report, the existence of monolayer of reduced graphene oxide flakes has been demonstrated [45]. The produced graphene had low quality due to incomplete removal of various functional groups. Between 1990 and 2004, many efforts were made to create very thin films of graphite by mechanical exfoliation [46] but nothing less than several tens of layers were produced. In 2004, A. Geim and K. Novoselov obtained single-atom thick graphene from bulk graphite by using a process called micromechanical cleavage [47]. To date, different methods have been developed to produce single-layer or few-layer graphene such as mechanical exfoliation [47], oxidation of graphite [48], liquid-phase exfoliation [49, 50], by chemical vapor deposition [51, 52], thermal decomposition of silicon carbide [53, 54], and cutting open nanotubes [55].

Unfortunately, many challenges have to be addressed in graphene synthesis for practical application since these methods suffer from limited controllability

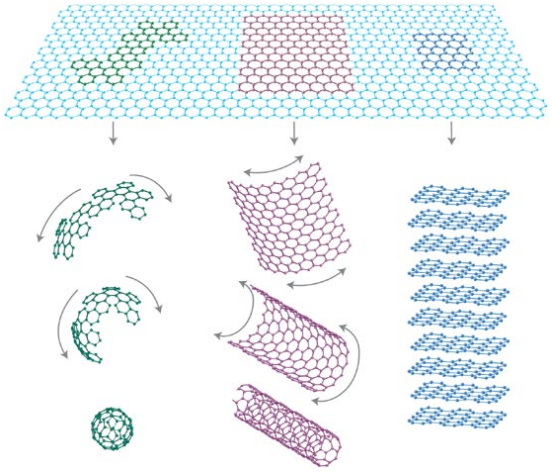

Figure 3.9: 0D fullerene molecules, 1D carbon nanotubes, and 3D graphite can all be thought of as being formed from 1D graphene sheets [56].

over the size, shape, edge, or location of graphene. The reason why graphenes have drawn so much attention to scientists arises from their remarkable properties. Experimental results from electronic transport measurements show that graphene has remarkably high electron mobility at room temperature [56]. A single layer of graphene has a high Youngs modulus of more than 1TPa [57] and is one of the stiffest known materials. It absorbs approximately 2.3% of white light demonstrating a very high opacity for an atomic monolayer [58]. The thermal conductivity of graphene was recently measured and exceeds the thermal conductivity for carbon nanotubes or diamond [59]. Graphene research is still at the very beginning and many experimental and theoretical results are expected to elucidate the physical characteristics of this important material.

Graphenes represent the 2D carbon nanomaterials formed by one or several monolayers of graphite. Similar to the graphite structure, the sp^2-bonded carbon atoms are densely packed in a honeycomb crystal lattice with the bond length of about 0.142nm. A single sheet is called a graphene sheet, while several graphene sheets, stacked with an interplanar spacing of 0.335nm, are called few-layer graphene. Graphene is the basic structural element of the other carbon based nanomaterials, as it can be wrapped up to form 0D spherical fullerenes or rolled to form 1D nanotubes (Figure 3.9) [56].

3.4 Properties of Graphene

Graphene layer is sp^2 hybridized honeycomb networks with strong in plane σ and weaker π bonds to the substrate. These different bond strength makes anisotropic elastic properties, where the sp^2 layer is stiff in plane and soft out of plane.

The covalent chemical bonds, sp^2 bonds, between the carbon atoms in a graphene sheet are among the strongest in nature. They are in fact even stronger than the carbon bonds in diamond. This exceptional property of the sp^2 bond causes the exceptional stability of graphitic systems, where they can be stable against extremely large thermal and electrical stresses which is very important for electronic applications and especially for nanoelectronics.

Moreover, the low temperature electronic mobility of graphite is of the order of 10^6 cm^2/Vs, exceeding silicon by about three orders of magnitude. The very strong bonds, combined with the low mass of the carbon atom causes a very high sound velocity resulting in a large thermal conductivity, which is advantageous for graphitic electronics. The most important graphene properties actually emerge from the unique band structure of this material as explained in detail below.

The electronic structure of graphene forms the foundation of its electronic properties. Graphene is not a metal, but it is essentially a giant organic molecule and technically a semi-metal. The electrons drive along π-bonds when they travel from one atom to other, then the precise geometry of the carbon atoms is essential for electron movement, that it is in contrast to metals. Also the electrons in graphene interact with the lattice in such a way that they appear to be massless while in metals, the electrons behave like free electrons.

A measurement of the mechanical properties of a single graphene layer, demonstrated that graphene is the hardest material known with the elastic modulus of 1.0 TPa [57].

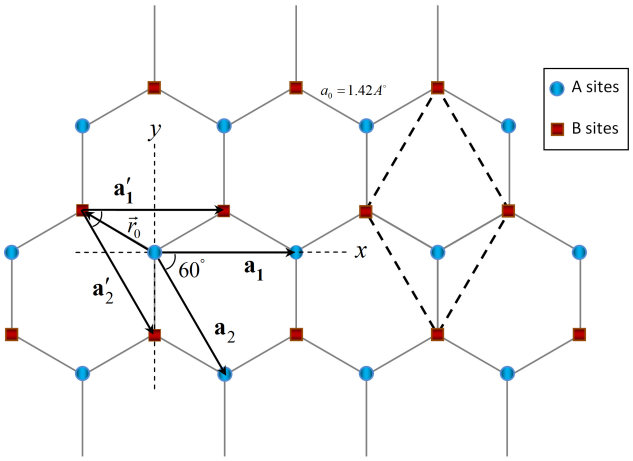

Figure 3.10: The direct lattice structure of 2D graphene sheet.

3.5 Graphene Structure

Graphene is a 2D sheet of carbon atoms in which each carbon atom is bound to its three neighbors to form a network then its crystalline structure is a flat monolayer of carbon atoms tightly packed into a 2D honeycomb lattice. The atomic orbitals of carbon atoms in graphene are sp^2 hybridized, with the three planar sp^2 suborbitals for each carbon atom being used to make three very strong planar σ bonds with other carbons atoms. This leads to forming planar hexagonal carbon rings, for example, in graphene with two dimensional honeycomb lattice of carbon atoms, all the $2p_z$ orbitals are used to form π bonds, which create delocalized electrons, and these are capable of moving freely. At low energy the delocalized electrons behave like 2D relativistic free particles. This is one of the reason behind graphene fantastic properties [60, 61, 62, 56, 63, 64, 65].

Graphene can be described by two sublattices (labeled A and B) while it does not correspond to a Bravais lattice. There is not a set of lattice vectors that their primitive translations cover all graphene sites. Technically, graphene can be described by two triangular Bravais sublattices (A and B) with two sets of lattice vectors (**a***s* and **a'***s*) as shown in Figure 3.10.

The primitive unit cell in such system of two triangular sublattices A and B is an equilateral parallelogram with two atoms (A and B) per unit cell (the dashed lines in Figure 3.10). A and B sites are the nearest neighbors of each others. The

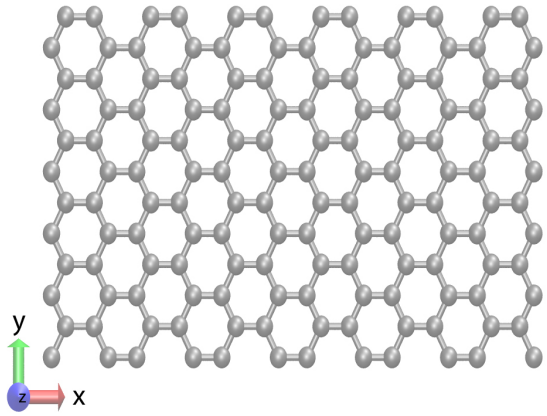

Figure 3.11: A honeycomb lattice structure showing both armchair (along x direction) and zigzag (along y direction) edges.

lattice vectors can be conveniently written as equations 3.2

$$\begin{aligned} \mathbf{a_1} &= \sqrt{3}\, a_0 \hat{i}, \\ \mathbf{a}_2 &= \tfrac{\sqrt{3}}{2} a_0 \left(\hat{i} - \sqrt{3}\, \hat{j} \right), \\ \mathbf{r_0} &= \tfrac{1}{2} a_0 \left(-\sqrt{3}\, \hat{i} + \hat{j} \right) \end{aligned} \tag{3.2}$$

There are two edges boundaries commonly seen in graphene crystallites: the armchair and the zigzag edges [56]. Figure 3.11 shows a honeycomb lattice that has armchair edges along the x direction and zigzag edges along the y direction. In many experimental and theoretical study [65, 66, 67, 68, 69] it has been shown that the graphene edges as armchair or zigzag plays a crucial role in their physical characteristics.

This crystallographic description of graphene is the basis for graphene electronic properties calculations. The individual electrons in graphene have both electric charge and spin. The electric charge is affected by the electric potential and electric field around the hexagonal carbon atoms lattice, and the spin of the electron is more related to the magnetic properties.

3.6 Graphene Nanoribbons

graphene nanoribbons (GNRs) are narrow rectangles like thin band made from graphene sheets and have widths on the order of nanometers up to tens of

nanometers, but they have arbitrarily long length. Graphene ribbons were firstly introduced as a theoretical model [67, 69, 68] to examine the edge and nanoscale size effect in graphene. However, they and are currently being investigated for their superior electrical, optical, mechanical, thermal, and quantum mechanical properties [56]. GNRs are a relatively new class of quasi-1D nanomaterials that can have metallic or semiconducting character.

There are two types of GNR, which are called armchair graphene nanoribbons (acGNRs) and zigzag graphene nanoribbons (zzGNRs). The ideal GNRs with infinite length in the x direction but finite width in the y direction, is an acGNR, while, one with infinite width along the y but finite in the x direction is a zzGNR as illustrated in Figure 3.12.

Some times, the GNRs are also labeled by the number of carbon atoms present in one of the width edges of the acGNR and zzGNR respectively. Let N_{ac} atoms be in the lateral edge of acGNR and N_{zz} in the lateral edge of zzGNR, then the nanoribbon can be conveniently denoted as N_{ac}-acGNR and N_{zz}-zzGNR respectively. The width of the GNRs can be acquired from the number of lateral atoms from equations 3.3.

$$\begin{aligned} w_{ac} &= \tfrac{N_{ac}-1}{2}\sqrt{3}\,a_0, \\ w_{zz} &= \tfrac{3N_{zz}-2}{2}a_0 \end{aligned} \tag{3.3}$$

where $a_0 = 1.42$ $\mathring{A}$. In Figure 3.12, the width of 10-acGNR along y direction is 11.07 $\mathring{A}$, while the width of 10-zzGNR along x direction is 19.88 $\mathring{A}$.

The electronic properties of GNRs are both width dependent and charity dependent. The charity here means edge structures, armchair or zigzag edges. Tight binding calculations predict that zigzag GNRs are metallic while armchairs can behave either like metal or semiconductor, depending on their width. With the width of between 2 and 3 nm, it is possible to produce nanoribbons with band gaps similar to Ge or InN. If larger bang gap ribbons are needed (like band gaps of Si, InP, or GaAs), their width must be reduced to 1-2 nm [70]. Indeed, experimental results show that the energy gaps have inverse relation with GNR

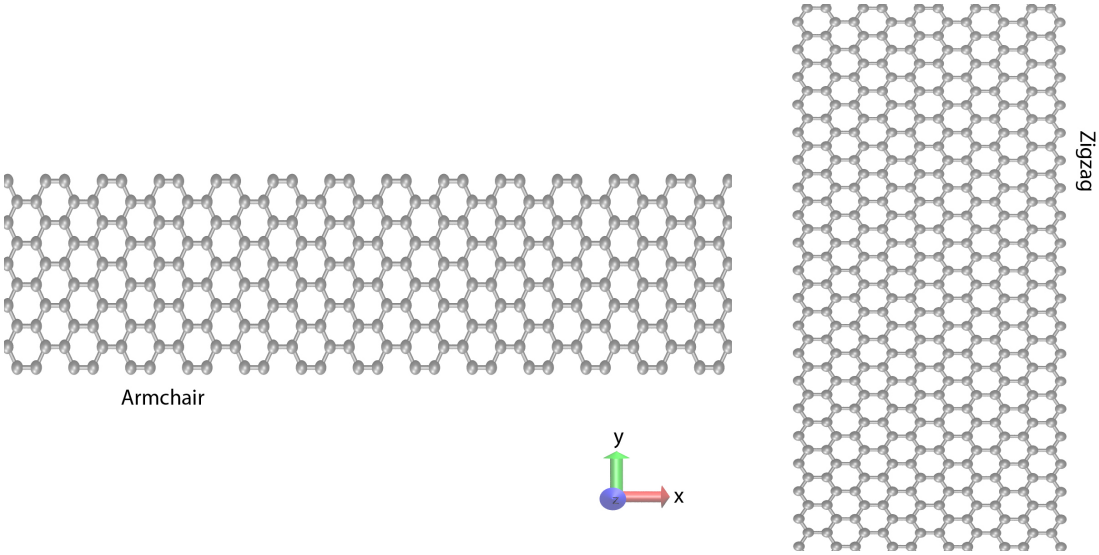

Figure 3.12: Left: Armchair GNR; Right: Zigzag GNR.

width [71].

In contrast to a large graphene sheet where electrons are free to move in a 2D plane, the small width of GNRs can lead to quantum confinement of electrons which restricts their motion to 1D along the length of the nanoribbons.

Fantastic properties of GNRs like their 2D structure, high electrical and thermal conductivity, and low noise make them a possible candidate to replace copper for integrated circuit interconnects. Some research is also being done to create quantum dots from quantum confinement by changing the width of GNRs [72].

3.7 Producing Graphene

Graphene was experimentally fabricated in its free state in 2004 when individual graphene samples of a few microns in width were isolated by micromechanical cleavage of highly oriented pyrolytic graphite (HOPG) [47]. By mechanical exfoliation of bulk graphite, one can produce graphene up to sizes of 100 μm (Figure 3.13), although graphene crystallites left on a substrate are extremely rare [73]. Raman spectroscopy can be used to discern graphene crystals with a few layers [74].

Two factors are important for future large-scale application of graphene as follows. Easy synthesis of larger quantities and control of the charity, morphology,

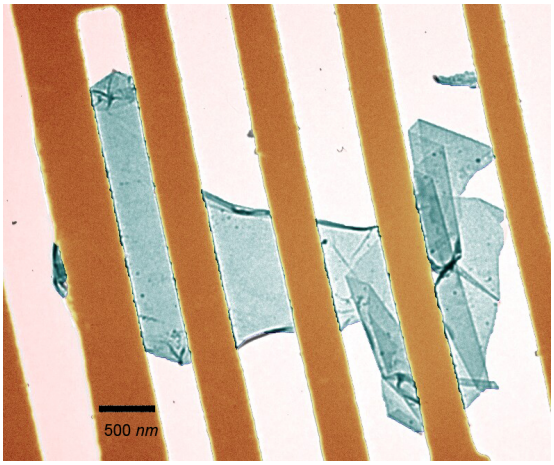

Figure 3.13: TEM image of a suspended graphene membrane. Electron diffraction shows that it is a single crystal. A strongly folded region are visible on the right [43].

and crystallinity of the edges of graphene nanoribbons, as their properties are depending on their charity, their size and the atomic structure of their edges [75]. Nanoribbons with wide of less than 10nm are semiconductors, independent of their edge structure [76].

Gram-scale production of graphene has been achieved [77] by reacting ethanol and sodium to an intermediate solid that is then pyrolyzed, yielding a fused array of graphene sheets that are dispersed by mild sonication. By a solution-based method for large-scale production, uniform films of single and/or few-layer chemically converted graphene can be produced over the entire area of a $silicon/SiO_2$ wafer [78]. Epitaxial graphene layers have been grown on single crystal 4-inch silicon carbide wafers [53] and a number of additional chemical methods are available for the production of graphene [79].

So far, a variety of methods have been reported for the synthesis of graphene with one atom thick as following:

1. The earliest and simplest method was mechanical exfoliation of HOPG, which is deposited on to a substrate like SiO_2 [47, 73]. Although this method is low cost, the graphene produced has the limited area and poor quality. It is a difficult and time-consuming method to synthesize graphene in large scale [80].

2. Chemical exfoliation from bulk graphite [81, 82]. In this method, strong acids are used to oxidized graphite then it is cleaved by means of rapid thermal expansion or ultrasonic dispersion, and subsequently the graphene oxide sheets were reduced to graphene. A serious disadvantage of this technique is that the oxidation process induces defects which would destroy the electronic properties of graphene.

3. Epitaxial growth on an insulator surface like SiC [83]. The graphene obtained showed poor uniformity and contained a multitude of domains.

4. chemical vapor deposition (CVD) on the surfaces of metals like Ni [51]. The CVD method is reported for the bulk production of long, thin, and highly crystalline graphene ribbons (less than $20-30\ \mu m$ in length), with widths from 20 to 300 nm and small thicknesses (2 to 40 layers) [84]. Moreover, N-doped graphene was first synthesized by a CVD method with the presence of CH4 and NH3 [85]. As doping accompanies with the recombination of carbon atoms into graphene in the CVD process, dopant atoms can be substitutionally doped into the graphene lattice, which is hard to realize by other synthetic methods.

5. The bottom up synthesis of these nanostructures may be feasible as noted by Hoheisel and collaborators [86].

3.8 Applications of Graphene

The experimental advances have increased the expectations for the use of graphene in high-tech devices. In parallel there is an increased interest in the physical properties of carbon nanostructures in general, due to their outstanding mechanical and electronic properties.

Besides, many efforts have been dedicated to study the electronic properties of graphene, because creating a gap could allow the use of graphene in field effect

transistors. Many mechanisms have been proposed with that purpose: nanopattering, creating quantum dots, using multilayer, doping, covalent functionalization [87] and applying mechanical stress [88, 89]. Recently Gui [89] proposed that graphene under a symmetrical strain distribution always leads to a zero band-gap semiconductor, and the pseudo-gap decreases linearly with the strain strength in the elastic linear regime. However, asymmetrical strain induces an opening of band gaps at the Fermi level.

Several unique electronic properties associated with these 2D crystals have been discovered [90]. In addition, it is known that carbon nanotubes have good sensor properties [56]. Recently, graphenes as highly sensitive gas sensors were also reported [91, 92, 93]. It was shown that the increase in graphene charge carrier concentration induced by adsorbed gas molecules could be utilized to make highly sensitive sensors, even with the possibility of detecting individual molecules. The sensing property is based on the changes in the resistivity due to molecules adsorbed on graphene sheet that act as donors or acceptors. The sensitivity of NH_3, CO, and H_2O up to 1 ppb (particles per 10^9) was demonstrated, and even the ultimate sensitivity of an individual molecule was suggested for NO_2. Furthermore, the preliminary works indicated that graphene have promising physical adsorption properties for hydrogen [94].

Apart from the interesting dependence of the electronic structure upon an electric field, this is a promising material for future spintronic devices, since it could work as a perfect spin filter.

In order to predict performance of zzGNR in future devices like gates, it is important to know how its electronic properties depend on stress. Some works related with the study of strain in graphene nanoribbons [95, 96] show that there is no important variation of the electronic properties of zigzag nanoribbons upon stress-strain effects, while Faccio et al [97] presented the first systematic determination of the Youngs modulus, Poissons ratio and calculated Shear modulus for graphene nanoribbons.

The current intense interest in graphene is driven by the high crystal quality

and ballistic transport at sub-micron distances as well as the behavior of quasi-particles as massless Dirac fermions so that the electronic properties are governed by quantum electrodynamics rather than the standard physics of metals based on the (non-relativistic) Schrodinger equation [98, 73].

This discovery has triggered enormous amount of interest on graphene both in fundamental and applied research. Graphene has shown promising applications as ultra-sensitive gas sensors, transparent electrodes in liquid crystal display devices, and large capacity electrodes in Li batteries [99].

Chapter 4

THE GRAPHENE'S IMPACT ON MOTION OF LIGHT ATOMS

Many phenomena in physical systems are described by the motion of Brownian particle in periodic potentials [100, 101]. One dimensional periodic potentials are the first studied case in the literature [102, 103]. The study of electrical conductivity of superionic solids and the effects of the surface of a crystals on the motion of adatoms are some standard text book examples [102]. The value of the damping factor in the Langevin equation plays an important role which classifies the motion as subdiffusive, diffusive and superdiffusive. Lacasta *et al* [104] studied the stochastic motion in a two periodic sinusoidal and random two-dimensional potential produced by general solid surfaces. They classified diffusive motions based on the coefficient of friction and different initial conditions for the velocities.

One of the newly discovered honeycomb structures, which is a one atom-thick-planar sheet made of carbon atoms (i.e. graphene), was discovered in 2004 [47]. This newly discovered material has various interesting electrical and mechanical properties [56, 65, 105]. Applying a pressure difference across the membrane, a monolayer graphene membrane is impermeable to standard gases including helium [106]. This pressurized graphene membrane is the thinnest balloon in the world. This nano balloon is stable under large pressure differences across the membrane.

Transmission electron microscopy can visualize the images and dynamics of light atoms deposited on a single-layer graphene sheet [107]. Suitable force fields provide real inter-atomic interactions between the graphene sheet and external inclusions. One of the well-known force fields is LJ pairwise potential which is

parameterized for different types of atomic and molecular systems. For example, a LJ pair wise potential for C_{60}-graphene interaction and C_{60}-carbon nanotubes interaction, which has provided theoretically viable and experimentally desirable results, was introduced in Ref. [108]. Also several van der Waals parameters for physical adsorption of C_{60} on the graphite and other substrates were formulated using a continuum rigid body model for C_{60} and a continuum dielectric media for the graphite by Girad *et al* [109]. An analytical study which has included three main parts for the interaction between C_{60} and various substrates such as graphite was presented by Gravil *et al* [110]. They showed that the adsorption energy and the height of the molecule center above the surface are 968 meV and 6.55 Å, respectively. The equivalent results for showing the diffusive motion of C_{60} on graphene were obtained by assuming LJ potential between carbon atoms of graphene and C_{60} [111] using molecular dynamics simulation. In contrast, alkali metal atoms form nanoclusters on the graphene sheet which is caused by the deep potential well between alkali metals [112].

The aim of this study is to provide further insights into the stochastic motion of noble gases on a graphene sheet. We show that depending on the atom type on the monolayer graphene, different two dimensional periodic potential (2DPP) is produced at a fix height. Close to the surface (<1Å) , the 2DPP has sharp positive peaks where in closer inspection a honeycomb structure is revealed. Far from the sheet, the 2DPP goes to a flat surface. We estimated the equilibrium distance and the corresponding binding energies for noble gases (He, Ne, Ar and Xe) on graphene. Furthermore, we show that the variation of the interaction potential between the graphene sheet and external atoms along the z-direction, although similar to the LJ function, cannot fully account for it. The effects of the coefficient of friction and binding energies on the trajectories of the atoms are also studied.

This Chapter is organized as follows. In section 4.1 we explain the atomistic model and details of 2DPP. Section 4.2 contains discussion on the Langevin dynamics and the corresponding numerical solution with several limits for coefficient

of friction and different noble gas atoms.

4.1 The periodic potential

Carbon atoms in graphene sheet are densely packed in a honeycomb crystal lattice Fig. 4.1. The carbon-carbon bond length, a_0, is 1.42 Å. Since a flat honeycomb lattice is not a Bravais lattice, one should divide honeycomb lattice into a couple of sublattices, say A-lattice and B-lattice. Therefore two sets of primitive vectors can specify the A and B sites on a graphene sheet.

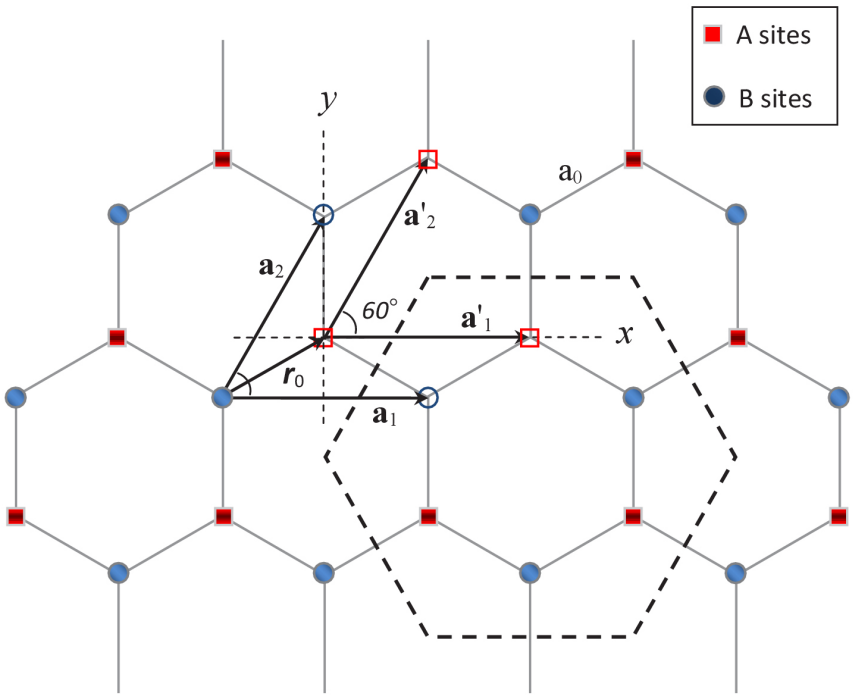

Figure 4.1: The honeycomb lattice is not a Bravais lattice. Two A and B lattices are Bravais lattice separately. Dashed honeycomb is one of favorable path for diffusion of the rare gas atoms.

Two-dimensional position vectors are written in A and B lattices as follows:

$$\mathbf{r}_A = p\,\mathbf{a}_1 + q\,\mathbf{a}_2, \tag{4.1}$$

$$\mathbf{r}_B = p'\,\mathbf{a}'_1 + q'\,\mathbf{a}'_2, \tag{4.2}$$

$$\tag{4.3}$$

Where $\mathbf{a}_1$ and $\mathbf{a}_2$ are the primitive vectors in the A-lattice and $\mathbf{a}'_1$, $\mathbf{a}'_2$ are the primitive vectors in the B-lattice. The magnitudes of all primitive vectors are equal to $\sqrt{3}\,a_0$. In the above equations $p(p')$ and $q(q')$ are two integers which count A-lattice (B-lattice) sites . On the other hand, one can write the primitive and position vectors in the Cartesian coordinate system whose origin is assumed to coincide with the origin of the primitive vectors in A-lattice:

$$\mathbf{a}_1 = \sqrt{3}\,a_0\,\hat{i}, \tag{4.4}$$

$$\mathbf{a}_2 = \frac{\sqrt{3}}{2}\,a_0\,\hat{i} + \frac{3}{2}\,a_0\,\hat{j}, \tag{4.5}$$

$$\mathbf{r}_0 = \frac{\sqrt{3}}{2}\,a_0\,\hat{i} + \frac{1}{2}\,a_0\,\hat{j}, \tag{4.6}$$

Where two lattices are connected by vector $\mathbf{r}_0$. Any space point, p, in the Cartesian coordinate system can be written as $\mathbf{r} = x\,\hat{i} + y\,\hat{j} + z\,\hat{k}$. The distance between A-lattice and B-lattice points and the space point, p, are given by

$$|\mathbf{r} - \mathbf{r}_A| = ((x - \sqrt{3}\,p\,a_0 - \frac{\sqrt{3}}{2}q\,a_0)^2 + (y - \frac{3}{2}q\,a_0)^2 + z^2)^{1/2}, \tag{4.7}$$

$$|\mathbf{r} - \mathbf{r}_B| = ((x - \sqrt{3}\,p\,a_0 - \frac{\sqrt{3}}{2}q\,a_0 - \frac{\sqrt{3}}{2}a_0)^2 + (y - \frac{3}{2}q\,a_0 - \frac{1}{2}a_0)^2 + z^2)^{1/2}. \tag{4.8}$$

Note that here we put $p = p'$ and $q = q'$ for counting purposes. The LJ potential provides both the general repulsive and attractive nature of the interaction between an uncharged noble gas deposited on the graphene sheet. The LJ potential is the widely used potential in various simulations for two interacting uncharged particles, i.e. $U(r) = 4\varepsilon((\sigma/r)^{12} - (\sigma/r)^6)$, where r is distance between two atoms, ε is the depth of the potential well, and σ is the distance at which the potential becomes zero. To model the interaction between two different types of atoms such as carbon and argon, we adjust LJ parameters using the equations $\varepsilon = \sqrt{\varepsilon_1\varepsilon_2}$ *and* $\sigma = \frac{\sigma_1+\sigma_2}{2}$. In Table 4.1 we have listed our used parameters for

Table 4.1: The adjusted parameters of the LJ potential for noble gases [113].

	He	Ne	Ar	Xe
$\varepsilon(meV)$	0.878	3.079	10.23	19.4
$\sigma(\mathring{A})$	2.56	2.74	3.405	4.07

four noble gases [113]. For carbon atoms $\sigma = 3.369$ Å and $\varepsilon = 2.63$ meV [112].

The derivative of the LJ potential with respect to the position vector gives the force between atoms. Total force acting on an atom over the graphene sheet includes both contributions from A and B lattices. The distance between each graphene atom and any guest atom should be included as well. Considering both contributions, the potential function can be written as

$$U(\mathbf{r}) = \sum_{A} U(|\mathbf{r} - \mathbf{r}_A|) + \sum_{B} U(|\mathbf{r} - \mathbf{r}_B|). \tag{4.9}$$

Substituting both distances (Eq. (4.7) and Eq. (4.8)) in Eq. (4.9) helps to rewrite the potential function for interaction between a monolayer graphene at $z = 0$ and an atom located at $(x, y, z > 0)$:

$$\begin{aligned} U_p(\mathbf{r}) = &\sum_{-p}^{p}\sum_{-q}^{q} 4\varepsilon \left[\left(\frac{\sigma}{|\mathbf{r} - \mathbf{r}_A|}\right)^{12} - \left(\frac{\sigma}{|\mathbf{r} - \mathbf{r}_A|}\right)^{6}\right] \\ &+ \sum_{-p}^{p}\sum_{-q}^{q} 4\varepsilon \left[\left(\frac{\sigma}{|\mathbf{r} - \mathbf{r}_B|}\right)^{12} - \left(\frac{\sigma}{|\mathbf{r} - \mathbf{r}_B|}\right)^{6}\right]. \end{aligned} \tag{4.10}$$

Note that the difference between the potential energy of $p = q = \pm 16$ and $p = q = \pm 17$ is less than 10^{-4} meV. We used $p = q = \pm 20$ as a sufficient high and low limits for summations in Eq. (4.10) (the same limits were used for p' and q').

For bilayer graphene, we add another layer at z=-3.4 Å below the monolayer

graphene with a shift equal to $a_0/2$ in x components for all A and B sites of monolayer graphene. The third layer is put at z=-6.8 Å with the same x and y coordinates as used for the first layer. The LJ potential between bilayer (triple layer) graphene and an atom at $(x, y, z > 0)$, instead of two terms in Eq. (4.10), is written with four (six) terms considering the above mentioned shifts.

Figure 4.2 shows the 2DPP energy surface scaled by K_BT , U($\mathbf{r}$) at z=3.5 Å for an Ar atom above monolayer graphene. The unit of length is a_1. It is clear that the potential barrier between two neighbor wells are smaller than K_BT and goes to zero for higher height.

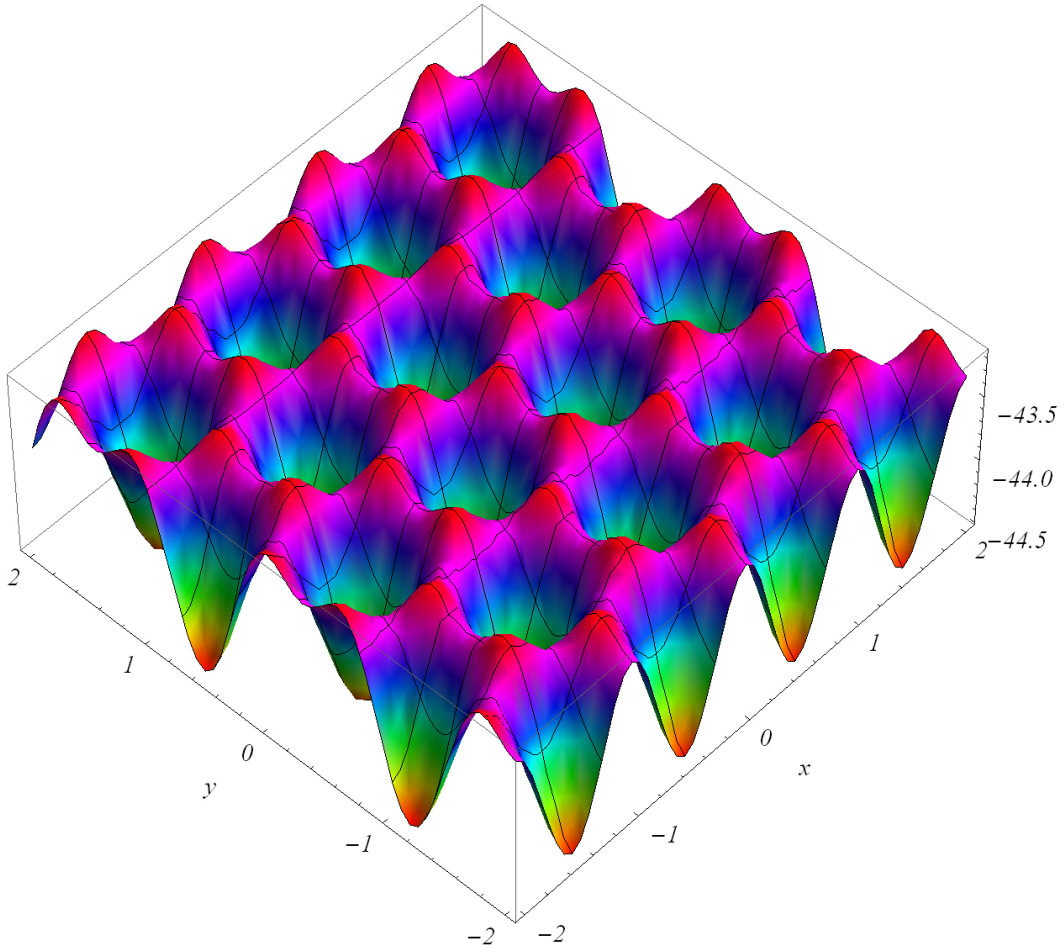

Figure 4.2: The two-dimensional potential energy surface for an Ar atom above monolayer graphene. Unit of length is a_1 and energy unit is K_BT.

Variation of 2DPP at the fix point in the $x - y$ surface (V) versus z is also interesting. The Figure 4.3 shows variation of the potential energy scaled by

Table 4.2: Equilibrium distances, z_{min}, and the binding energies, D, of noble gases on a monolayer graphene sheet.

	He	Ne	Ar	Xe
$2^{1/6}\sigma(\mathring{A})$	3.3275	3.4285	3.8018	4.1756
$z_{min}(\mathring{A})$	2.906	2.988	3.347	3.696
D/K_BT	-0.827	-1.554	-3.401	-5.576

K_BT versus z at x=0.5a_1 and y=-$\sqrt{3}$/6a_1. The effects of different points is not noticeable. As can be seen, elements with smaller ε (Xe) show deeper potential (and vice versa) which produce stronger binding energy between the elements and the monolayer graphene. The functionality of these profiles is not the same as the LJ function. Moreover, the equilibrium distances are smaller than $2^{1/6}\sigma$. Therefore, the equilibrium distance between a carbon atom and a noble gas atom is larger than the equilibrium distance between a sheet of carbon and a noble gas atom. In Table 4.2, values for $2^{1/6}\sigma$ using $\sigma = \frac{\sigma_1+\sigma_2}{2}$, the equilibrium distances z_{min} and binding energies D are listed. Figure 4.4 shows the variation of the potential energy along z axis, similar to Figure 4.3 except for bilayer graphene. Figure 4.5 compares the potential energy along the z direction at x=0.5a_1 and y=-$\sqrt{3}$/6a_1 for monolayer, bilayer, and triple-layer graphene for Ar and Xe atoms. As can be seen from this Figure adding extra layers changes the potential energy only slightly. The difference between monolayer and bilayer at minima is about 0.35 K_BT. Indeed, the van der Waals interaction between uncharged noble gases on the monolayer graphene and graphite (more than two layer) and consequently the type of the motion of those atoms on those materials are more or less the same. Therefore, in the next section we only focus on the monolayer graphene. Note that by increasing the height, the potential energy surface goes to a flat surface [111].

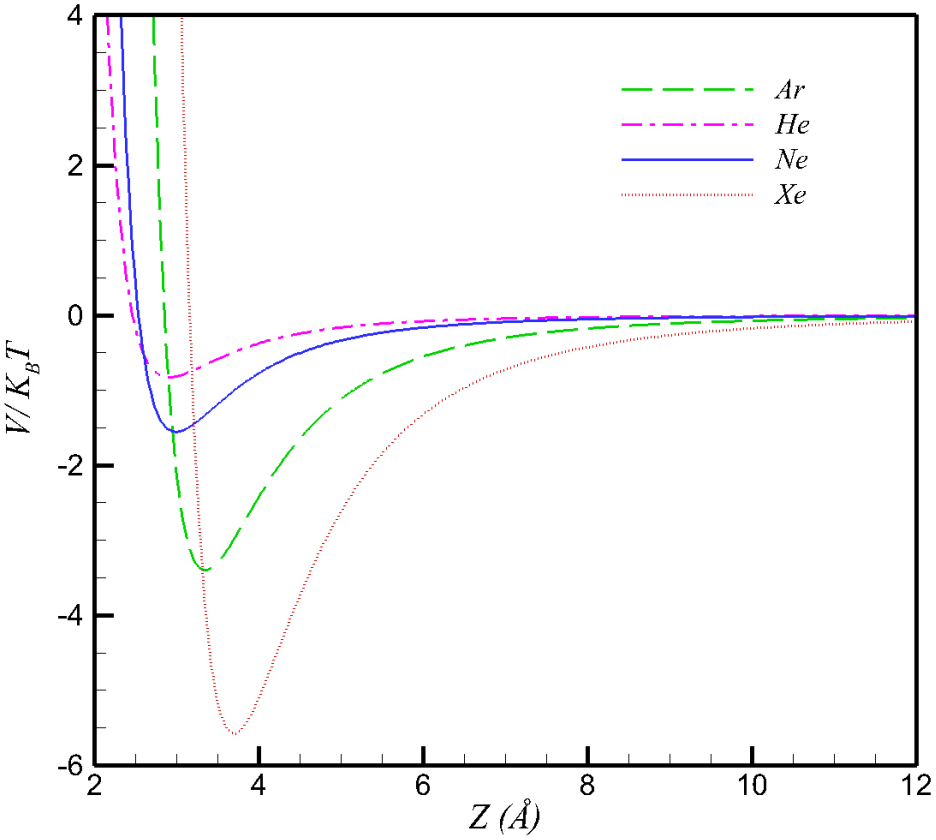

Figure 4.3: Variation of the potential energy versus z for four noble gas atom on the monolayer graphene at x=0.5a_1 and $y = -\sqrt{3}/6a_1$.

4.2 Langevin dynamics

In this section the surface diffusion of a particle with mass m (noble gas atom) at a fix height z within the produced two-dimensional LJ potential by monolayer graphene is studied. This motion occurs in the presence of thermal noise and dependent dissipation. The Langevin equation which describes the stochastic two-dimensional trajectory, $\mathbf{r}$, is written as

$$\ddot{\mathbf{r}} = -M^{-1}\frac{\partial U(x, y, z = const.)}{\partial \mathbf{r}} - \gamma\,\dot{\mathbf{r}} + \sqrt{2\gamma K_B T} M^{-1/2}\mathbf{dW}(t), \qquad (4.11)$$

Where the first two terms refer to the drift velocity, γ is the coefficient of

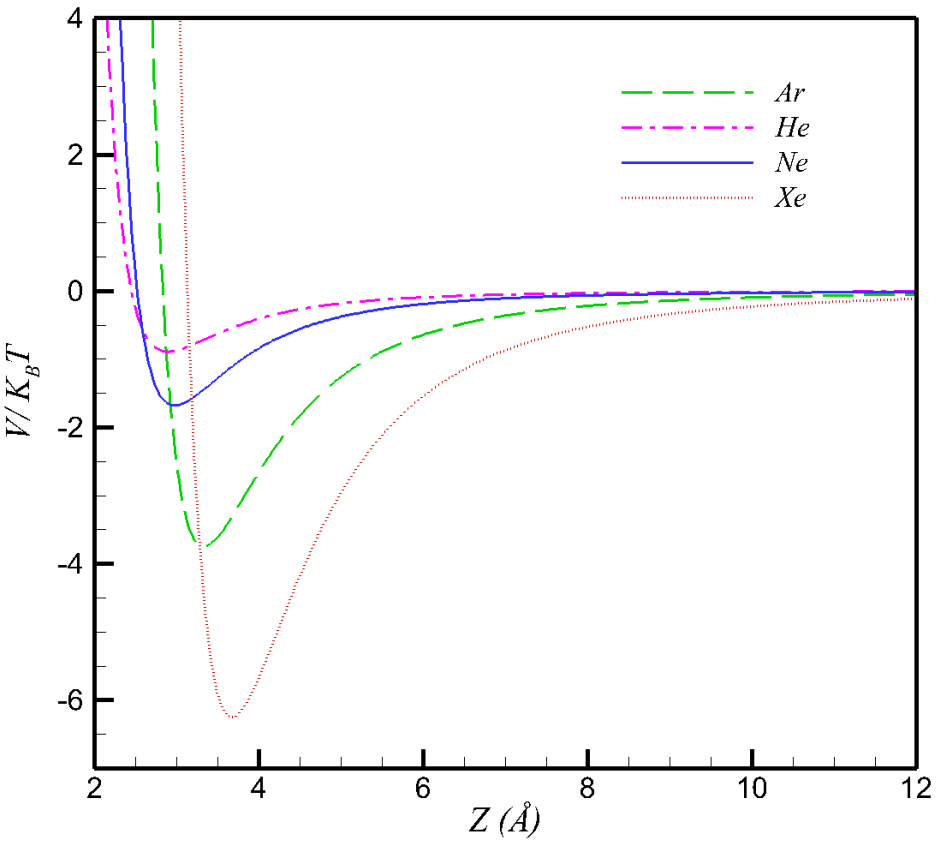

Figure 4.4: Variation of the potential energy versus z for four noble gas atom on the bilayer graphene (middle) at x=0.5a_1 and $y = -\sqrt{3}/6a_1$.

friction, and the term, $dW(t)$, is a collection of Gaussian Wiener processes with the mean and variance given by

$$\langle dW(t) \rangle = 0, \tag{4.12}$$

$$\langle dW_i(t)\, dW_j(t') \rangle = \delta_{ij}\delta(t - t'). \tag{4.13}$$

In the diffusive motion the mean square displacement (msd) is $< r^2(\tau) > \sim D\tau^{\alpha}$, where for normal diffusion $\alpha = 1$ while in different time-dependent motion α is either greater than one -superdiffusive motion- or less than one -subdiffusive motion- [104]. The average $\langle ... \rangle$ designates a time-average or an ensemble-average

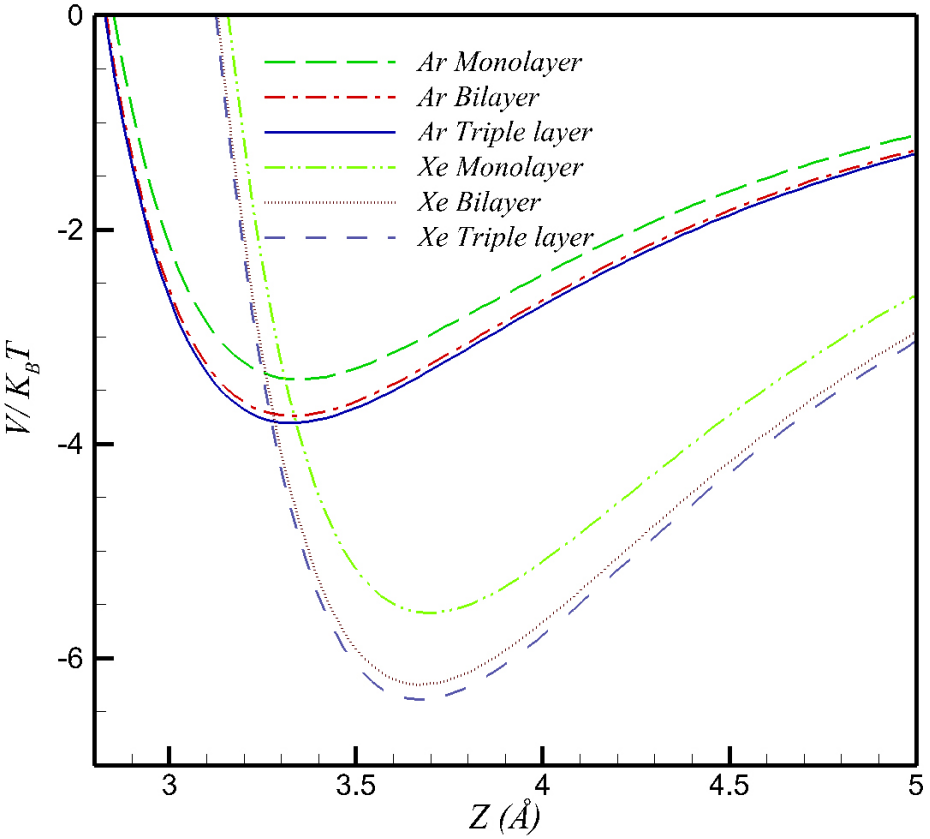

Figure 4.5: This figure shows the potential energy for Ar and Xe above monolayer, bilayer and triple layer graphene.

over several trajectories. To calculate msd at increment τ, we averaged over N position vectors points of a trajectory of the particle and used the following relation

$$\frac{1}{N-\tau}\sum_{\alpha=1}^{N-\tau}[\mathbf{r}(t+\tau)-\mathbf{r}(t)]^2. \tag{4.14}$$

To solve Eq. (4.11) numerically, we used a_1 as the unit of length, and K_BT for the unit of energy, molecular mass of noble gasses i.e.; m as the unit of mass, $\chi = \sqrt{\frac{m}{K_BT}}a_1$ for the time unit and $\eta = (m\chi)^{-1}$ for the unit of γ. Note that by choosing mass of noble gasses as the unit of mass, two other units, i.e. χ and η, become different for each element. For example γ =1.0 in the simulation for He in real dimension is equal to $\frac{a_1}{\sqrt{4.0K_BT}}$ while for Xe it is equal to $\frac{a_1}{\sqrt{131.29K_BT}}$. Therefore,

the unit of γ for heavy atoms is smaller than the one for light atoms. For time unit, heavy atoms have larger χ. We set time step equal to 0.5 fs. The initial velocity randomly were chosen from (0,0.01) range and the initial position was set at the origin. One can use different initial conditions for the velocities [104]. The system has infinite size but technically one should care about the calculation of the force exerted on the particle when it is far from the origin because of limiting p and q (also for p' and q') in Eq. (4.10) to ± 20. Due to the periodic nature of 2DPP, we found the equivalent coordinates for far-center particles within the first primitive cells for both A-lattice and B-lattice and computed the force exerted on the particle.

4.2.1 Effect of coefficient of friction and binding energy

We have solved the Langevin equations for the stochastic motion of Xe and He atoms because they have the largest and the smallest ε, respectively. These atoms have the maximum and minimum binding energy to the graphene sheet too (see Figure 4.3). Here two coefficients of friction $\gamma = 1,\ 10$ are used. The trajectory of Xe atom above the monolayer graphene at z=1.2 and z=1.4 for two γ values are shown in Figures 4.6 and 4.7. Close to the surface, higher γ localizes the motion inside the honeycombs having different sizes in comparison to the original monolayer graphene honeycombs. Two of these larger honeycombs are shown in the top panel of Figure 4.7 (see dashed black honeycomb in Figure 4.1 as well). Each side of these honeycombs has unit length ($=a_1$). As can be seen from this figure, it is interesting to note that the atom moves to another honeycomb via the valleys only. The motion with higher γ is diffusive which is characterized by small steps in the top panel of Figure 4.7. Figure 4.6 shows trajectories correspond to small friction, $\gamma = 1$, and clearly shows the preponderance of long tracks along valleys direction between sites before turning to another (particularly for smaller z). Far from the surface, the particle is more free and it is spread in $x-y$ surface. Despite the fact that these behaviors are common in the periodic two dimensional potentials, they have not been observed in random potentials [104].

The motion of He atom at a fixed height above the graphene is more free with respect to the motion of Xe atom. Figure 4.8 shows the two dimensional trajectory of a He atom above the graphene sheet at $z = 1.2$ for $\gamma = 1,\ 10$. We observe that the motion is different from the case of Xe atom exhibited in the top panels of figures 4.6 and 4.7. This is related to different LJ potential parameters for these two elements. Due to smaller minima (see Figure 4.3) in He-graphene interaction, it is expected that at $z < 1.2$ He localizes within honeycombs.

The evolution of msd for different γs is shown in Figure 4.9. After equilibration of the system, we used equation (4.14) to calculate the msd. Here heights were fixed at z=1.2. Irrespective of γ's and the type of elements in early stages of time, the motion is almost ballistic ($\alpha \cong 2$) but at very long times the motion becomes diffusive and αs are close to unit. The smaller the γ values the more delay in reaching the diffusive regime. Also for a specific γ value, the smaller binding energy in He case shows a diffusive motion later with respect to the motion of Xe atom. The unusual fluctuations in msd for Xe atom have occurred around 10^3 time steps which is equal to 0.5 ps. This is a typical time for going to a nearest minimum well. At very long times one can calculate two diffusion constants using $D = \frac{<r^2(\tau)>}{4t}$ which are in the order of 1 m^2/s for He and around 0.1 m^2/s for Xe atom for large γ. Note that Figures 4.9 show the variation of $< r^2 >$ versus simulation times step (not the real time) in loglog scale. We found the slopes by using $\alpha = Log(\Delta y)/Log(\Delta x)$ relation, where Δy and Δx are the vertical and horizontal sides of the triangles in the figure.

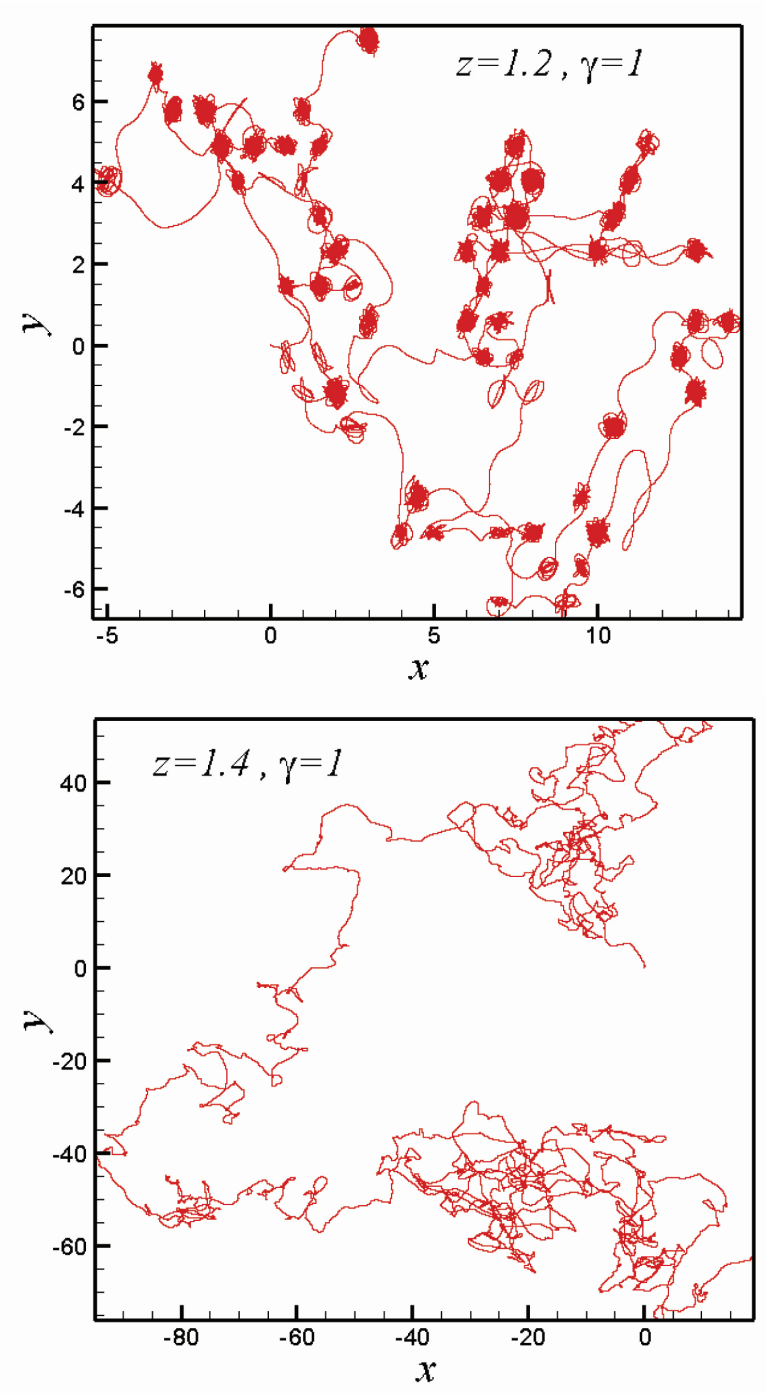

Figure 4.6: Two dimensional trajectories of Xe atom on the monolayer graphene with coefficients of friction equals $\gamma = 1$ at two different heights according to the legends. Total time of simulations is 5 ns and the unit of length is a_1.

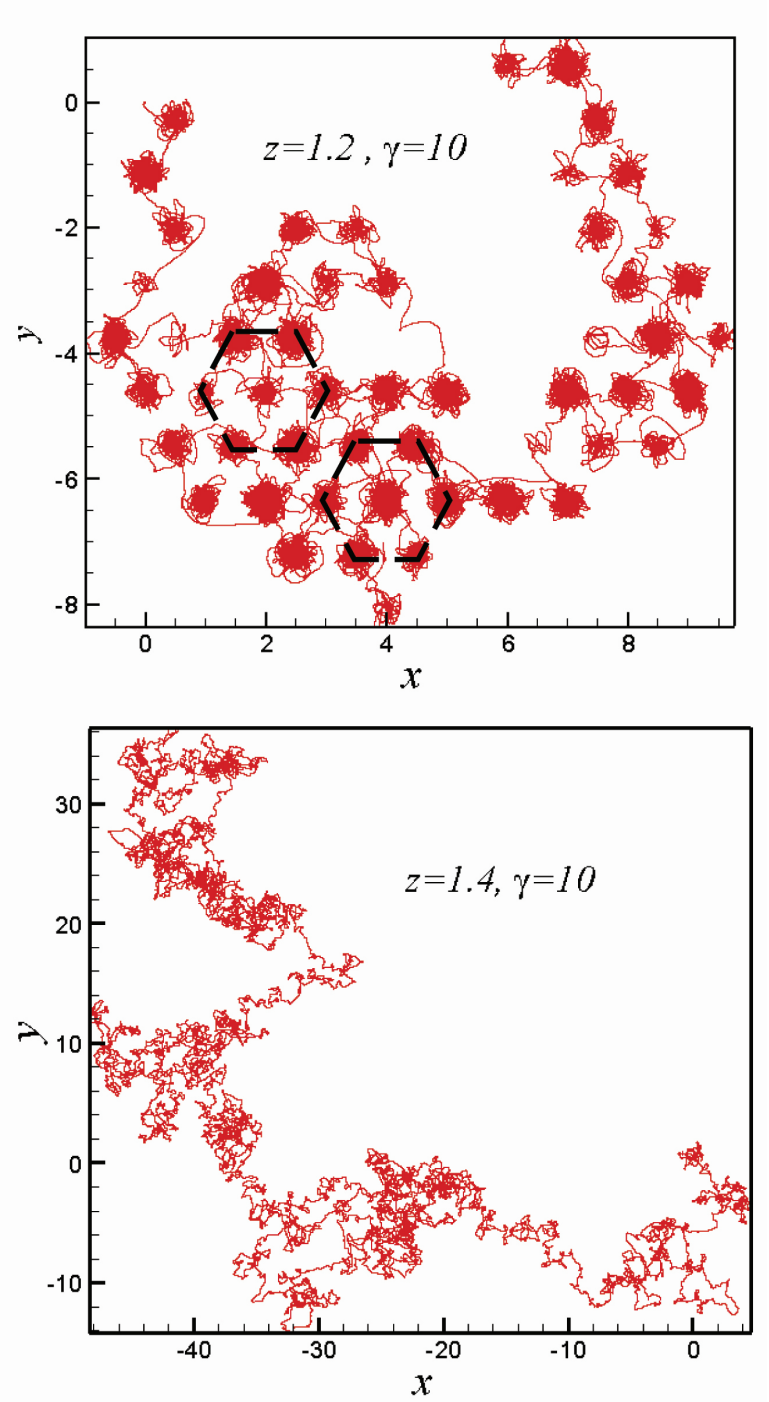

Figure 4.7: Two dimensional trajectories of Xe atom on the monolayer graphene with coefficients of friction equals $\gamma = 10$ at two different heights according to the legends. Total time of simulations is 5 ns and the unit of length is a_1.

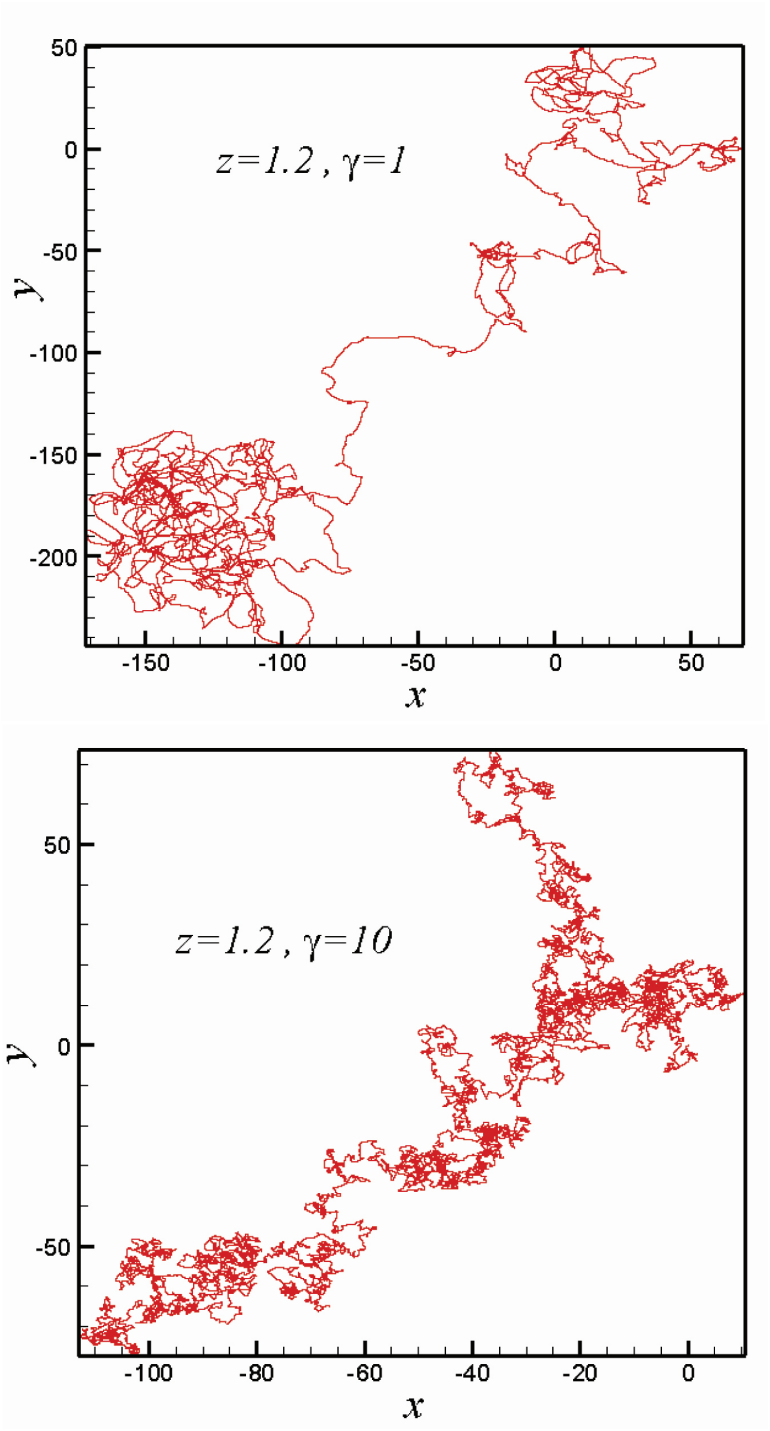

Figure 4.8: Two dimensional trajectories of He atom on the monolayer graphene at z=1.2 above the sheet with two different coefficients of friction according to the legends. Total time of simulations is 5 ns and the unit of length is a_1.

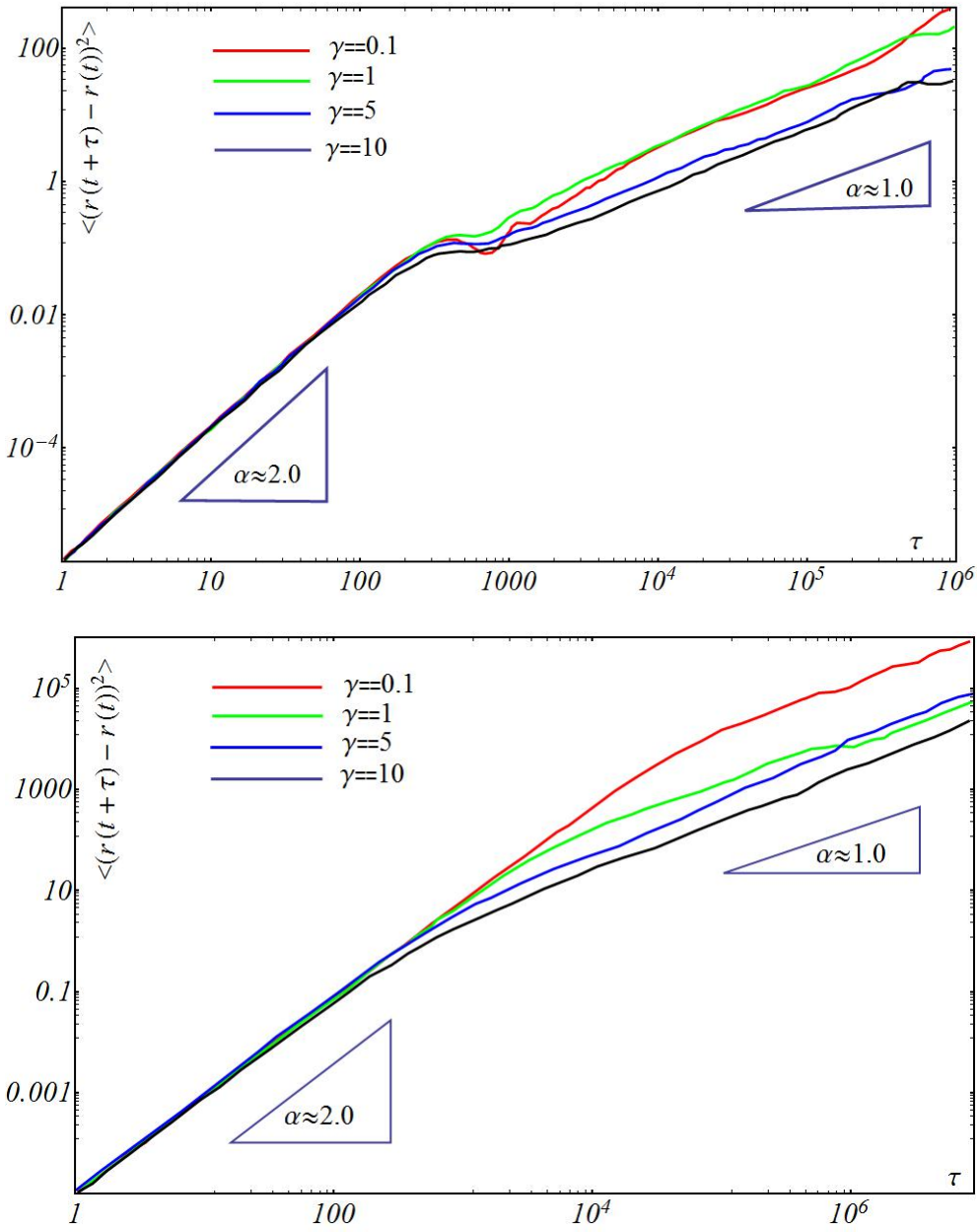

Figure 4.9: Mean square displacements for the motion of Xe atom (top) and He atom (bottom) for four different coefficients of friction.

Chapter 5

THERMOMECHANICAL PROPERTIES OF GRAPHENE

Since the discovery of graphene in 2004, which is an almost two dimensional crystalline material, its exceptional mechanical properties have been studied [57, 105, 43, 114, 115, 116]. Tensional strain in monolayer graphene affects its electronic structure. For example strains larger than 15% changes graphene's band structure and leads to the opening of an electronic gap [117]. In recent experiments the buckling strain of a graphene sheet that was positioned on top of a substrate was found to be six orders of magnitude larger (i.e. $0.5 - 0.6\%$) than for graphene suspended in air [115]. Furthermore, some experiments showed that a compressed rectangular monolayer of graphene on a plastic beam with size $30\times100\ \mu m^2$ is buckled at about 0.7% strain [118].

Elasticity theory for a thin continuum plate and the empirical interatomic potentials (EP) are two main theoretical approaches that have been used to study various mechanical properties measured in compressing and stretching experiments [114, 119, 120]. Continuum elasticity theory does not give the atomistic features of graphene while the EPs, such as the Brenner potential (REBO) [121, 122] and the LCBOPII potential [123], can properly account for the mechanical properties of graphene. Despite the several benefits of these EPs, some special atomistic features of graphene subjected to compressive or tensile strains could not be explained. The different energy contributions in these potentials are mixed. For example, in REBO all the many body effects are put in the bond order term and the different important energy contributions are not separable.

It still remains unclear how large are the contributions of the different energy terms in strained graphene. Using the recently introduced *valence force field*

(VFF) model by Perebeinos and Tersoff [11] we show how the contribution of the different energy modes in strained graphene can be separated and we calculate their dependence on the value of strain.

The bending modulus of graphene at zero temperature was estimated using several interatomic potentials, e.g., the first version of the Brenner potential [121] yields 0.83 eV, the second generation of the Brenner potential [122] estimated it to be 0.69 eV, adding the third nearest neighbors (the dihedral angle effect) in the Brenner potential enhances it to 1.4 eV [124], using the LCBOPII potential and continuum membrane theory the bending rigidity was found to be 0.82 eV [114, 123], Tersoff's VFF model estimated it to be 2.1 eV, and from ab-initio energy calculations it was found to be 1.5 eV [125] (note that 'bending rigidity' ('bending modulus') is used for a membrane stiffness (an atomistic sheet)). Despite these studies the temperature dependence of the bending modulus is poorly known. An increasing behavior versus temperature for the bending rigidity was found [114] by using Monte Carlo simulations with the LCBOPII potential and membrane theory concepts. In contrast, Liu *et al* [126] found a decreasing bending rigidity with temperature using the REBO. Here we show that the VFF model predicts a temperature independent bending modulus.

In this study we employ VFF and carry out standard Monte Carlo simulations in order to calculate and compare the different energy modes of a graphene sheet that is subject to axial strains. The total energy is found to be different for compressing and stretching when strains are applied larger than $|2|\%$. Two important terms, i.e. stretching and bending, vary differently depending on the way that one stretches or compresses the system. We find that out-of-plane and $\pi-\pi$ terms have much larger contributions in compression experiments when compared to stretching. Furthermore, we used this potential to calculate Young's modulus at room temperature from stretching-compressing simulations. We also calculate the molar heat capacity. Our Monte Carlo simulations show that the VFF potential yields a temperature independent bending modulus.

This chapter is organized as follows. Section 5.1 contains the essentials of the

VFF model for graphene. The simulation method for strained graphene will be presented in section 5.2. Different energy modes of strained graphene are studied in section 5.3. In section 5.4 the molar heat capacity for non-strained suspended graphene is calculated. Temperature effects on the bending modulus of graphene with periodic boundary condition are presented in section 5.5 and the scaling properties of graphene at finite temperature are investigated in section 5.6.

5.1 Elastic energy of graphene

There are two main classical approaches for the investigation of the elastic energy of graphene: 1) the continuum approach based on elasticity theory, and 2) the atomistic description using accurate interatomic potentials.

The total energy of a deformed membrane consists of two important terms: stretching and bending. For an almost flat and continuum membrane using Monge representation the surface area element dA can be approximated by a flat sheet area element in the x-y-plane, i.e. $dA \approx dxdy$ and the bending energy is written as $\frac{1}{2}\int dxdy\kappa(\nabla^2 h)^2$. Where κ is the bending rigidity and h is the out-of-plane deformation of the membrane at point (x, y). The stretching term for an isotropic continuum material in the linear regime includes two independent parameters: the shear modulus (μ) and the Lamé coefficient (λ) and is written as $\frac{1}{2}\int dxdy[2\mu u_{\alpha\beta}^2 + \lambda u_{\alpha\alpha}^2]$. Here $u_{\alpha\beta} = \frac{1}{2}[\partial_\alpha u_\beta + \partial_\beta u_\alpha + \partial_\alpha h \partial_\beta h]$ is the second rank symmetric tensor with $\alpha, \beta = 1, 2$ and $u_\alpha(x, y)$ is the α^{th} component of the displacement vector. Neglecting the last term in the strain tensor makes the stretching term linear and decouples the bending and stretching energy. Therefore, for an isotropic and continuum material for small deformations and with the assumption of a nearly flat membrane ($|\nabla h|^2 \ll 1$), the strain energy (U_T) can be written as [127]

$$U_T = \frac{1}{2}\int dxdy[\kappa(\nabla^2 h)^2 + 2\mu u_{\alpha\beta}^2 + \lambda u_{\alpha\alpha}^2]. \tag{5.1}$$

The integral is taken over the projected area of the membrane into the x-y-plane. For isotropic materials and in the linear approximation the mentioned parameters are related to the Young modulus (Y) and Poisson's ratio (ν) as $\mu = Y/(2(1+\nu))$ and $\lambda = 2\mu\nu/(1-2\nu)$. Equation (5.1) can be rewritten in terms of the Fourier components of h and yields the scaling properties of the sheet. Despite these benefits, this continuum model does not include self-avoidance (the natural condition of true physical systems) and does not show atomistic details of the membrane under different boundary conditions. All these deficiencies originate from the continuity assumption. Assuming graphene as a continuum plate limits the study to only bending and stretching modes.

Due to the hexagonal symmetry of the flat monolayer graphene lattice, it is elastically isotropic which implies that the the bending modulus is independent of the direction at least within the linear elastic regime [124]. However, the graphene monolayer can exhibits anisotropic behavior in the nonlinear regime where distortions are no longer infinitesimal. The larger stretches, the stronger anisotropy and non-linearity effects. Cadelano *et al* [128] found that monolayer graphene is isotropic in the linear regime, while it is anisotropic when nonlinear features are taken into account.

The recently introduced VFF model in Ref. [11] is expected to be able to describe both compression and stretching experiments by separating the contribution of the various energy modes. This model includes explicitly the various relevant energy terms which describe the change in the bond lengths, bond angles and torsional effects. The total energy density is written as

$$E_T = \frac{1}{NS_0}(E_{st} + E_{be} + E_{out} + E_{bo} + E_p + E_{co}), \tag{5.2}$$

where N is the number of atoms and $S_0 = \frac{3\sqrt{3}}{4}a_0^2$ is the surface area of the unit cell of the honeycomb lattice. In the following we will discuss the different terms in equation 5.2. Note that the energy reference is set to zero. Assuming

$a_0 = 1.42\,\mathring{A}$ as the unit of length, the '*stretching*' and '*bending*' (bending of the bond angle) terms are

$$E_{st} = \frac{1}{2}K_s \sum_{i,j} (\delta r_{ij})^2 \tag{5.3}$$

$$E_{be} = K_{be} \sum_{i,j<k} (\cos(\theta_{ijk}) - \cos(\theta_0))^2 \tag{5.4}$$

where $\delta r_{ij} = r_{ij} - 1$ and $\theta_0 = 2\pi/3$. In equations 5.3 and 5.4, r_{ij} is the bond length between atom 'i' and 'j', θ_{ijk} is the angle between the nearest neighbor atoms 'i', 'j' and 'k' and θ_0 is the equilibrium angle between three nearest neighbor atoms. E_{st} is the two-body stretching term responsible for bond stretching. E_{be} is the bending energy due to the bond angles. Here, all bond angles will be considered. The above two terms results in a quasi-harmonic model [123]. Later, we will find that these two terms become constant as function of strain when beyond the buckling point in a compression experiment.

The stiffness against '*out-of-plane*' vibration is provided by

$$E_{out} = K_{out} \sum_{i,j<k<l} \left(\frac{3\overrightarrow{r_{ij}} \cdot \overrightarrow{r_{ik}} \times \overrightarrow{r_{il}}}{r_{ij}r_{ik} + r_{ij}r_{il} + r_{ik}r_{il}}\right)^2, \tag{5.5}$$

where the summation is taken over the first neighbors of atoms 'i' and taking care of not double counting. In equation 5.5, $\overrightarrow{r_{ij}}$ is the distance vector between atom 'i' and 'j'. Hence there are three different terms for each atom. Correlations between bond lengths are provided by the '*bond order*' term

$$E_{bo} = K_{bo} \sum_{i,j<k} \delta r_{ij} \delta r_{ik}, \tag{5.6}$$

where for each bond length with central atom 'i' three different terms are considered.

The misalignment of the neighboring π orbital is given by the '$\pi - \pi$' term

$$E_p = \frac{1}{2}K_p \sum_{i,j} |\overrightarrow{\pi_i} \times \overrightarrow{\pi_j}|^2, \tag{5.7}$$

Table 5.1: Parameters of the energy model are taken from Ref. [11]. The unit is eV.

K_s	K_{be}	K_{out}	K_{bo}	K_p	K_{cor}
37.04	4.087	1.313	4.004	0.016102	4.581

where

$$\overrightarrow{\pi_i} = 3\frac{\overrightarrow{n_{ijk}} + \overrightarrow{n_{ikl}} + \overrightarrow{n_{ilj}}}{r_{ij}r_{ik} + r_{ij}r_{il} + r_{ik}r_{il}}. \tag{5.8}$$

$\overrightarrow{n_{ijk}} = \overrightarrow{r_{ij}} \times \overrightarrow{r_{ik}}$ is a vector normal to the plane passing through the vectors $\overrightarrow{r_{ij}}$ and $\overrightarrow{r_{ik}}$. This kind of interaction plays an important role in the interlayer interaction in graphitic structures. Note that the simple two body interaction gives only 2% of the local density of state (LDA) result for the energy difference between AA and AB stacked graphite [129].

The last term takes into account the coupling between bond stretching and bond angle bending (bond length-bond angle cross coupling), i.e. the *'correlation'* term

$$E_{cor} = K_{cor} \sum_{i,j<k} \delta r_{ij}(\cos(\theta_{ijk}) - \cos(\theta_0)). \tag{5.9}$$

The coefficients in the above equations (K_s, K_{be} and so on) were recently parameterized by Perebeinos and Tersoff [11] such that the phonon dispersion of graphene was accurately described. These parameters are listed in Table 5.1.

5.2 Simulation method: strained graphene

In order to compress (stretch) graphene nanoribbons, we have carried out several standard Monte Carlo simulations [114] of a suspended graphene sheet at finite temperature. Equation (5.2) is used to calculate the total energy of the system. Our sample is a rectangular graphene sheet with $l_x \times l_y$ dimensions in x- and y-directions, respectively, containing N_0=1600 atoms. The sheet is strained along the armchair or the zig-zag direction. Strain is always applied

Table 5.2: Young's modulus of graphene in units of N/m.

Experimental	340±50	Ref. [57]
Classical (T=300 K)	350±3.15 355±21 384	Present[§] Ref. [119][†] Ref. [130][‡]
Ab-initio (T=0 K)	345±6.9 336 352.54 351.75 322	Ref. [125] Ref. [131] Ref. [132] Ref. [133] Ref. [97]
Tight-Binding	312	Ref. [128]

[§] VFF model [11], [†] LCBOPII potential, [‡] Tersoff-Brenner potential.

along x. When graphene is strained along the armchair direction we named it *armchair graphene* -AC- (l_x=85.2 Å, l_y=49.19 Å) and strained graphene along zig-zag direction is named *zig-zag graphene*-ZZ- (l_x=98.38 Å, l_y=42.6 Å). Periodic boundary conditions are applied along the lateral direction i.e. zigzag direction in AC graphene and along the armchair direction for ZZ graphene. Our simulation starts with a flat sheet, and we allow then the system to thermally equilibrate such that the total energy no longer changes. Temperature is typically taken T=300 K, except when otherwise indicated.

Figure 5.1(a) shows a snapshot of the relaxed unstrained ZZ graphene at T=300 K (note that the supported ends are fixed). We found that the graphene sheet is corrugated after relaxation which are the intrinsic thermal ripples in graphene. Thus the used VFF is able to display true structural properties. These ripples are vital in order to make suspended graphene stable and are, therefore, crucial for the stability of a flat 2D crystal at finite temperature [114].

To simulate a suspended sheet we fixed two atomic rows at both longitudinal ends. These boundary atoms are not included in the summations when calculat-

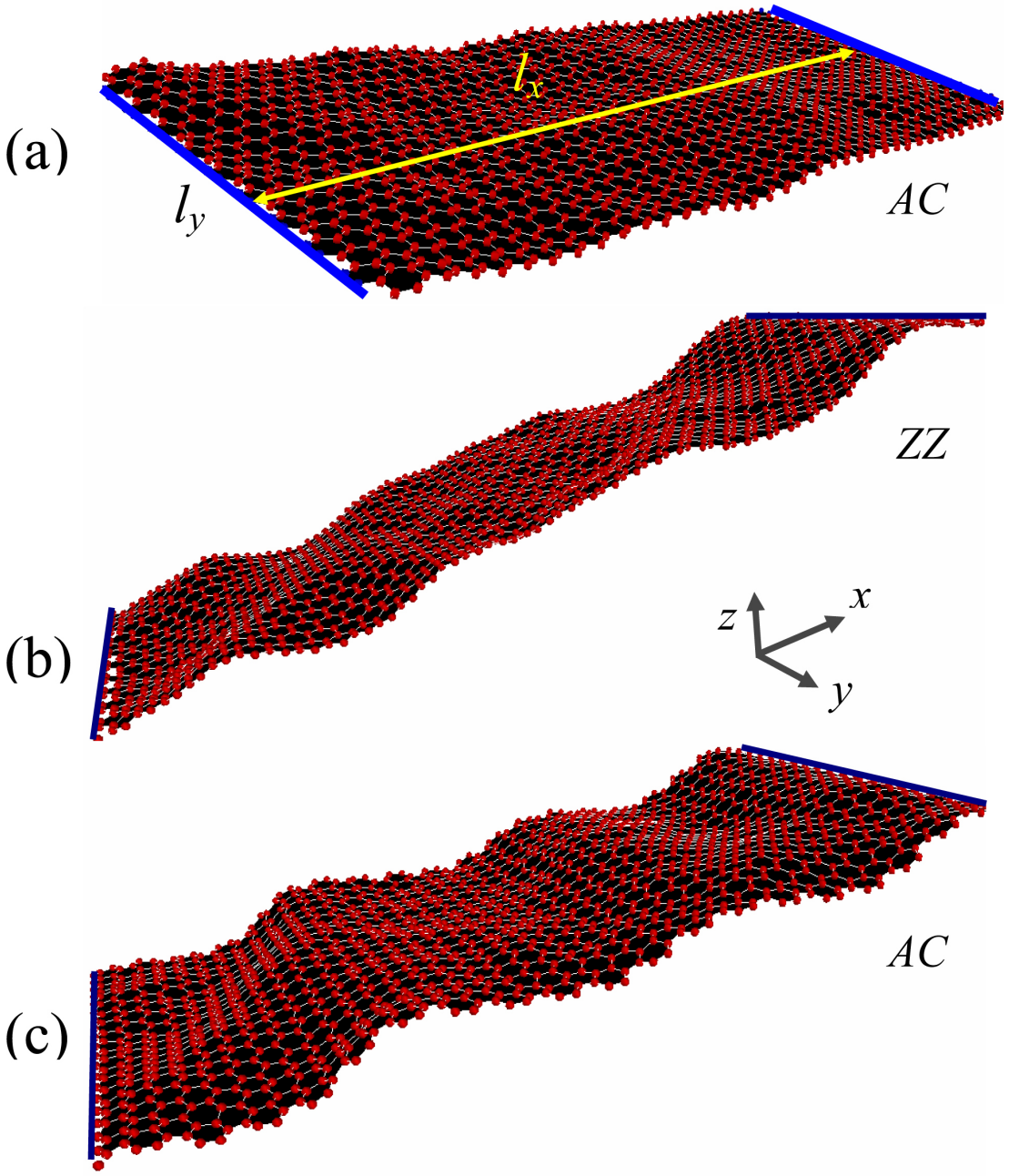

Figure 5.1: The snapshot of a suspended graphene sheet at T=300 K using the valence force model (Equation 5.2). Blue lines indicate the position of fixed atoms in $x-y$ plane. (a) Unstrained, (b) compressed ZZ graphene, and (c) compressed AC graphene.

ing the different energy contributions (in equations 5.2-5.9), i.e. $N = N_0 - 40$. We compress/stretch the system with a slow rate, i.e. in every million Monte Carlo steps the longitudinal ends are reduced/elongated with about δ =0.02 Å such that the system stays in thermal equilibrium. After obtaining the total desired strain ε, we wait for an extra 4 million steps during which the system can relax. For example, a strain (applied in x-direction) of $\varepsilon = 1.2\%$ is achieved after 29×10^6 Monte Carlo steps.

5.3 Different energy modes for strained graphene

Figures 5.1(b) and (c) show two snapshots of compressed ZZ and AC graphene, respectively when ε=-2%. It is interesting that the rippled structure is different in the two cases. This is due to the different out-of-plane and $\pi - \pi$ interaction terms around and beyond the buckling transition points, i.e. $\varepsilon \lesssim -2.5\%$.

The variation of height, $\widetilde{\Delta h} = \sqrt{< h^2 > - < h >^2}$, in figure 5.1(a) after 10 million MC steps fluctuates around 0.2 Å which is comparable with those found when using REBO [134]. In figures 5.1(b,c) for compressed nanoribbons of about ε = -2.0 % $\widetilde{\Delta h}$ is 0.5 Å after 54 million MC steps. The larger compressive strain yields a larger height variance.

Figure 5.2 shows the variation of the total energy (equation (5.2)) with applied strain at T=300 K. The vertical dashed line separates compressive (left) and tensile strain (right). Square (circular) symbols refer to AC (ZZ) graphene. Notice that AC and ZZ strained graphene result in the same energy, although their ripples structure (see figures 5.1(b,c)) can be rather different. Note that the energy curve is no longer symmetric around $\varepsilon = 0$ beyond the colored rectangle where $|\varepsilon| \gtrsim 0.02$. Inside this region the deformation is symmetric and the harmonic approximation to the total energy works well as shown by the full black (parabolic) curve in figure 5.2. The solid curve is a quadratic fit according to $E_T = E_0 + \frac{1}{2}Y\varepsilon^2$ for only positive strains, where the fitting parameter Y is Young's modulus and E_0 is the energy of the graphene sheet in the absence of

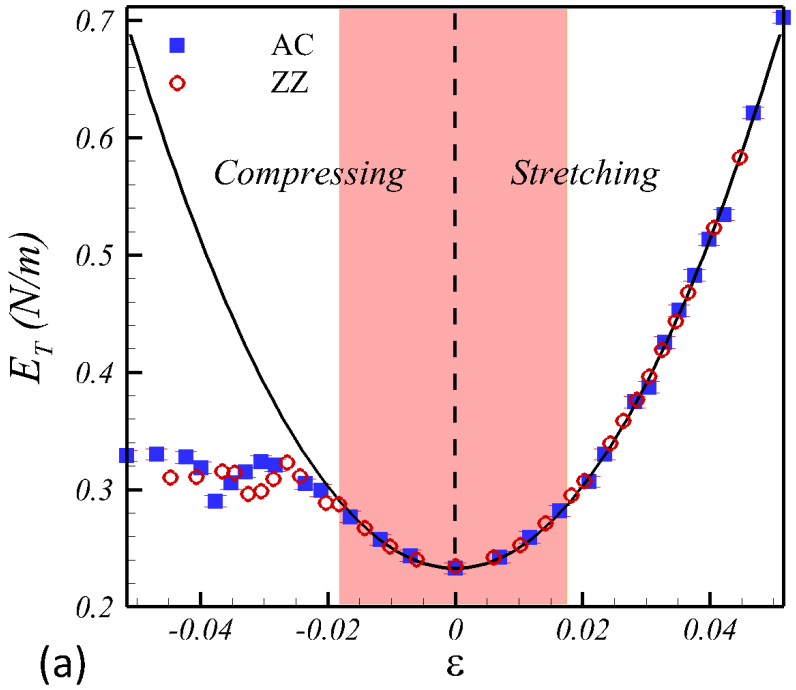

Figure 5.2: Total energy of a graphene sheet subjected to stretching and compression for AC and ZZ.

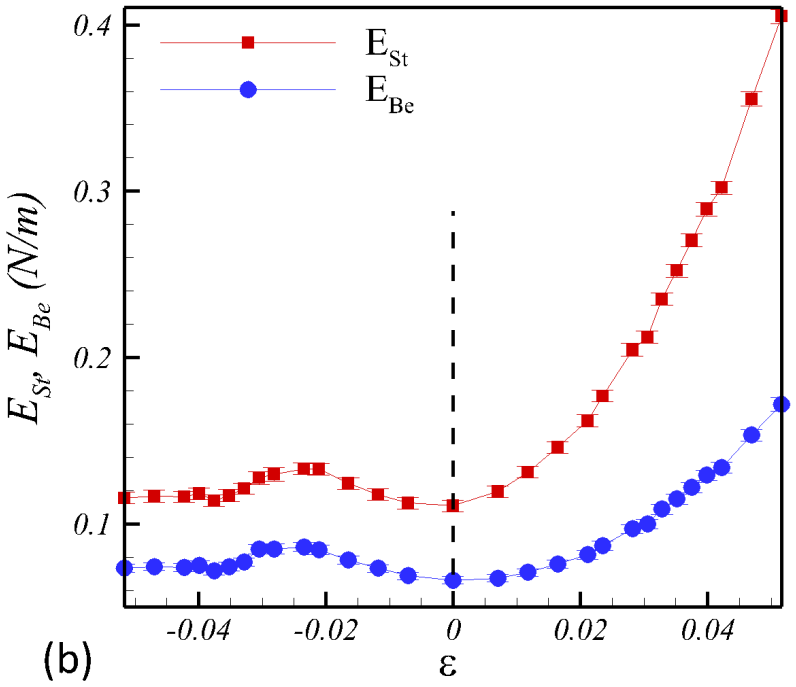

Figure 5.3: Contribution of the bending (Eq. 5.4) and the stretching (Eq. 5.3) terms of the total energy for AC.

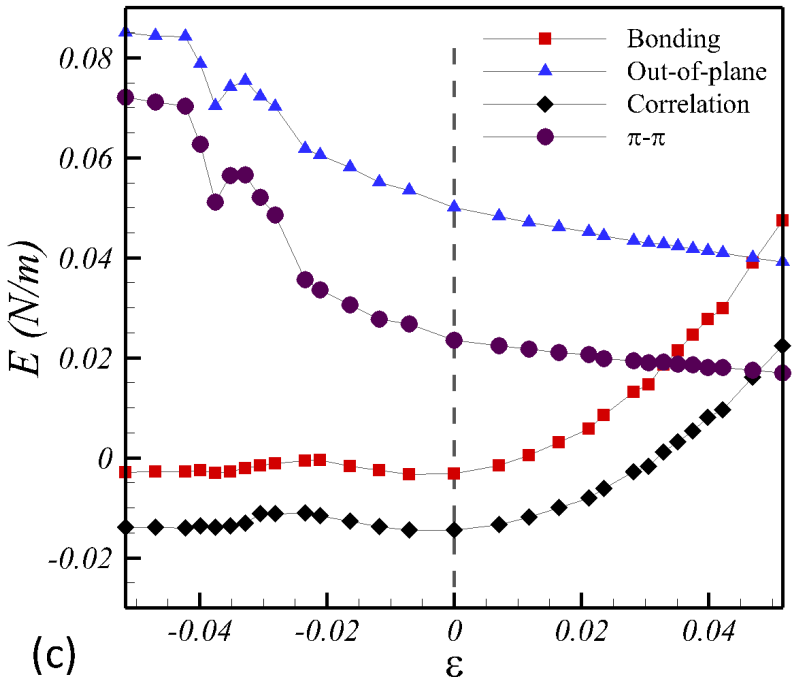

Figure 5.4: Contribution of the other remaining terms given by Eqs. 5.5-5.9 for AC.

strain. We found E_0=0.232±0.002 N/m and Y=350.42±3.15 N/m for room temperature. The calculated error bars are derived from the fitting procedure of our numerical data. The best fit yielded the smallest deviation from the harmonic behavior. Our result for the room temperature Young's modulus is close to the experimental value (340±50 N/m) and is within the ab-initio results (335-353 N/m) and is in agreement with those obtained from other classical force fields such as (LCBOPII [119] and Tersoff-Brenner [130]) and Tight-Binding [128], see 5.2. Note that Perebeinos and Tersoff estimated Y at zero temperature and found 1.024 N/m^2 (343.04 N/m) [11]. Here we calculated Y at room temperature via stretching-compression simulations. Different force fields are parameterized such that they describe a set of chosen experimental data of particular experimental effects. For example, the VFF model can not be used to study hydrogenation, melting and defect formation in either graphene or carbon nanotubes sheets, while the REBO has been set-up such that it can be used in those cases. The property

that the energy can be separated into different energy modes and the simplicity of coding the VFF potential are two important advantages of this model.

Notice that the total energy for AC (square symbols in figure 5.2) and ZZ (circular symbols in figure 5.2) graphene are almost the same which is in agreement with the results of Ref. [128]. Graphene acts isotropically in the linear elastic limit. Beyond the harmonic regime there is a small local maximum in the energy for compression which is related to the buckling of graphene. Notice that in this regime there are small differences between ZZ and AC sheets. The buckling threshold is about $\varepsilon_b \simeq -2.5\%$. The buckling strains is smaller than those found by using REBO [120], i.e. -0.86%. Notice that both the boundary conditions and the employed interatomic potentials are responsible for the difference in the buckling thresholds. The main difference is due to the different potential. The VFF model is not a bond-order potential (REBO). As we mentioned in the introduction the bending modulus predicted by REBO is about 0.69-0.83 eV which is smaller than the one predicted by the VFF model (2.1 eV). Therefore, we expect a larger buckling transition using REBO and a smaller one using VFF model (considering the negative sign for compressive strains). Another important reason for the different result is the calculations method. Here we used Monte Carlo (time is meaningless) and in Ref.[120] we used Molecular dynamics simulations.

Figure 5.3 shows the contribution of the two important energy terms, i.e. stretching and bending as given by equation 5.3 and equation 5.4, respectively, for strained AC graphene. Notice that the stretching energy is larger than the bending and that the rate of increase for stretching is different. In the compression part (i.e the region to the left of the vertical dashed line), after the buckling points these energies are almost constant. Thus increasing compression beyond the buckling point does not change the bending and stretching energies. Figure 5.5 shows the contribution of the different energy terms (scaled by E_T) for three values of the strain for both AC and ZZ graphene (e.g., the first set of bars to the left refer to $100 \times E_{st}/E_T$ for each particular strain shown in the legends). From figure 5.5, we conclude that the contribution of the energy terms (equation 5.4

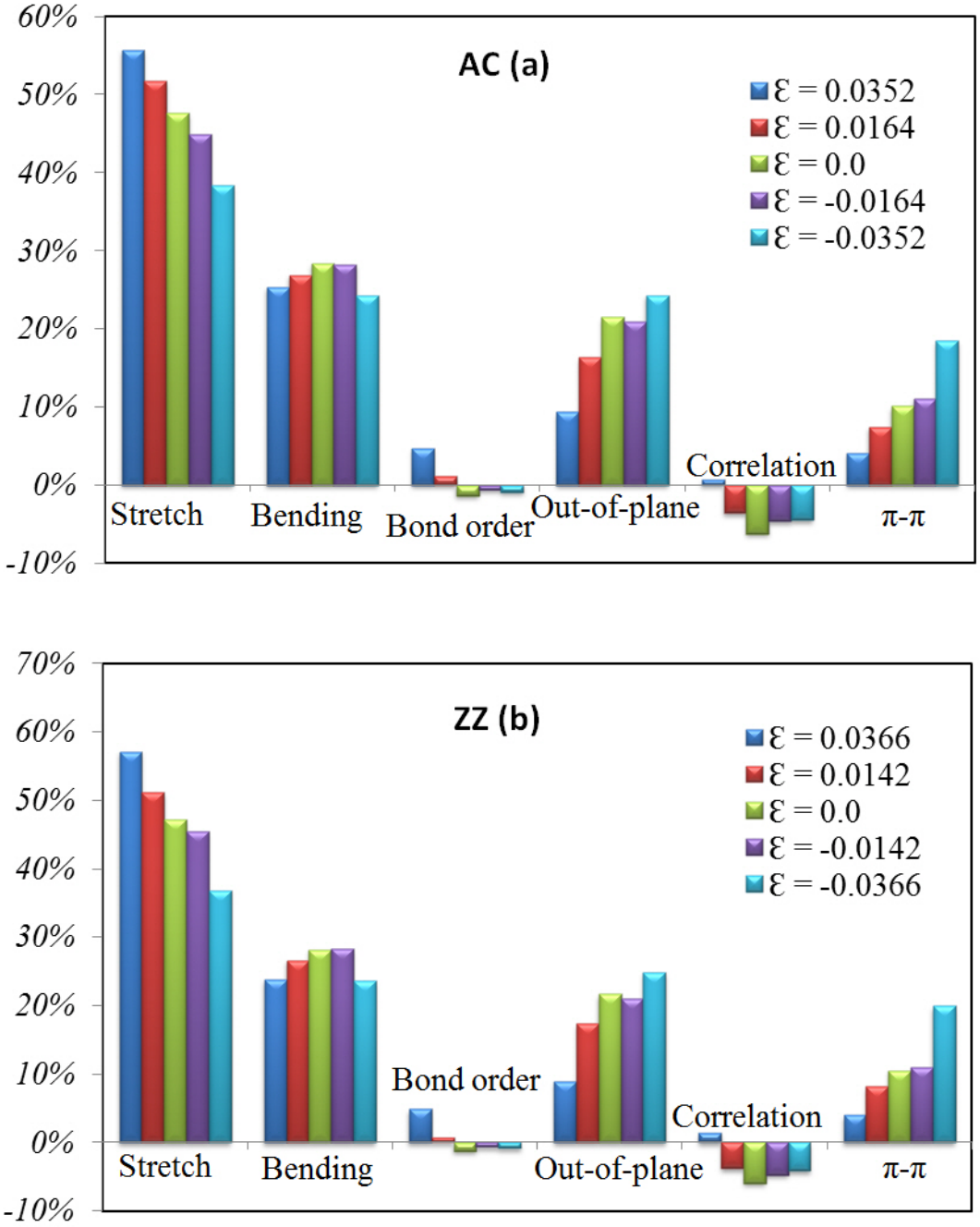

Figure 5.5: Contribution of the different energy terms to the total energy for three typical values of the strain in AC (Top) and ZZ (Bottom) graphene.

and equation 5.7) which are not determinable in the continuum elasticity energy approach (equation (5.1)) are substantial and should be retained when describing strained graphene at the atomistic scales

Figure 5.4 shows the variation of the other terms in the energy, equations 5.5-5.9), with strain. The energy for π-π repulsion and out-of-plane increase (decrease) with compression (stretching) and they behave opposite to the other terms. In compression experiments the sheets become strongly corrugated and neighbor π orbitals become more misaligned. In other words the normal to the adjacent surfaces, - $\overrightarrow{n_{ijk}}$- and -$\overrightarrow{n_{ijl}}$- become more misaligned and results in an increase of the total energy. Notice also that the bond order term is smaller and negative in the compression part with respect to the stretching part. The correlation between the bond lengths is always negative for the compression part. We found that the relative contribution of the different energy modes for stretching and compression of AC and ZZ graphene are almost the same, compare figure 5.5(a) and figure 5.5(b). However as we see from figures 5.1(b,c) the structure of the ripples depends on the direction of the applied strain. In the case of AC the ripples are regular (sinusoidal shape) while they exhibit an irregular pattern in ZZ graphene. Note that the buckling in plates is generally known to depend on the plate geometric parameters [135, 120]. Notice that, the dependence of the ripple structure of the graphene sheets on the sheet geometry has been demonstrated experimentally in Ref. [115].

5.4 Molar heat capacity

Next, we simulated graphene at different temperatures. Figure 5.6 shows the temperature dependence on the average total energy and of the six energy terms for $\varepsilon = 0$. Notice that all energy terms vary linearly with T. The quantity $C_V = N_A S_0 \frac{d\langle E_T \rangle}{dT}$ gives the potential energy contribution to the molar heat capacity of the system at constant volume, where N_A is Avogadro's constant. We first relaxed the volume of the system by performing a constant pressure-temperature (NPT)

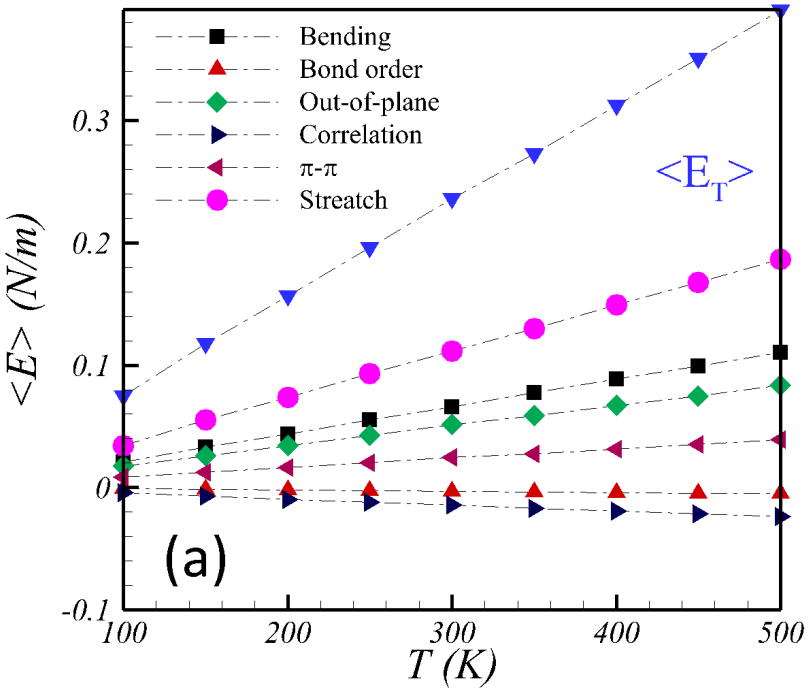

Figure 5.6: Temperature dependence of the various energy modes of a suspended graphene sheet which is suspended along arm-chair direction.

Monte Carlo simulation (which removes possible boundary strains). Then we fixed the boundaries to the found relaxed size and allowed for additional thermal relaxation (i.e. constant volume-temperature Monte Carlo simulation or NVT). During this new thermal relaxation no strain is applied $\varepsilon = 0$, thus, the calculated heat capacity corresponds to constant volume molar heat capacity. Surprisingly, we found that $C_V = 12.33\,\mathrm{J\,mol^{-1}\,K^{-1}}$ which is almost half of the Dulong-Petit value, i.e. $3\Re$=24.94 $\mathrm{J\,mol^{-1}\,K^{-1}}$. Notice that $\langle E_T \rangle$ is the average of the potential energy of graphene which is taken over 4 million Monte Carlo steps. Assuming that the average of the kinetic term equals the average potential energy ($\langle E_T \rangle$) according to the equipartition theorem (in the harmonic regime), we can write the total energy $\langle E \rangle = \langle E_T \rangle + \langle K \rangle = 2\langle E_T \rangle$ and then the total heat capacity is found to be $24.66 \pm 0.10\,\mathrm{J\,mol^{-1}\,K^{-1}}$. The obtained result is close to our previous result obtained using REBO, i.e. $24.98 \pm 0.14\,\mathrm{J\,mol^{-1}\,K^{-1}}$ [136]. In Ref. [119] the heat capacity at 300 K was found to be $24.2\,\mathrm{J\,mol^{-1}\,K^{-1}}$. We have performed many

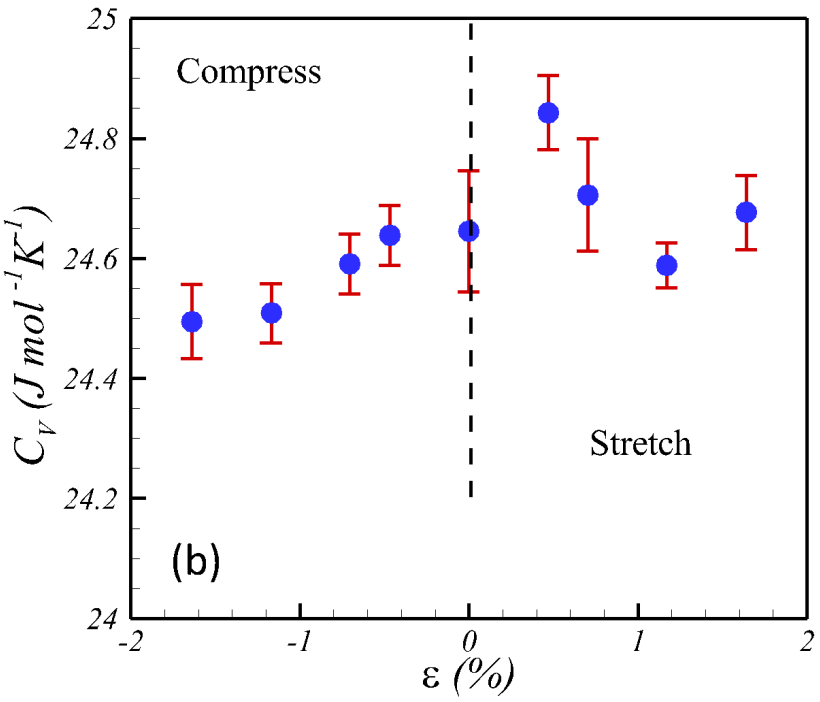

Figure 5.7: Variation of molar heat capacity at constant volume for graphene subjected to compressive and tensile strains.

simulations at different temperatures for strained graphene and found always a linear $\langle E_T \rangle - T$ curves. Figure 5.7 shows the variation of C_V versus strain. It is interesting to note that C_V is slightly lower ($\sim 1.0\%$) in compressed graphene as compared to stretched graphene.

Furthermore, we performed several simulations using the same sample employing the AIREBO potential within LAMMPS software. It is interesting to know that AIREBO gives (in the range of 10 K-1000 K) C_V=24.92 J mol^{-1} K^{-1} which was found to be independent of temperature. Therefore, the VFF model, REBO and AIREBO predicts temperature independent heat capacity.

On the other hand, we found that the VFF model, REBO and AIREBO, give a linear increase in the carbon-carbon bond length (a) with temperature. The resulting bond length thermal expansion coefficients for the VFF model, REBO and AIREBO are $\alpha = \frac{1}{a_0}\frac{da}{dT} = (5.0 \pm 0.07) \times 10^{-6} K^{-1}$, $(5.0 \pm 0.03) \times 10^{-6} K^{-1}$ and $(7.0 \pm 0.04) \times 10^{-6} K^{-1}$ respectively. The Gruneisen parameter is defined

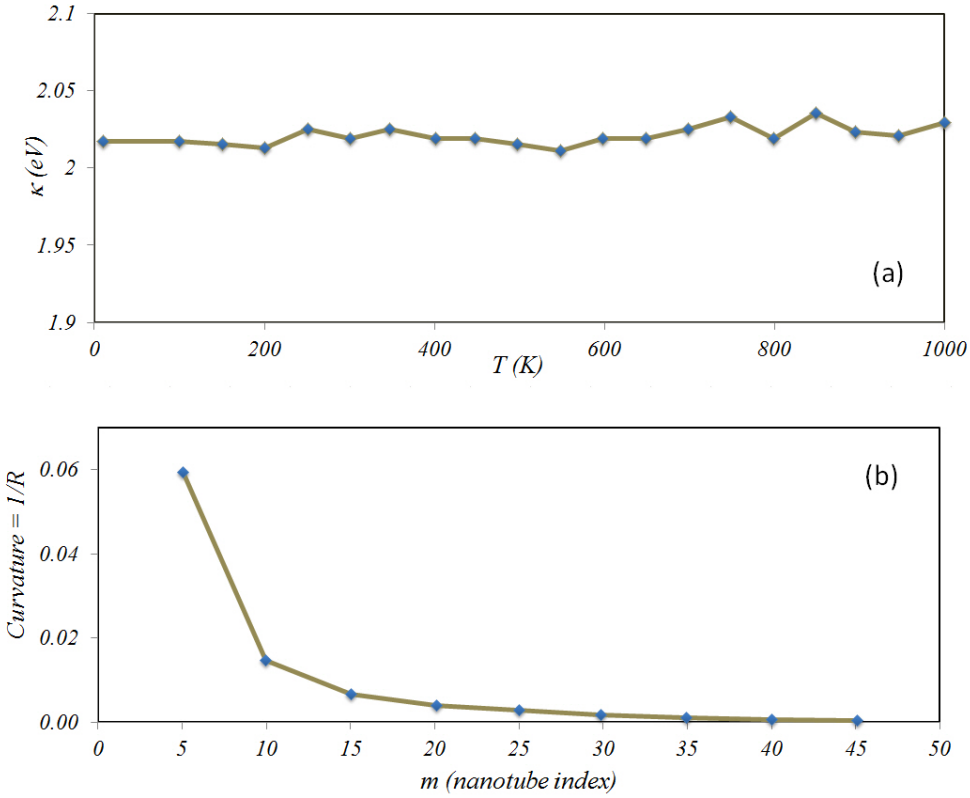

Figure 5.8: Temperature dependence of the bending modulus of graphene (a) and variation of the nanotube curvature versus nanotube index, i.e m.

as $\gamma = \frac{\alpha B}{C_V \rho}$ where B is the two dimensional bulk modulus for graphene, i.e $B = 12.7$ eVÅ^{-2} [119], and ρ is the mass density of graphene, i.e. $\rho = 12.0/S_0 = 7.6 \times 10^{-4}$g m^{-2}. Using our result for C_V and α gives $\gamma = 0.64$ which is better estimation for the Grüneisen parameter than the one found in Ref. [11], i.e. -0.2, and is closer to the experimental result, i.e. 2.0 [137].

5.5 Temperature effect of the bending modulus

A common method for calculating the bending modulus of graphene is by performing several simulations as function of the radius (R) of the curved tubes and extrapolating the results to $R \to \infty$ (see figure 5.8(b)). Hence, one can calculate the elastic energy of carbon nanotubes as a function of the inverse square of the radius, $E = \frac{1}{2}\kappa R^{-2}$. The coefficient κ in the elastic energy gives the bending modulus of graphene. In order to study the effect of temperature on the bending

modulus of graphene we have carried out several NPT Monte Carlo simulations (constant pressure with periodic boundary condition) at different temperatures. For each particular temperature we have 8 different tubes. In this part, our systems are different armchair carbon nanotubes with radius $R = 3\,m^2\,a_0/2\pi$ and initial length 10 nm. We used eight armchair carbon nanotubes with index (m,m) for m= 5, 10, 15, 20, 25, 30, 35, 40. For each particular nanotube with index m, we carried out several NPT Monte Carlo simulations with periodic boundary condition along the nanotube axis and varying temperatures in the range 10 to 1000 K. Calculating E_T by using equation 5.2 for all nanotubes at temperature T, we fitted $\frac{1}{2}\kappa R^{-2}$ to the data and found the bending modulus (stiffness), κ, at T. From figure 5.8(a) we notice that κ is practically temperature independent and is about 2.02 eV. Thus the present VFF model results in a temperature independent bending modulus. Using membrane theory to calculate the bending rigidity of graphene shows that different potentials lead to conflicting temperature dependence for the bending rigidity; e.g., LCBOPII [114] yields an increase of the bending rigidity with temperature while REBO predicts a decreasing dependence [126].

5.6 Scaling properties

In the harmonic regime the power spectrum of the graphene solid membrane can be obtained by calculating $< |h_q|^2 >$ where h_q is the Fourier transform of the height of the atoms (h) and q is the norm of the wave vector $\overrightarrow{q}$ ($= (q_x, q_y) = 2\pi(\frac{n_x}{l_x}, \frac{n_y}{l_y})$) with integers n_x and n_y where l_x and l_y are the longitudinal and lateral size of the graphene sample. It is important to note that in this section we simulated a graphene sheet with initial size $l_x = 230.04\,\mathring{A}$ and $l_y = 221.35\,\mathring{A}$ (N=19440) using standard NPT Monte Carlo simulations with periodic boundary conditions in both directions (the method is similar to that reported in Refs. [4,10]). We estimated the spectral modes h_q by fitting $|h_q|^2$ to a q^α function, from which we extract the power law α. Figure 5.9 shows the variation

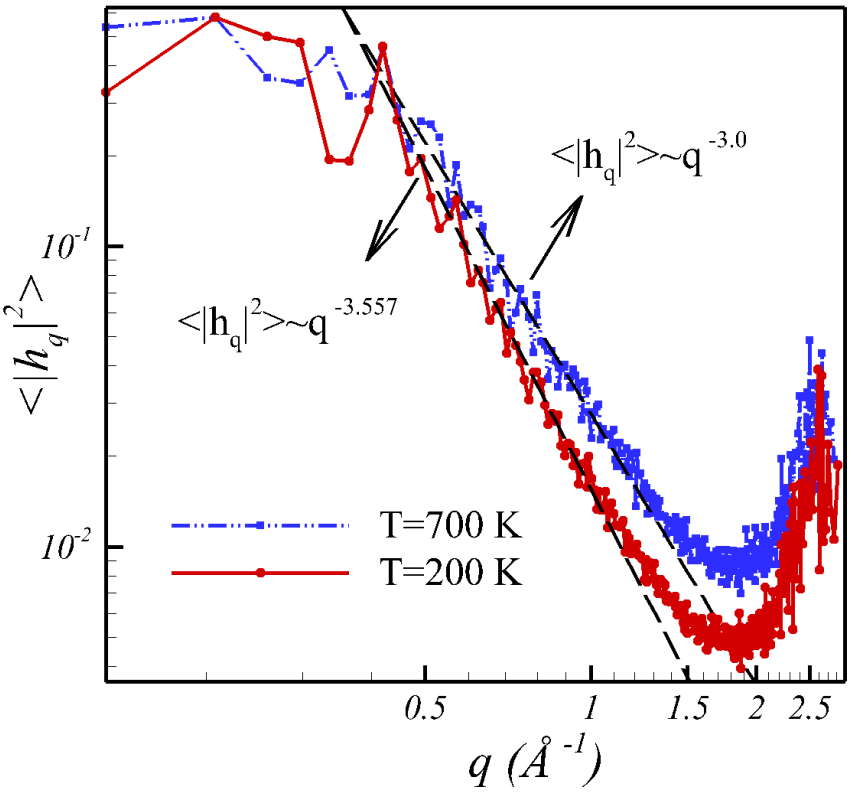

Figure 5.9: The absolute value of the square of the Fourier transform of atomic heights of C-atoms ($|h_q|^2$) versus the absolute value of the wave vectors of the graphene lattice.

of $|h_q|^2$ (averaged over 500 Monte Carlo realizations where 5 neighboring points were accumulated and averaged to a single point in order to make the curves smoother) versus q for graphene at two temperatures 200 K and 700 K. The dashed lines are power law fits. Notice that $\alpha \neq -4$ which clearly indicates that anharmonic effects are present in the used VFF potential. Moreover we see that α decreases with decreasing temperature (α =-3.0 for T=700 K and α =-3.557 for T=200 K) which hints that a more harmonic behavior is found at low temperature when using the VFF potential. The latter temperature dependence is in agreement with the REBO predictions [134]. Notice that the REBO is a bond-order interatomic potential. The peaks in Figure 5.9 are related to first Bragg-peak, $4\pi/3a_0 = 2.94\mathring{A}$ due to the discreteness of the graphene lattice. The modulation amplitude in Figure 5.9 for T=200 K is about 0.5Å and for T=700 K is about 0.7Å which are temperature and size dependent quantities, the larger the size the larger the amplitudes (here graphene has dimension 221×230 Å^2).

Chapter 6

CONCLUSION

In our first work that published in Computational Materials Science 49(4):839 (2010), the stochastic motion of noble gases in a two dimensional periodic potentials (2DPP) produced by a graphene membrane was studied. We calculated the depth of the potential well of the interaction between noble gases and the graphene sheet. The Langevin equation was solved with velocity Verlet algorithm to find out the effects of the binding energy, damping factor and the equilibrium distance to the motion of noble gases on the graphene sheet.

2DPP produced by the monolayer, bilayer and triple-layer of graphene were studied. We showed that increasing the number of graphene layers changes infinitesimally the pairwise interaction between noble gases and the graphene sheet. The binding energies were calculated in the range of meV and the equilibrium distances were found to be less than $2^{1/6}\sigma$. The effects of the coefficient of friction and the type of the elements deposited over the graphene, on the trajectories of the motion of noble gases on the graphene were investigated. We showed that the Xe atom with smaller binding energy is trapped in the potential well at high friction coefficients while the He atom with larger binding energy can freely diffuse.

In our second project that published in Journal of Physics Condensed Matter 24(17): 175303 (2012), with using the valence force field model of Perebeinos and Tersoff, different energy modes of suspended graphene subjected to tensile or compressive strain were studied. By carrying out Monte Carlo simulations some exciting results were found. The only for small strains ($|\varepsilon| \lessapprox 0.02$) the total energy is symmetrical in the strain, while it behaves completely different beyond this threshold. The important energy contributions in stretching exper-

iments are stretching, angle bending, out-of-plane term and the term provides repulsion against $\pi - \pi$ misalignment. In compressing experiments the two latter terms increase rapidly and beyond the buckling transition stretching and bending energies are found to be constant. From stretching-compressing simulations we calculated the Young modulus at room temperature 350 ± 3.15 N/m, which is in good agreement with experimental results (340 ± 50 N/m) and with ab-initio results 322-353 N/m. Molar heat capacity is estimated to be $24.64\,\mathrm{J\,mol^{-1}\,K^{-1}}$ which is comparable with the Dulong-Petit value, i.e. $24.94\,\mathrm{J\,mol^{-1}\,K^{-1}}$ and is almost independent of the strain. Non-linear scaling properties were obtained from height-height correlations at finite temperature. The used valence force field model results in a temperature independent bending modulus for graphene.

In this study, we showed that the recently proposed valence force field model (VFF) [11] for graphene enables to compare the contribution of the different energy terms when straining graphene. In a stretching experiment the main energy contributions are due to stretching and bending terms while for compressive strains also other terms such as out-of-plane and $\pi - \pi$ interaction terms play an important role. We found that using such a classical approach gives accurate values for the Young's modulus at room temperature which are found to be as accurate as those using ab-initio methods. The calculated Young's modulus is close to the experimental result. The total energy is quadratic in ε for strains smaller than $|2\%|$. The current VFF model predicts a temperature independence bending modulus. The temperature dependence of the total strain energy yields an acceptable value for the molar heat capacity of graphene which is almost independent of the applied strain. The Grüneisen parameter is found to be positive and about 0.64. These results can confirm that the present VFF model is an accurate force fields for studying the thermo-mechanical properties of graphene.

REFRENCES

[1] Swapan K. Pati, Toshiaki Enoki, and C. N. R. Rao. *Graphene and its fascinating attributes*. World Scientific, Singapore ;, Hackensack, N.J, 2011.

[2] Jinghong Fan. *Multiscale analysis of deformation and failure of materials*. Wiley, Chichester, West Sussex ;, Hoboken, NJ, 2011.

[3] Sergey Mikhailov. *Physics and applications of graphene*. InTech, Rijeka, 1. publ. edition, 2011.

[4] Sidney Yip and Tomas de La Diaz Rubia. *Scientific modeling and simulations*. Springer, Berlin, 2009.

[5] M. P. Allen and D. J. Tildesley. *Computer simulation of liquids*. Clarendon Press and Oxford University Press, Oxford [England], New York, 1989, c1987.

[6] D. Frenkel and B. Smit. *Understanding Molecular Simulation*. Academic Press, San Diego, 1996.

[7] M. P. Allen and D. J. Tildesley. *Computer simulation in chemical physics*. Kluwer Academic Publishers, Dordrecht ;, Boston, 1993.

[8] Andrew R. Leach. *Molecular modelling: Principles and applications*. Pearson Prentice Hall, Harlow [u.a.], 2 edition, 2001.

[9] Tamar Schlick. *Molecular modeling and simulation: An interdisciplinary guide*. Springer, New York, [repr. with corrections] edition, 2006.

[10] Giovanni Ciccotti and W. G. Hoover. *Molecular-dynamics simulation of statistical-mechanical systems: Proceedings of the International School of Physics "Enrico Fermi" : course XCVII, Varenna on Lake Como, Villa Monastero, 23 July-2 August 1985*. North-Holland, Amsterdam ;, Oxford, 1986.

[11] Vasili Perebeinos and J. Tersoff. Valence force model for phonons in graphene and carbon nanotubes. *Physical Review B*, 79(24), 2009.

[12] Hugh O. Pierson. *Handbook of carbon, graphite, diamond, and fullerenes: Properties, processing, and applications*. Noyes Publications, Park Ridge and N.J, 2001.

[13] H. W. Kroto and D. R. M. Walton, editors. *The Fullerenes*. Cambridge University Press, Cambridge, 1993.

[14] B. T. Kelly. *Physics of graphite*. Applied Science, London and and Englewood and N.J, 1981.

[15] D. Chung. Review graphite. *Journal of Materials Science*, 37:1475–1489, 2002.

[16] C. S. G. Cousins. Formal elasticity of four carbon allotropes: I. the inner elastic constants, internal strain tensors, and zone-centre optic mode frequencies and their pressure dependences. *Journal of Physics: Condensed Matter*, 14(20):5091–5113, 2002.

[17] L. Samuelson, Inder P. Batra, and C. Roetti. A comparison of electronic properties of various modifications of graphite. *Solid State Communications*, 33(7):817–820, 1980.

[18] S. Flandrois and B. Simon. Carbon materials for lithium-ion rechargeable batteries. *Carbon*, 37(2):165–180, 1999.

[19] Guozhong Cao. *Nanostructures & nanomaterials: Synthesis, properties & applications*. Imperial College Press, London, 2004.

[20] S.C Graham, K. Pichler, R.H Friend, W.J Romanow, J.P McCauley, N. Coustel, J.E Fischer, and A.B Smith. Photoluminescence in solid films of c60. *Synthetic Metals*, 50(1-3):531–535, 1992.

[21] H. W. Kroto, A. W. Allaf, and S. P. Balm. C60: Buckminsterfullerene. *Chemical Reviews*, 91(6):1213–1235, 1991.

[22] H. W. Kroto and K. McKay. The formation of quasi-icosahedral spiral shell carbon particles. *Nature*, 331(6154):328–331, 1988.

[23] Hongjie Dai. Carbon nanotubes: opportunities and challenges. *Surface Science*, 500(1-3):218–241, 2002.

[24] X. Zhao, Y. Liu, S. Inoue, T. Suzuki, R. Jones, and Y. Ando. Smallest carbon nanotube is 3å in diameter. *Physical Review Letters*, 92(12), 2004.

[25] Qian Wen, Rufan Zhang, Weizhong Qian, Yuran Wang, Pingheng Tan, Jingqi Nie, and Fei Wei. Growing 20 cm long dwnts/twnts at a rapid growth rate of 80−90 um/s. *Chemistry of Materials*, 22(4):1294–1296, 2010.

[26] A. Jorio, G. Dresselhaus, and M. S. Dresselhaus. *Carbon nanotubes: Advanced topics in the synthesis, structure, properties, and applications*. Springer, Berlin and and New York, 2008.

[27] Stephanie Reich, Christian Thomsen, and Janina Maultzsch. *Carbon nanotubes: Basic concepts and physical properties*. Wiley-VCH, Weinheim, 2 edition, 2005.

[28] E. Ivchenko and B. Spivak. Chirality effects in carbon nanotubes. *Physical Review B*, 66(15), 2002.

[29] M. M. J. Treacy, T. W. Ebbesen, and J. M. Gibson. Exceptionally high young's modulus observed for individual carbon nanotubes. *Nature*, 381(6584):678–680, 1996.

[30] Min-Feng Yu, Bradley Files, Sivaram Arepalli, and Rodney Ruoff. Tensile loading of ropes of single wall carbon nanotubes and their mechanical properties. *Physical Review Letters*, 84(24):5552–5555, 2000.

[31] K. Zhang, M.M.F Yuen, J.H Gao, and B. Xu. Fabrication of high thermal conductivity carbon nanotube arrays by self assembled fe3o4 particles. *CIRP Annals - Manufacturing Technology*, 56(1):245–248, 2007.

[32] Madhu Sudan Saha, Ruying Li, Xueliang Sun, and Siyu Ye. 3-d composite electrodes for high performance pem fuel cells composed of pt supported on nitrogen-doped carbon nanotubes grown on carbon paper. *Electrochemistry Communications*, 11(2):438–441, 2009.

[33] X. Sun, R. Li, D. Villers, J.P Dodelet, and S. Désilets. Composite electrodes made of pt nanoparticles deposited on carbon nanotubes grown on fuel cell backings. *Chemical Physics Letters*, 379(1-2):99–104, 2003.

[34] B. Gao, A. Kleinhammes, X.P Tang, C. Bower, L. Fleming, Y. Wu, and O. Zhou. Electrochemical intercalation of single-walled carbon nanotubes with lithium. *Chemical Physics Letters*, 307(3-4):153–157, 1999.

[35] Vasilis G. Gavalas, Rodney Andrews, Dibakar Bhattacharyya, and Leonidas G. Bachas. Carbon nanotube sol−gel composite materials. *Nano Letters*, 1(12):719–721, 2001.

[36] Yoshikazu Nakayama and Seiji Akita. Field-emission device with carbon nanotubes for a flat panel display. *Synthetic Metals*, 117(1-3):207–210, 2001.

[37] O.K Varghese, P.D Kichambre, D. Gong, K.G Ong, E.C Dickey, and C.A Grimes. Gas sensing characteristics of multi-wall carbon nanotubes. *Sensors and Actuators B: Chemical*, 81(1):32–41, 2001.

[38] WeiFen Jiang, ShunHua Xiao, HuanYun Zhang, YongFen Dong, and Xin-Jian Li. Capacitive humidity sensing properties of carbon nanotubes grown on silicon nanoporous pillar array. *Science in China Series E: Technological Sciences*, 50(4):510–515, 2007.

[39] P. Wallace. The band theory of graphite. *Physical Review*, 71(9):622–634, 1947.

[40] Eduardo Fradkin. Critical behavior of disordered degenerate semiconductors. ii. spectrum and transport properties in mean-field theory. *Physical Review B*, 33(5):3263–3268, 1986.

[41] N. Mermin. Crystalline order in two dimensions. *Physical Review*, 176(1):250–254, 1968.

[42] David R. Nelson, Tsvi Piran, and S. Weingerg. *Statistical mechanics of membranes and surfaces*. World Scientific Pub, Singapore and and River Edge and N.J, 2 edition, 2004.

[43] Jannik C. Meyer, A. K. Geim, M. I. Katsnelson, K. S. Novoselov, T. J. Booth, and S. Roth. The structure of suspended graphene sheets. *Nature*, 446(7131):60–63, 2007.

[44] Scheila F. Braga, Vitor R. Coluci, Sergio B. Legoas, Ronaldo Giro, Douglas S. Galvão, and Ray H. Baughman. Structure and dynamics of carbon nanoscrolls. *Nano Letters*, 4(5):881–884, 2004.

[45] H. P. Boehm, A. Clauss, G. O. Fischer, and U. Hofmann. Das adsorptionsverhalten sehr dnner kohlenstoff-folien. *Zeitschrift fr anorganische und allgemeine Chemie*, 316(3-4):119–127, 1962.

[46] Andre K. Geim and Philip Kim. Carbon wonderland. *Scientific American*, 298(4):90–97, 2008.

[47] K. S. Novoselov. Electric field effect in atomically thin carbon films. *Science*, 306(5696):666–669, 2004.

[48] Dmitriy A. Dikin, Sasha Stankovich, Eric J. Zimney, Richard D. Piner, Geoffrey H. B. Dommett, Guennadi Evmenenko, SonBinh T. Nguyen, and Rodney S. Ruoff. Preparation and characterization of graphene oxide paper. *Nature*, 448(7152):457–460, 2007.

[49] Yenny Hernandez, Valeria Nicolosi, Mustafa Lotya, Fiona M. Blighe, Zhenyu Sun, Sukanta De, I. T. McGovern, Brendan Holland, Michele Byrne, Yurii K. Gun'Ko, John J. Boland, Peter Niraj, Georg Duesberg, Satheesh Krishnamurthy, Robbie Goodhue, John Hutchison, Vittorio Scardaci, Andrea C. Ferrari, and Jonathan N. Coleman. High-yield production of graphene by liquid-phase exfoliation of graphite. *Nature Nanotechnology*, 3(9):563–568, 2008.

[50] Mustafa Lotya, Yenny Hernandez, Paul J. King, Ronan J. Smith, Valeria Nicolosi, Lisa S. Karlsson, Fiona M. Blighe, Sukanta De, Zhiming Wang, I. T. McGovern, Georg S. Duesberg, and Jonathan N. Coleman. Liquid phase production of graphene by exfoliation of graphite in surfactant/water solutions. *Journal of the American Chemical Society*, 131(10):3611–3620, 2009.

[51] Alfonso Reina, Xiaoting Jia, John Ho, Daniel Nezich, Hyungbin Son, Vladimir Bulovic, Mildred S. Dresselhaus, and Jing Kong. Large area, few-layer graphene films on arbitrary substrates by chemical vapor deposition. *Nano Letters*, 9(1):30–35, 2009.

[52] Chong-an Di, Dacheng Wei, Gui Yu, Yunqi Liu, Yunlong Guo, and Daoben Zhu. Patterned graphene as source/drain electrodes for bottom-contact organic field-effect transistors. *Advanced Materials*, 20(17):3289–3293, 2008.

[53] C. Berger. Electronic confinement and coherence in patterned epitaxial graphene. *Science*, 312(5777):1191–1196, 2006.

[54] Han Huang, Wei Chen, Shi Chen, and Andrew Thye Shen Wee. Bottom-up growth of epitaxial graphene on 6h-sic(0001). *ACS Nano*, 2(12):2513–2518, 2008.

[55] Liying Jiao, Xinran Wang, Georgi Diankov, Hailiang Wang, and Hongjie Dai. Facile synthesis of high-quality graphene nanoribbons. *Nature Nanotechnology*, 5(5):321–325, 2010.

[56] A. K. Geim and K. S. Novoselov. The rise of graphene. *Nature Materials*, 6(3):183–191, 2007.

[57] Changgu Lee, Xiaoding Wei, Jeffrey W. Kysar, and James Hone. Measurement of the elastic properties and intrinsic strength of monolayer graphene. *Science*, 321(5887):385–388, 2008.

[58] A. Kuzmenko, E. van Heumen, F. Carbone, and D. van der Marel. Universal optical conductance of graphite. *Physical Review Letters*, 100(11), 2008.

[59] Alexander A. Balandin, Suchismita Ghosh, Wenzhong Bao, Irene Calizo, Desalegne Teweldebrhan, Feng Miao, and Chun Ning Lau. Superior thermal conductivity of single-layer graphene. *Nano Letters*, 8(3):902–907, 2008.

[60] Phaedon Avouris, Zhihong Chen, and Vasili Perebeinos. Carbon-based electronics. *Nat Nano*, 2(10):605–615, 2007.

[61] Andrey K. Geim and Allan H. MacDonald. Graphene: Exploring carbon flatland. *Physics Today*, 60(8):35–41, 2007.

[62] Andre K. Geim and Philip Kim. Carbon wonderland. *Scientific American*, 298(4):90–97, 2008.

[63] A. K. Geim. Graphene: Status and prospects. *Science*, 324(5934):1530–1534, 2009.

[64] Virendra Singh, Daeha Joung, Lei Zhai, Soumen Das, Saiful I. Khondaker, and Sudipta Seal. Graphene based materials: Past, present and future. *Progress In Materials Science*, 56(8):1178–1271, 2011.

[65] A. H. Castro Neto, F. Guinea, N. M. R. Peres, K. S. Novoselov, and A. K. Geim. The electronic properties of graphene. *Reviews of Modern Physics*, 81(1):109–162, 2009.

[66] R. N. Costa Filho, G. A. Farias, and F. M. Peeters. Graphene ribbons with a line of impurities: Opening of a gap. *Physical Review B*, 76(19):193409, 2007.

[67] M. Fujita, K. Wakabayashi, K. Nakada, and K. Kusakabe. Peculiar localized state at zigzag graphite edge. *Journal of the Physical Society of Japan*, 65(7):1920–1923, 1996.

[68] K. Wakabayashi, M. Fujita, H. Ajiki, and M. Sigrist. Electronic and magnetic properties of nanographite ribbons. *Physical Review B*, 59(12):8271–8282, 1999.

[69] K. Nakada, M. Fujita, G. Dresselhaus, and M. S. Dresselhaus. Edge state in graphene ribbons: Nanometer size effect and edge shape dependence. *Physical Review B*, 54(24):17954–17961, 1996.

[70] VerÃ³nica Barone, Oded Hod, and Gustavo E. Scuseria. Electronic structure and stability of semiconducting graphene nanoribbons. *Nano Lett*, 6(12):2748–2754, 2006.

[71] Melinda Y. Han, Barbaros Oezyilmaz, Yuanbo Zhang, and Philip Kim. Energy band-gap engineering of graphene nanoribbons. *Physical Review Letters*, 98(20):206805, 2007.

[72] Z. F. Wang, Q. W. Shi, Qunxiang Li, Xiaoping Wang, J. G. Hou, Huaixiu Zheng, Yao Yao, and Jie Chen. Z-shaped graphene nanoribbon quantum dot device. *Applied Physics Letters*, 91(5):053109, 2007.

[73] Yuanbo Zhang, Yan-Wen Tan, Horst L. Stormer, and Philip Kim. Experimental observation of the quantum hall effect and berry's phase in graphene. *Nature*, 438(7065):201–204, 2005.

[74] A. C. Ferrari, J. C. Meyer, V. Scardaci, C. Casiraghi, M. Lazzeri, F. Mauri, S. Piscanec, D. Jiang, K. S. Novoselov, S. Roth, and A. K. Geim. Raman spectrum of graphene and graphene layers. *Physical Review Letters*, 97(18), 2006.

[75] X. Jia, M. Hofmann, V. Meunier, B. G. Sumpter, J. Campos-Delgado, J. M. Romo-Herrera, H. Son, Y.-P Hsieh, A. Reina, J. Kong, M. Terrones, and M. S. Dresselhaus. Controlled formation of sharp zigzag and armchair edges in graphitic nanoribbons. *Science*, 323(5922):1701–1705, 2009.

[76] Mauricio Terrones. Materials science: Nanotubes unzipped. *Nature*, 458(7240):845–846, 2009.

[77] Mohammad Choucair, Pall Thordarson, and John A. Stride. Gram-scale production of graphene based on solvothermal synthesis and sonication. *Nature Nanotechnology*, 4(1):30–33, 2008.

[78] Vincent C. Tung, Matthew J. Allen, Yang Yang, and Richard B. Kaner. High-throughput solution processing of large-scale graphene. *Nature Nanotechnology*, 4(1):25–29, 2008.

[79] Sungjin Park and Rodney S. Ruoff. Chemical methods for the production of graphenes. *Nature Nanotechnology*, 4(4):217–224, 2009.

[80] G.D Yuan, W.J Zhang, Y. Yang, Y.B Tang, Y.Q Li, J.X Wang, X.M Meng, Z.B He, C.M.L Wu, I. Bello, C.S Lee, and S.T Lee. Graphene sheets via microwave chemical vapor deposition. *Chemical Physics Letters*, 467(4-6):361–364, 2009.

[81] Dan Li, Marc B. Müller, Scott Gilje, Richard B. Kaner, and Gordon G. Wallace. Processable aqueous dispersions of graphene nanosheets. *Nature Nanotechnology*, 3(2):101–105, 2008.

[82] X. Li, X. Wang, L. Zhang, S. Lee, and H. Dai. Chemically derived, ultrasmooth graphene nanoribbon semiconductors. *Science*, 319(5867):1229–1232, 2008.

[83] S. Y. Zhou, G.-H Gweon, A. V. Fedorov, P. N. First, W. A. de Heer, D.-H Lee, F. Guinea, A. H. Castro Neto, and A. Lanzara. Substrate-induced bandgap opening in epitaxial graphene. *Nature Materials*, 6(11):916, 2007.

[84] Jessica Campos-Delgado, Jose Manuel Romo-Herrera, Xiaoting Jia, David A. Cullen, Hiroyuki Muramatsu, Yoong Ahm Kim, Takuya Hayashi, Zhifeng Ren, David J. Smith, Yu Okuno, Tomonori Ohba, Hirofumi Kanoh,

Katsumi Kaneko, Morinobu Endo, Humberto Terrones, Mildred S. Dresselhaus, and Mauriclo Terrones. Bulk production of a new form of sp(2) carbon: Crystalline graphene nanoribbons. *Nano Letters*, 8(9):2773–2778, 2008.

[85] Dacheng Wei, Yunqi Liu, Yu Wang, Hongliang Zhang, Liping Huang, and Gui Yu. Synthesis of n-doped graphene by chemical vapor deposition and its electrical properties. *Nano Letters*, 9(5):1752–1758, 2009.

[86] Tobias N. Hoheisel, Stephen Schrettl, Ruth Szilluweit, and Holger Frauenrath. Nanostructured carbonaceous materials from molecular precursors. *Angewandte Chemie-international Edition*, 49(37):6496–6515, 2010.

[87] Elena Bekyarova, Mikhail E. Itkis, Palanisamy Ramesh, Claire Berger, Michael Sprinkle, Walt A. de Heer, and Robert C. Haddon. Chemical modification of epitaxial graphene: Spontaneous grafting of aryl groups. *Journal of the American Chemical Society*, 131(4):1336–+, 2009.

[88] Vitor M. Pereira, A. H. Castro Neto, and N. M. R. Peres. Tight-binding approach to uniaxial strain in graphene. *Physical Review B*, 80(4):045401, 2009.

[89] Gui Gui, Jin Li, and Jianxin Zhong. Band structure engineering of graphene by strain: First-principles calculations. *Physical Review B*, 78(7):075435, 2008.

[90] C. W. J. Beenakker. Colloquium: Andreev reflection and klein tunneling in graphene. *Reviews of Modern Physics*, 80(4):1337–1354, 2008.

[91] Z. M. Ao, J. Yang, S. Li, and Q. Jiang. Enhancement of co detection in al doped graphene. *Chemical Physics Letters*, 461(4-6):276–279, 2008.

[92] J. S. Bunch, Y. Yaish, M. Brink, K. Bolotin, and P. L. McEuen. Coulomb oscillations and hall effect in quasi-2d graphite quantum dots. *Nano Letters*, 5(2):287–290, 2005.

[93] Wenrong Yang, Kyle R. Ratinac, Simon P. Ringer, Pall Thordarson, J. Justin Gooding, and Filip Braet. Carbon nanomaterials in biosensors: Should you use nanotubes or graphene? *Angewandte Chemie-international Edition*, 49(12):2114–2138, 2010.

[94] Z. M. Ao, Q. Jiang, R. Q. Zhang, T. T. Tan, and S. Li. Al doped graphene: A promising material for hydrogen storage at room temperature. *Journal of Applied Physics*, 105(7):074307, 2009.

[95] Lian Sun, Qunxiang Li, Hao Ren, Haibin Su, Q. W. Shi, and Jinlong Yang. Strain effect on electronic structures of graphene nanoribbons: A first-principles study. *Journal of Chemical Physics*, 129(7):074704, 2008.

[96] Yang Wu, Mingyuan Huang, Feng Wang, X. M. Henry Huang, Sami Rosenblatt, Limin Huang, Hugen Yan, Stephen P. O'Brien, James Hone, and Tony F. Heinz. Determination of the young's modulus of structurally defined carbon nanotubes. *Nano Letters*, 8(12):4158–4161, 2008.

[97] Ricardo Faccio, Pablo A. Denis, Helena Pardo, Cecilia Goyenola, and Alvaro W. Mombru. Mechanical properties of graphene nanoribbons. *Journal of Physics-condensed Matter*, 21(28):285304, 2009.

[98] K. S. Novoselov, A. K. Geim, S. V. Morozov, D. Jiang, M. I. Katsnelson, I. V. Grigorieva, S. V. Dubonos, and A. A. Firsov. Two-dimensional gas of massless dirac fermions in graphene. *Nature*, 438(7065):197–200, 2005.

[99] C. N. R. Rao, A. K. Sood, K. S. Subrahmanyam, and A. Govindaraj. Graphene: The new two-dimensional nanomaterial. *Angewandte Chemie International Edition*, 48(42):7752–7777, 2009.

[100] A. Bunde. Liquids in a periodic medium: Commensurability effects. *Zeitschrift fr Physik B Condensed Matter*, 44(3):225–232, 1981.

[101] Matthew Fisher and Wilhelm Zwerger. Quantum brownian motion in a periodic potential. *Physical Review B*, 32(10):6190–6206, 1985.

[102] H. Risken and T. K. Caugheyz. The fokker-planck equation: Methods of solution and application, 2nd ed. *Journal of Applied Mechanics*, 58(3):860, 1991.

[103] Amal K. Das and P. Schwendimann. Fokker-planck equation for a periodic potential. *Physica A: Statistical Mechanics and its Applications*, 89(3):605–612, 1977.

[104] A. Lacasta, J. Sancho, A. Romero, I. Sokolov, and K. Lindenberg. From subdiffusion to superdiffusion of particles on solid surfaces. *Physical Review E*, 70(5), 2004.

[105] Tim J. Booth, Peter Blake, Rahul R. Nair, Da Jiang, Ernie W. Hill, Ursel Bangert, Andrew Bleloch, Mhairi Gass, Kostya S. Novoselov, M. I. Katsnelson, and A. K. Geim. Macroscopic graphene membranes and their extraordinary stiffness. *Nano Letters*, 8(8):2442–2446, 2008.

[106] J. Scott Bunch, Scott S. Verbridge, Jonathan S. Alden, Arend M. van der Zande, Jeevak M. Parpia, Harold G. Craighead, and Paul L. McEuen. Impermeable atomic membranes from graphene sheets. *Nano Letters*, 8(8):2458–2462, 2008.

[107] Jannik C. Meyer, C. O. Girit, M. F. Crommie, and A. Zettl. Imaging and dynamics of light atoms and molecules on graphene. *Nature*, 454(7202):319–322, 2008.

[108] Hendrik Ulbricht, Gunnar Moos, and Tobias Hertel. Interaction of c60 with carbon nanotubes and graphite. *Physical Review Letters*, 90(9), 2003.

[109] Ch Girard, Ph Lambin, A. Dereux, and A. Lucas. van der waals attraction between two c60 fullerene molecules and physical adsorption of c60 on graphite and other substrates. *Physical Review B*, 49(16):11425–11432, 1994.

[110] P. Gravil, M. Devel, Ph Lambin, X. Bouju, Ch Girard, and A. Lucas. Adsorption of c60 molecules. *Physical Review B*, 53(3):1622–1629, 1996.

[111] M. Neek-Amal, N. Abedpour, S. Rasuli, A. Naji, and M. Ejtehadi. Diffusive motion of c_{60} on a graphene sheet. *Physical Review E*, 82(5), 2010.

[112] M. Neek-Amal, Reza Asgari, and M. R. Rahimi Tabar. The formation of atomic nanoclusters on graphene sheets. *Nanotechnology*, 20(13):135602, 2009.

[113] Jean-Pierre Hansen and Ian R. McDonald. *Theory of simple liquids*. Elsevier / Academic Press, Amsterdam ;, Boston, 3rd edition, 2007, c2006.

[114] A. Fasolino, J. H. Los, and M. I. Katsnelson. Intrinsic ripples in graphene. *Nature Materials*, 6(11):858–861, 2007.

[115] Otakar Frank, Georgia Tsoukleri, John Parthenios, Konstantinos Papagelis, Ibtsam Riaz, Rashid Jalil, Kostya S. Novoselov, and Costas Galiotis. Compression behavior of single-layer graphenes. *ACS Nano*, 4(6):3131–3138, 2010.

[116] Wenzhong Bao, Feng Miao, Zhen Chen, Hang Zhang, Wanyoung Jang, Chris Dames, and Chun Ning Lau. Controlled ripple texturing of suspended graphene and ultrathin graphite membranes. *Nature Nanotechnology*, 4(9):562–566, 2009.

[117] F. Guinea, M. I. Katsnelson, and A. K. Geim. Energy gaps and a zero-field quantum hall effect in graphene by strain engineering. *Nature Physics*, 6(1):30–33, 2009.

[118] Georgia Tsoukleri, John Parthenios, Konstantinos Papagelis, Rashid Jalil, Andrea C. Ferrari, Andre K. Geim, Kostya S. Novoselov, and Costas Galiotis. Subjecting a graphene monolayer to tension and compression. *Small*, 5(21):2397–2402, 2009.

[119] K. Zakharchenko, M. Katsnelson, and A. Fasolino. Finite temperature lattice properties of graphene beyond the quasiharmonic approximation. *Physical Review Letters*, 102(4), 2009.

[120] M. Neek-Amal and F. Peeters. Graphene nanoribbons subjected to axial stress. *Physical Review B*, 82(8), 2010.

[121] Donald Brenner. Empirical potential for hydrocarbons for use in simulating the chemical vapor deposition of diamond films. *Physical Review B*, 42(15):9458–9471, 1990.

[122] Donald W. Brenner, Olga A. Shenderova, Judith A. Harrison, Steven J. Stuart, Boris Ni, and Susan B. Sinnott. A second-generation reactive empirical bond order (rebo) potential energy expression for hydrocarbons. *Journal of Physics: Condensed Matter*, 14(4):783–802, 2002.

[123] Jan Los, Luca Ghiringhelli, Evert Meijer, and A. Fasolino. Improved long-range reactive bond-order potential for carbon. i. construction. *Physical Review B*, 72(21), 2005.

[124] Qiang Lu, Marino Arroyo, and Rui Huang. Elastic bending modulus of monolayer graphene. *Journal of Physics D: Applied Physics*, 42(10):102002, 2009.

[125] Konstantin Kudin, Gustavo Scuseria, and Boris Yakobson. C2f, bn, and c nanoshell elasticity from ab initio computations. *Physical Review B*, 64(23), 2001.

[126] P. Liu and Y. W. Zhang. Temperature-dependent bending rigidity of graphene. *Applied Physics Letters*, 94(23):231912, 2009.

[127] Konstantin V. Zakharchenko. *Temperature effects on graphene: From flat crystal to 3D liquid*. PhD thesis, Radboud University Nijmegen.

[128] Emiliano Cadelano, Pier Palla, Stefano Giordano, and Luciano Colombo. Nonlinear elasticity of monolayer graphene. *Physical Review Letters*, 102(23), 2009.

[129] Aleksey Kolmogorov and Vincent Crespi. Registry-dependent interlayer potential for graphitic systems. *Physical Review B*, 71(23), 2005.

[130] K. H. Michel and B. Verberck. Theory of the elastic constants of graphite and graphene. *physica status solidi (b)*, 245(10):2177–2180, 2008.

[131] O. Leenaerts, H. Peelaers, A. Hernández-Nieves, B. Partoens, and F. Peeters. First-principles investigation of graphene fluoride and graphane. *Physical Review B*, 82(19), 2010.

[132] Enrique Muñoz, Abhishek K. Singh, Morgana A. Ribas, Evgeni S. Penev, and Boris I. Yakobson. The ultimate diamond slab: Graphane versus graphene. *Diamond and Related Materials*, 19(5-6):368–373, 2010.

[133] Fang Liu, Pingbing Ming, and Ju Li. Ab initio calculation of ideal strength and phonon instability of graphene under tension. *Physical Review B*, 76(6), 2007.

[134] X. Chang, Y. Ge, and J. M. Dong. Ripples of aa and ab stacking bilayer graphenes. *The European Physical Journal B*, 78(1):103–109, 2010.

[135] Robert M. Jones. *Buckling of bars, plates, and shells*. Bull Ridge Publishing, Blacksburg, Va, 2006.

[136] M. Neek-Amal and F. Peeters. Lattice thermal properties of graphane: Thermal contraction, roughness, and heat capacity. *Physical Review B*, 83(23), 2011.

[137] T. Mohiuddin, A. Lombardo, R. Nair, A. Bonetti, G. Savini, R. Jalil, N. Bonini, D. Basko, C. Galiotis, N. Marzari, K. Novoselov, A. Geim, and A. Ferrari. Uniaxial strain in graphene by raman spectroscopy: G peak splitting, grüneisen parameters, and sample orientation. *Physical Review B*, 79(20), 2009.